ผลของความเครียดในการปลูกฟิล์มบางแบบเฮเทอโรเอพิแทกเซียล: แบบจำลองบอล-สปริง

นายมาณิต แกล้วทนงค์

วิทยานิพนธ์นี้เป็นส่วนหนึ่งของการศึกษาตามหลักสูตรปริญญาวิทยาศาสตรดุษฎีบัณฑิต
สาขาวิชาฟิสิกส์ ภาควิชาฟิสิกส์
คณะวิทยาศาสตร์ จุฬาลงกรณ์มหาวิทยาลัย
ปีการศึกษา 2556
ลิขสิทธิ์ของจุฬาลงกรณ์มหาวิทยาลัย

EFFECTS OF STRAIN IN HETEROEPITAXIAL THIN FILM GROWTH: A
BALL-SPRING MODEL

Mr. Manit Klawtanong

A Dissertation Submitted in Partial Fulfillment of the Requirements
for the Degree of Doctor of Philosophy Program in Physics
Department of Physics
Faculty of Science
Chulalongkorn University
Academic Year 2013

Thesis Title	EFFECTS OF STRAIN IN HETEROEPITAXIAL THIN FILM GROWTH: A BALL-SPRING MODEL
By	Mr. Manit Klawtanong
Field of Study	Physics
Thesis Advisor	Chatchai Srinitiwarawong, Ph.D.
Thesis Co-Advisor	Assistant Professor Patcha Chatraphorn, Ph.D.

Accepted by the Faculty of Science, Chulalongkorn University in Partial Fulfillment of the Requirements for the Doctoral Degree

.... Dean of the Faculty of Science

(Professor Supot Hannongbua, Dr.rer.nat.)

THESIS COMMITTEE

.... Chairman

(Assistant Professor Nuttakorn Thubthong, Ph.D.)

.... Thesis Advisor

(Chatchai Srinitiwarawong, Ph.D.)

.... Thesis Co-Advisor

(Assistant Professor Patcha Chatraphorn, Ph.D.)

.... Examiner

(Assistant Professor Sakuntam Sanorpim, Ph.D.)

.... Examiner

(Orapin Wannadelok, Ph.D.)

.... External Examiner

(Soontorn Chanyawadee, Ph.D.)

มาณิต แกล้วทนงค์ : ผลของความเครียดในการปลูกฟิล์มบางแบบเฮเทอโรเอพิแทก เซียล: แบบจำลองบอล-สปริง. (EFFECTS OF STRAIN IN HETEROEPITAXIAL THIN FILM GROWTH: A BALL-SPRING MODEL) อ.ที่ปรึกษาวิทยานิพนธ์หลัก : ดร.ฉัตรชัย ศรีนิติวรวงศ์, อ.ที่ปรึกษาวิทยานิพนธ์ร่วม : ผศ.ดร.ปัจฉา ฉัตราภรณ์, 108 หน้า.

การสร้างชั้นเฮเทอโรเอพิแทกซีเป็นอีกหนึ่งหัวข้อสำคัญในการศึกษาฟิสิกส์ฟิล์มบาง โดยคาดหวังว่าเกาะเครียดประกอบเองที่เกิดขึ้นระหว่างกระบวนการเติบโตของฟิล์มจะมี สมบัติที่น่าสนใจและสามารถนำไปใช้ในอุปกรณ์เชิงแสงและอิเล็กทรอนิกส์ ดังนั้นการควบคุม สมบัติของเกาะเช่นเดียวกับปรับปรุงเอกรูปและลำดับจึงมีความสำคัญมาก ในวิทยานิพนธ์ นี้เราศึกษาระบบเฮเทอโรเอพิแทกซีผ่านแบบจำลองคอมพิวเตอร์ แบบจำลองบอล-สปริง ไม่ต่อเนื่องกันสองมิติถูกใช้ในการจำลองมอนติคาร์โลจลน์ ผลลัพธ์ของเราแสดงให้เห็นว่า ความเครียดที่ผิวร่วมฟิล์ม-ซับสเตรตไบแอสกระบวนการแพร่อะตอมผิวฟิล์มซึ่งส่งเสริมการ ก่อเกิดเกาะและหลุม การก่อเกิดหลุมในกรอบการเติบโตจำกัดเชิงจลน์เป็นอีกหนึ่งกลไก เพื่อผ่อนคลายความเครียดในระบบ ความหนาวิกฤต ขนาดเกาะและจำนวนเกาะถูกพบ ว่าขึ้นอยู่กับเงื่อนไขการเติบโต นอกจากนี้เรายังใช้ระเบียบวิธีเลขชี้กำลังความขรุขระซึ่งใช้ ทั่วไปในการศึกษาการเติบโตของผิวฟิล์มเพื่อมาประยุกต์ใช้ในแบบจำลองฟรัสเทรตแอนติ เฟร์โรแมกเนติกเอกซ์วายสปิน โดยการแปลงโครงแบบสปินไปยังผิวฟิล์มของแบบจำลอง การเติบโตเอสโอเอสที่ดัดแปรเราแสดงให้เห็นว่าความขรุขระและเลขชี้กำลังความขรุขระ ประสบความสำเร็จในการหาค่าอุณหภูมิวิกฤติและเลขชี้กำลังวิกฤติสำหรับการเปลี่ยนสถานะ ที่สูญเสียสมมาตรไครแรลในแบบจำลองสปิน

ภาควิชา ฟิสิกส์	ลายมือชื่อนิสิต	
สาขาวิชา ฟิสิกส์	ลายมือชื่อ อ.ที่ปรึกษาวิทยานิพนธ์หลัก	
ปีการศึกษา 2556	ลายมือชื่อ อ.ที่ปรึกษาวิทยานิพนธ์ร่วม	

5273840423 : MAJOR PHYSICS

KEYWORDS : HETEROEPITAXY / STRAINED ISLANDS / MONTE CARLO / FAXY MODEL

MANIT KLAWTANONG : EFFECTS OF STRAIN IN HETEROEPITAXIAL THIN FILM GROWTH: A BALL-SPRING MODEL. ADVISOR : CHATCHAI SRINITIWARAWONG, Ph.D., CO-ADVISOR : ASST. PROF. PATCHA CHATRAPHORN, Ph.D., 108 pp.

Heteroepitaxial growth is one of the promising topics studied in thin film physics. The self-assembled strain islands formed during the growth process are expected to have interesting properties that can be used in optoelectronic devices. Controlling island properties as well as improving island uniformity and ordering are therefore crucial. In this dissertation, we investigate a heteroepitaxial system via computer modeling. A two-dimensional discrete ball and spring model is used in the kinetic Monte Carlo simulations. Our results show that strain at the film-substrate interface creates a bias in the adatom diffusion process which promotes island and pit formations. The pit formation in a limited mobility growth regime is another mechanism to relieve strain in the system. The critical thickness, island size, and number of islands are found to depend on the values of growth conditions. Furthermore, we apply a roughness exponent method normally used in surface growth study to the frustrated antiferromagnetic XY spin model. By mapping spin configurations to film surfaces of a modified SOS growth model, we show that the film roughness and its exponents successfully determine the critical temperature and critical exponents for the chiral symmetry breaking transition in the spin model.

Department : Physics .... Student's Signature ....

Field of Study : Physics .... Advisor's Signature ....

Academic Year : 2013 .... Co-Advisor's Signature ....

Acknowledgements

I would like to express my sincere gratitude to my thesis advisor, Dr. Chatchai Srinitiwarawong, and my thesis co-advisor, Asst. Prof. Dr. Patcha Chatraphorn, from whom I have learned a lot and without whose guidance and suggestions the work presented here would not have been possible. I greatly appreciate that they are always willing to give me advice throughout my study.

I would like to thank the dissertation committee, Asst. Prof. Dr. Nuttakorn Thubthong, Asst. Prof. Dr. Sakuntam Sanorpim, Dr. Orapin Wannadelok, and Dr. Soontorn Chanyawadee, for valuable comments and suggestions.

I would like to thank Asst. Prof. Dr. Kajornyod Yoodee, Asst. Prof. Dr. Surachate Limkumnerd, for helpful discussions and suggestions during this work, and especially Asst. Prof. Dr. Sojiphong Chatraphorn, for providing and maintaining high-efficiency computer facilities.

I would like to acknowledge Thailand Center of Excellence in Physics (ThEP Center) for financial support. This work was partially supported by Research Funds from the Faculty of Science, Chulalongkorn University and also the Special Task Force for Activating Research (STAR), Ratchadaphiseksomphot Endowment Fund, Chulalongkorn University through the Energy Materials Physics Research Group.

A lot of thanks go to all my friends and people at the Department of Physics, particularly my friends in the Semiconductor Physics Research Laboratory (SPRL), Aj. R. Chanphana, S. Piankoranee, J. Disrattakit, P. Disrattakit, C. Chaiyasorn, W. Kanjanaput, C. Chomngam, J. Yaemwong, S. Potepanit, and the SPRL's members whose names are not mentioned here, who have shared warm friendships and helped me by any means.

Last but not least, I would like to thank my parents, my brother, and my sister, who always support and understand me during my difficult times. I cannot give enough thanks for everything they have done for me.

Contents

List of Tables

List of Figures

Figure   **page**

Figure **page**

CHAPTER I

Introduction

1.1 Epitaxial growth

Epitaxial growth is an important process to fabricate high quality thin films. This process occurs during the deposition of new material to form a crystalline overlayer on a crystalline substrate. The overlayer, which is called an epitaxial film or epitaxial layer, prefers specific orientations with respect to the crystalline substrate. The history of epitaxial growth dates back in the 1920s after Louis Royer carried out an extensive study and discovered a new systematic way of growing epitaxial films [1]. The word "epitaxy", which means "upon order", was termed to distinguish epitaxial growth from polycrystalline and amorphous growth [1]. The most powerful application of epitaxy is the semiconductor devices—for example transistors, lasers, and solar cells—which are found in everyday life.

Well-known techniques for epitaxial growth are molecular-beam epitaxy (MBE) and metal-organic vapor-phase epitaxy (MOVPE). For the MBE technique, epitaxial growth consists of three processes [2]. In the first process, the deposition process, atoms or simple molecules are evaporated from heated sources known as *the Knudsen effusion cells*. The "beam" of particles is then collimated and directed toward the heated substrate. The mean free path of the particles is very long so that the particles do not interact with each other until they reach the substrate. The second process is the diffusion of mobile atoms (adatoms) on the film surface. The last process is the desorption process, which is a rare process and not desired in most epitaxial growth. To achieve an epitaxial film with a

preferred crystalline structure, the growth must be carried out in an extreme environment: ultra-high vacuum (pressure $\approx 10^{-10}$ torr), high purity, and low growth rate (≈ 1 monolayer/s) [3]. The low growth rate leads to what is commonly known as the layer-by-layer growth mode[1]. Growth conditions, e.g. the deposition flux and substrate temperature, can be varied during the growth process.

Characterization tools such as the reflection high-energy electron diffraction (RHEED), scanning tunneling microscopy (STM), and atomic force microscopy (AFM) have been used to study the grown films. The RHEED is suitable for monitoring the real-time growth because it can observe *in situ* under normal growth conditions without interference the growth process, providing precisely identification of surface morphologies and crystalline structures.

Epitaxy can be categorized into two types according to growth materials. For homoepitaxial growth, the film and substrate are of the same material. In contrast, for heteroepitaxial growth, the film and substrate are of the different materials. In the latter case, lattice spacings of film and substrate atoms at the film-substrate interface do not match, and it is called *the lattice mismatch* or *misfit* (ϵ):

$$\epsilon = (a_f - a_s)/a_f, \tag{1.1}$$

where a_f and a_s are lattice constants of the film and substrate, respectively.

Heteroepitaxy has attracted much interest from researchers because of a rich variety of surface morphologies and its potential applications [1, 4, 5]. The well-known examples are the growth of Ge/Si with $\sim 4.0\%$ lattice mismatch [6, 7, 8, 9, 10, 11, 12, 13, 14, 15, 16, 17, 18, 19] and the growth of InAs/GaAs with $\sim$ 7.0% lattice mismatch [18, 20, 21, 22, 23, 24, 25]. Because of the incompatibility at the film-substrate interface, the film experiences strain which normally introduces defects, e.g. dislocations and stacking faults, to the film layer. As a result, the quality of the film is reduced. However, a novel surface morphology cannot be achieved without a contribution of strain. A good example is the fabrication of self-assembled, strained islands, which are approximately in order of 10-100

---

[1]Growth modes depend on interface free energies and will be discussed in the next section.

nanometers in size [6, 11, 12, 16, 21, 26] and commonly known as the quantum dots (QDs).

Fig. 1.1(a) shows a three-dimensional (3D) AFM image of Ge/Si QDs grown by the MBE technique [17]. Quantum dots have intriguing electronic and optical properties. According to dimensionality, carriers in QDs are spatially confined in all directions, and energy levels are quantized [4]. The density of state (DOS) of a single dot (sometime called an artificial atom) is described by Dirac delta function [21]. For an array of QDs, however, the DOS exhibits a broad peak depending on the distribution of the quantum dots. The energy spectra of QDs can be measured by using the photoluminescence (PL) [21].

Nowadays, many studies have been focused on how to fabricate uniformly distributed QDs in a large scale [6, 27, 28, 29]. This feature is important for many applications such as tunable wavelength lasers and other optoelectronic devices. In the recent development of laser technology, devices consisting of QDs exhibit superior properties: excellent temperature stability, low threshold current density, and large radiation resistance [4]. Fig. 1.1(b) shows one of the commercial applications of quantum dots used in light emitting devices [30]. Extensive reviews of QDs and their applications can be found in Refs. [5, 6, 31, 32, 33, 34, 35].
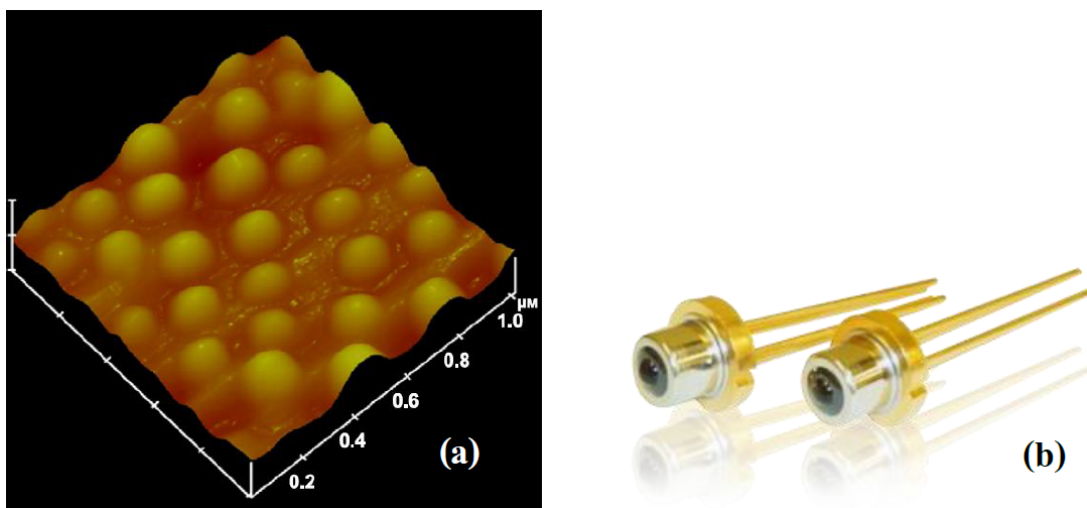
Figure 1.1: (a) A three-dimensional AFM image of Ge/Si quantum dots [17] and (b) an application of quantum dots used in light emitting devices [30].

1.2 Growth modes

Epitaxial growth can be categorized to one of the three growth modes depending on interface free energies: vacuum-film free energy (γ_{vf}), film-substrate free energy (γ_{fs}), and vacuum-substrate free energy (γ_{vs}) [1, 36]. Fig. 1.2(a) shows the Frank-van der Merwe (FM) or layer-by-layer growth mode. The vacuum-substrate free energy is higher than the combination of the film-substrate free energy and the vacuum-film free energy, $\gamma_{vs} > \gamma_{fs} + \gamma_{vf}$, so the film will "wet" the substrate. In this growth, adatoms tend to complete a film layer underneath before a new layer is created. The film is flat and consists of a single crystalline structure. Indeed, layer-by-layer growth is the ideal growth which is hardly seen, in a long-time scale of growth, in experiments. In early stages of the growth, however, it is observed in several heteroepitaxial systems with small lattice mismatches ($\epsilon < 2\%$). The film is considered to be in an unstable state against stress suppression. Up to a certain thickness, misfit dislocations, stacking faults, surface deformations etc. are introduced to the film to relieve strain, and the growth is no longer the layer-by-layer growth.

In contrast, the Volmer-Weber (VW) growth mode [see Fig. 1.2(b)] prefers the vacuum-substrate interface. The combination of the film-substrate free energy and the vacuum-film free energy is too large, $\gamma_{fs} + \gamma_{vf} > \gamma_{vs}$, for the film to wet the substrate. In this growth, adatoms form 3D islands directly on top of the substrate without a prior completed layer. Islands are stable because the film avoids touching the substrate. This type of growth is normally found in early stages of heteroepitaxial growth with large lattice mismatches. The phenomenon is similar to a liquid drop on a flat substrate. In the thermodynamic equilibrium, it is characterized by *a contact angle* which depends on their surface tensions (or interface energies) [36].

Due to the fact that the film-substrate interface is stable if its energy is low enough, and the film-substrate free energy generally depends on the film thickness (h) for lattice-mismatched systems; $\gamma_{fs} = \gamma_{fs}(h)$, the Stranski-Krastanov (SK)
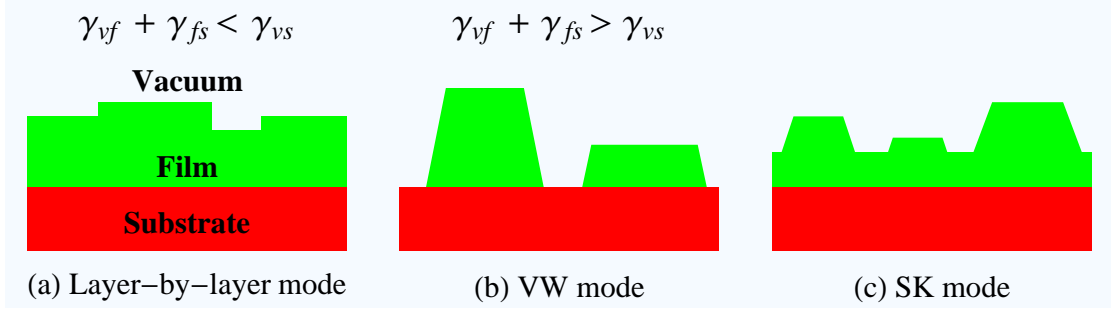
Figure 1.2: Schematic representation of three growth modes: (a) Layer-by-layer mode, (b) VW mode, and (c) SK mode.

growth mode [see Fig. 1.2(c)] can be described as follows. In early stages of growth ($h < h_c$ where h_c is a critical thickness), the growth is layer-by-layer, i.e. $\gamma_{vf} + \gamma_{fs}(h) < \gamma_{vs}$. Adatoms form a 2D flat layer called *a wetting layer*. The film-substrate free energy increases with the film thickness, and the layer-by-layer growth becomes energetically unfavorable. At a critical thickness ($h = h_c$), the relation does not hold, and it is no longer benefit to complete the wetting layer. In later stages ($h > h_c$); $\gamma_{vf} + \gamma_{fs}(h) > \gamma_{vs}$, 3D islands begin to nucleate on top of the wetting layer. If the film thickness is increased further, the vacuum-substrate free energy (γ_{vs}) dominates the interface free energies, and the 3D islands become stable. This type of growth is found in a moderate lattice mismatch regime, although exact values of the lattice mismatch vary from substance to substance.

Strain is considered to be a major factor responsible for the increasing of the film-substrate free energy $\gamma_{fs}(h)$. Generally, the elastic energy resulting from an accumulation of strain at the film-substrate interface increases with the film thickness and then changes the balance of the interface free energies. If the elastic energy is high enough, the film surface is deformed. At a critical thickness, adatoms begin to nucleate on top of the 2D wetting layer to form 3D islands, leading to a 2D-3D transition. The formation of 3D islands is one of the strain-relieved mechanisms found at a relatively small thickness before misfit dislocations are normally introduced at a larger thickness. The formation of 3D islands without dislocations known as *the dislocation-free* or *coherent* QDs, however, is more

attractive because of desirable properties of the films for many applications mentioned previously. The underlying mechanism of the 2D-3D transition and the role of the wetting layer are under discussion, and the study in this area is still widely open.

1.3 Previous work

In the theory of island formation known as the Asaro-Tiller-Grinfeld (ATG) instability (elastically driven instability) [36, 37], a flat, strained surface is unstable with respect to the suppression of an external force produced by the substrate. The mass transport driven by the instability along the film surface creates sinusoidal modulation [36]. The unstable surface remains flat unless a perturbation wavelength (λ) is sufficiently longer than a critical wavelength (λ_c), $\lambda > \lambda_c$. In this case, the modulation gradually develops into steeper islands, and the film-substrate free energy $\gamma_{fs}(h)$ is consequently reduced. The formation of 3D islands through the ATG instability provides a strain-relieved mechanism which does not require misfit dislocations to occur. The critical wavelength depends on the elastic property of the growth materials and the lattice mismatch (ϵ) as

$$\lambda_c \propto \epsilon^{-2}. \tag{1.2}$$

It is also proportional to island size l, providing direct control of the island size (QDs size) through the lattice mismatch

$$\lambda_c \propto l \propto \epsilon^{-2}. \tag{1.3}$$

Because effects of the arriving flux are not considered, the ATG instability theory is suitable for annealing films at high temperatures, where the mass transport is supported by adatom diffusion. For a growing film, the theory is still valid; however, the adatom diffusion process is interrupted by deposited atoms, and the power law relation in Eq. (1.3) is modified accordingly [12]. For the $Si_{1-x}Ge_x$/Si system, where x is the Ge concentration[2], it was found that [12, 13] 3D islands

---

[2]For the $Si_{1-x}Ge_x$/Si system, $\epsilon = 0.04x$.

gradually develop from ripple-like patterns at high temperature ($T \approx 950$ K) and small lattice mismatches ($0.56\% \leq \epsilon \leq 2.4\%$). Islands are steeper and bound by the (105) facets. The result is more consistent with the ATG instability, but the dependence of critical wavelength on the lattice mismatch is weaker; $\lambda_c \propto \epsilon^{-1}$. This is due to effects of the deposition flux, which stabilizes the film surface and makes the critical wavelength λ_c longer [12]. For large mismatches ($\epsilon > 2.4\%$) [13], the formation of conventional 3D islands was observed directly on the substrate, suggesting another strain-relieved mechanism: the island nucleation [8]. Whereas the ATG instability seems to be sensible for high temperature and small lattice mismatch growth, it is less sensible for low temperature and large lattice mismatch growth.

It is shown that [8] once an island (or pit) reaches a critical size, its associated energy is reduced. To form such a stable island, it must firstly overcome an energy barrier. The formation of 3D islands involving an energy barrier is known as the island nucleation [8]. The lattice mismatch (ϵ) lowers the energy barrier E_s, $E_s \propto \epsilon^{-4}$, and increases the island nucleation at a rate $R_{\text{nucl}} \propto \exp(-E_s/k_B T)$, where k_B is the Boltzmann constant. Islands can then easily nucleate on top of the substrate before the film surface has time to develop into a ripple-like pattern. In the growth of pure Ge on Si(001) substrate ($\epsilon \approx 4.0\%$) at low temperature ($T = 575$ K) [11], the formation of (105) faceted Ge islands (so-called hut clusters) can be understood in a context of the island nucleation.

From the above explanations, it is clear that growth conditions obviously play a crucial role whether the island formation is proceeded with the nucleation or instability [19]. In kinetic Monte Carlo (kMC) simulations, such nucleation [38, 39, 40] and instability [38] can be observed if the growth parameters are set properly.

As described earlier, heteroepitaxial growth has been extensively studied not only in experiments and theories but also in computer simulations. The density functional theory (DFT) is one of the most accurate approaches to be used in computer simulations. It provides useful microscopic details including equilibrium shapes and stability [41, 42], binding energies [43], and the 2D-3D transition [44].

However, using the DFT method is mostly impossible when the system size (or time scale) is very large. By coarse-graining lattice sites, continuum models can bypass the problem. The study of the morphological evolution [45, 46, 47, 48, 49, 50, 51] and island ordering [52, 53] is then possible. Nevertheless, microscopic processes and the island formation, which are sometimes more interesting than the morphological evolution itself, cannot be observed in the continuum models. In kMC simulations, discrete, solid-on-solid (SOS) growth models are widely used to study epitaxial growth [2]. A ball and spring model is particularly successful in describing the heteroepitaxial growth [54, 55, 56, 57, 58, 59]. The model was used earlier by Orr *et al.* [60], later by Barabási [61, 62], and Khor and Das Sarma [63, 64] to investigate the island formation. Various aspects of heteroepitaxial systems were studied, for example faceted islands [65], the wetting layer [66], and film intermixing or film alloying [59, 67, 68, 69]. An off-lattice model with the Lennard-Jones (LJ) potential was also implemented [70, 71] to study dislocations and the critical thickness (h_c) [72, 73, 74]. The studies were extended to 3D growth with small coverages and small substrate sizes [39, 40, 55, 66, 67, 68, 75, 76, 77, 78, 79, 80, 81].

One outstanding issue when discrete models are implemented is the long range nature of elasticity [36]. The (weak) long range interaction is a "global" characteristic which effects the results if the system size is too small. Since both accuracy and efficiency must be taken into account in order to capture relevant behavior of the strain, some approximation techniques have been used. Examples of these techniques are the Green's function approach with coarse-grained atom displacements [57], an energy cut-off [73], an expanding box method and upper bound rates [58], and the Fourier-multigrid method [82]. The larger the system size, the more sophisticated approximation method the models need.

According to previous experimental results [12, 13, 19], it is clear that the critical thickness h_c and island size l decrease with the lattice mismatch ϵ. However, the quantities are affected by the deposition flux as well [12]. The effects of growth conditions are not completely understood, e.g. the power law relation in

Eq. (1.3) is observed differently [12, 13, 19, 37, 38, 73]. Although the island size l and its uniformity in 3D submonolayer growth were studied [78], the substrate size is still small, and the film thickness h is less than 1 monolayer (ML). Effects of the deposition flux on the critical thickness h_c and island density were also investigated with a 2D off-lattice model [73]. Nevertheless, a complete study of island size l, island density, and critical thickness h_c dependence on the growth temperature is not available. The temperature and deposition flux are important factors because the parameters indicate whether the growth is mobility limited [19].

1.4   Objectives of this work

The scope of this work covers the following objectives. We investigate the island nucleation of the heteroepitaxial system on flat substrates. The effects of lattice mismatch, deposition flux and growth temperature on surface morphology and properties of the system such as the critical thickness, island size and number of islands are studied in detail. Statistical quantities are calculated and used to quantify the heteroepitaxial system.

In addition, we also use a roughness exponent method of a solid-on-solid growth model to determine critical temperature and critical exponents of the frustrated antiferromagnetic XY spin model.

1.5   The dissertation outline

In this chapter, we give an introduction of epitaxial growth. Growth techniques as well as characterization tools are also mentioned. The types of epitaxial growth are explained in a context of interface free energies. We then discuss previous work which focuses mainly on the heteroepitaxial systems. Detailed studies in theories, experiments, and computer simulations are provided. We also point out some effects of growth conditions on heteroepitaxial films which are not completely

understood, such as the growth temperature. Finally, we draw our objectives of this work.

In chapter II, Theory and Model, we provide most aspects of the theoretical background and computer modeling of the heteroepitaxial systems needed for performing simulations. A two-dimensional ball and spring model representing the heteroepitaxial system is described in detail. From equilibrium consideration, we outline the calculation of atom displacements and the elastic energy of the system.

In chapter III, Computer Simulations, we provide detailed simulations used in this work. Firstly, we describe microscopic processes of interest. We then provide an algorithm to solve a system of linear equations. Next, we discuss an energy localization and local approximation of the elastic energy used here. Finally, we present the kinetic Monte Carlo simulation method and the n-fold way algorithm.

In chapter IV, Results and Discussions, we present our numerical results of films grown on flat substrates at different lattice mismatches, deposition fluxes, and temperatures. The dependence of island size, number of islands, and critical thickness on the growth conditions are discussed in detail. We also compare our results with theoretical, experimental, and computational results presented in the literature.

In chapter V, An Application of Roughness Exponent Method in a Frustrated Spin System, we apply a roughness exponent method used in a solid-on-solid growth model to a spin model, the frustrated antiferromagnetic XY (FAXY) model, and show that the critical temperature and critical exponent of the spin model can be determined from the roughness exponent method. Firstly, we provide a literature review which focuses on the method for determining critical properties of seemingly different models including the spin models. We then introduce the FAXY model on a two-dimensional triangular lattice and the method used to determine critical properties of the FAXY model. Next, we present our numerical results obtained from the roughness exponent method and compare the

results with those obtained from conventional spin methods.

In chapter VI, Conclusions, we draw the conclusions of our work. The suggestions and future work are also mentioned.

CHAPTER II

Theory and Model

Historically, theoretical findings in physics were tested solely by experiments. After the computer invention, scientists can put a theoretical model to a computer, find a link between theories and experiments, and discover new models that describe many aspects of nature [2, 83]. The Eden model—which describes bacterial colonies—and the Ising model—which describes magnetic materials—are just a few examples. Models of interest are not only those motivated by nature. Models which are purely mathematical objects such as a cellular automaton and a fractal are studied for fundamental interest. Surprisingly and unexpectedly, a model intended for a particular system can also describe a phenomenon found in a seemingly different system [84].

Thin film physics becomes a popular subject after the MBE technique was introduced to grow high quality thin films [1, 36]. The study of kinetic roughening film surfaces is important because of their potential applications in industries and novel behavior found in a variety of thin film growth systems. To gain insight into the "real" MBE growth with many complex processes, simple models with a "minimal" set of rules are introduced. The models fill the gap between theory believed to govern the system and experimental results. Early models were used to describe the MBE growth which is generally far-from-equilibrium, relatively low temperature, layer-by-layer growth. The random deposition (RD) [2], Das Sarma-Tamborenea (DT) [84, 85], and Wolf-Villain (WV) [84, 86] models are examples of the so-called nonequilibrium, limited mobility, SOS growth models. These models are bound to specific rules of microscopic processes which are necessary for pro-

ducing films of interest. Non-MBE growth models such as the ballistic deposition (BD) [2] and the Family [84, 87] models are those of fundamental interest, which usually come together with the MBE growth models.

2.1 A two-dimensional ball and spring model

The formation of QDs in heteroepitaxial systems is an interesting phenomenon and is currently studied for various aspects. In the systems, the difference in the lattice constants of the film and substrate produces forces which act on film atoms and compress the atoms (for compressive strain) to take the natural lattice spacing of the substrate. The lattice spacing of the film atoms is gradually changed from the film-substrate interface to the topmost layer; therefore the film is said to be a commensurate structure [36].

In this study, we use a model which treats the heteroepitaxial system as a classical object: a discrete ball and spring model [38, 58, 60]. The model [see Fig. 2.1(a)] consists of film and substrate atoms with the same elastic property. Here, we restrict ourselves to 2D, SOS growth. The substrate has a simple cubic (SC) structure with four nearest neighbors (NN) and four next-nearest neighbors (NNN). The NN and NNN are connected by springs with spring constants k_{NN} and k_{NNN}, respectively. The interaction beyond NNN is considered very weak and is thus ignored. Note that bondings between film-film, substrate-substrate, and film-substrate atoms are the same. The natural lattice constant of the film is a_f, and the natural lattice constant of the substrate is a_s. In an equilibrium [see Fig. 2.1(b)], the lattice constant of the film is forced to take on the value of the lattice constant of the substrate in the horizontal direction and expand to a

(a) A ball and spring model   (b) Film under compression
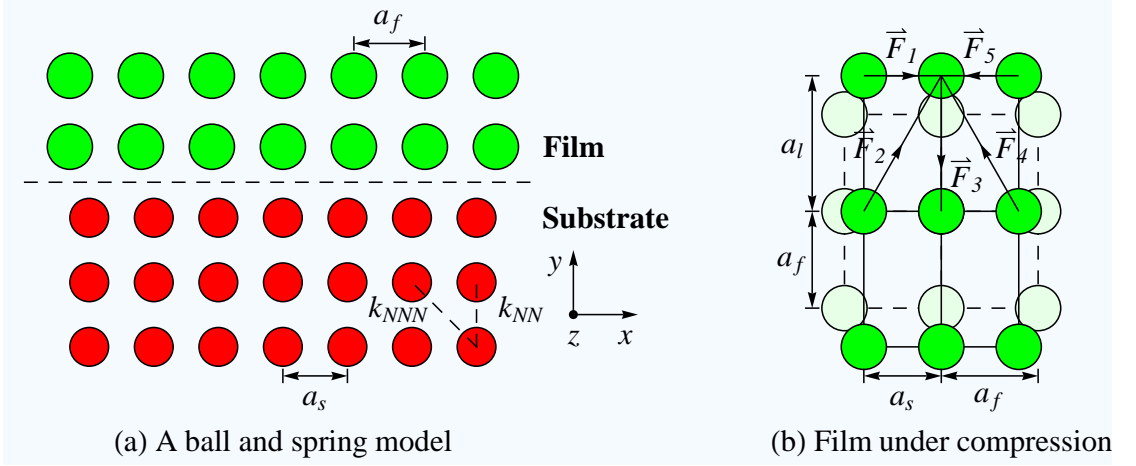
Figure 2.1: Schematic representations: (a) A ball and spring model and (b) film under compression.

distance a_l in the vertical direction. Forces acting on a topmost atom are

$$\vec{F}_1 = k_{NN}(a_f - a_s)\begin{pmatrix} 1 \\ 0 \end{pmatrix},$$

$$\vec{F}_2 = \left|\vec{F}_2\right|\begin{pmatrix} \cos\theta \\ \sin\theta \end{pmatrix},$$

$$\vec{F}_3 = k_{NN}(a_l - a_f)\begin{pmatrix} 0 \\ -1 \end{pmatrix}, \tag{2.1}$$

$$\vec{F}_4 = \left|\vec{F}_4\right|\begin{pmatrix} -\cos\theta \\ \sin\theta \end{pmatrix},$$

$$\vec{F}_5 = -\vec{F}_1.$$

Here $\left|\vec{F}_2\right| = \left|\vec{F}_4\right| = k_{NNN}\left(\sqrt{2}a_f - \sqrt{a_s^2 + a_l^2}\right)$, and $\tan\theta = a_l/a_s$. We assume that the configuration is infinitesimally distorted. Hence, to the first-order, $\cos\theta \approx \sin\theta \approx \sqrt{2}/2$, and $\sqrt{a_s^2 + a_l^2} \approx \sqrt{2}/2(a_f - a_f\epsilon + a_l)$. In an equilibrium, forces are balanced in all directions. In the vertical direction,

$$k_{NNN}(a_f + a_f\epsilon - a_l) - k_{NN}(a_l - a_f) = 0. \tag{2.2}$$

The result yields

$$a_l = a_f + a_f\epsilon\left(\frac{k_{NNN}}{k_{NN} + k_{NNN}}\right). \tag{2.3}$$

An unstrained atom is located at a lattice point denoted by an index (i, j)[1]. The model is subjected to the periodic boundary conditions in x direction; that is $(i + L, j) \equiv (i, j)$, where L is the substrate size. For convenience, we change the coordinates $(i, j) \rightarrow (i)$, $(i + 1, j) \rightarrow (i + 1)$, $(i, j + 1) \rightarrow (i + L)$, and so on. The model is now transformed into a 1D problem.

2.2 Elasticity

When an atom located at lattice point i is under compressive strain (or tensile strain), it is displaced from the lattice point. A displacement $\vec{u}(i) = u_x(i)\hat{x} + u_y(i)\hat{y}$ measured from the lattice point is then non-zero. The energy stored in each spring is proportional to the square of the relative displacement $(\Delta\vec{u})^2$.

2.2.1 The elastic energy

The total elastic energy of the system (E) is the sum of all energies stored in the springs connected to film and substrate atoms,

$$
\begin{aligned}
E &= \frac{1}{2} \sum_i E(i) \\
&= \frac{1}{2} \sum_i \left[E_{xx}(i) + E_{yy}(i) + 2E_{xy}(i) \right].
\end{aligned}
\tag{2.4}
$$

The components $E_{xx}(i)$, $E_{yy}(i)$, and $E_{xy}(i)$ are given by [58]

$$
\begin{aligned}
E_{xx}(i) = \frac{k_{NN}}{2} &\left\{ \delta_{i,i+1} \left[u_x(i+1) - u_x(i) - d_1 \right]^2 \right. \\
&\left. + \delta_{i,i-1} \left[u_x(i-1) - u_x(i) + d_1 \right]^2 \right\} \\
+ \frac{k_{NNN}}{4} &\left\{ \delta_{i,i+1+L} \left[u_x(i+1+L) - u_x(i) - d_1 \right]^2 \right. \\
&+ \delta_{i,i-1-L} \left[u_x(i-1-L) - u_x(i) + d_1 \right]^2 \\
&+ \delta_{i,i+1-L} \left[u_x(i+1-L) - u_x(i) - d_1 \right]^2 \\
&\left. + \delta_{i,i-1+L} \left[u_x(i-1+L) - u_x(i) + d_1 \right]^2 \right\},
\end{aligned}
\tag{2.5}
$$

---

[1]The variables i, j, and k denote a discrete space, while the variables x, y, and z denote a continuous space.

$$E_{yy}(i) = \frac{k_{NN}}{2} \left\{ \delta_{i,i+L} \left[u_y(i+L) - u_y(i) - d_2 \right]^2 \right.$$
$$\left. + \delta_{i,i-L} \left[u_y(i-L) - u_y(i) + d_2 \right]^2 \right\}$$
$$+ \frac{k_{NNN}}{4} \left\{ \delta_{i,i+1+L} \left[u_y(i+1+L) - u_y(i) - d_2 \right]^2 \right.$$
$$+ \delta_{i,i-1-L} \left[u_y(i-1-L) - u_y(i) + d_2 \right]^2$$
$$+ \delta_{i,i+1-L} \left[u_y(i+1-L) - u_y(i) + d_2 \right]^2$$
$$\left. + \delta_{i,i-1+L} \left[u_y(i-1+L) - u_y(i) - d_2 \right]^2 \right\}, \tag{2.6}$$

and

$$E_{xy}(i) = \frac{k_{NNN}}{4} \left\{ \delta_{i,i-1-L} \left[u_x(i-1-L) - u_x(i) + d_1 \right] \right.$$
$$\times \left[u_y(i-1-L) - u_y(i) + d_2 \right]$$
$$+ \delta_{i,i+1+L} \left[u_x(i+1+L) - u_x(i) - d_1 \right]$$
$$\times \left[u_y(i+1+L) - u_y(i) - d_2 \right]$$
$$- \delta_{i,i+1-L} \left[u_x(i+1-L) - u_x(i) - d_1 \right]$$
$$\times \left[u_y(i+1-L) - u_y(i) + d_2 \right]$$
$$- \delta_{i,i-1+L} \left[u_x(i-1+L) - u_x(i) + d_1 \right]$$
$$\left. \times \left[u_y(i-1+L) - u_y(i) - d_2 \right] \right\}. \tag{2.7}$$

An interaction with a neighboring site does not exist if the site lacks an atom, thus

$$\delta_{i,j} = \begin{cases} 1 & \text{if both site } i \text{ and site } j \text{ contain atoms,} \\ 0 & \text{otherwise.} \end{cases} \tag{2.8}$$

A film atom, which is forced to match the natural lattice constant of the substrate, will adapt its lattice spacing with amounts d_1 in x direction and d_2 in y direction, where d_1 and d_2 are

$$d_1 = \begin{cases} a_f - a_s & \text{for film-film and film-substrate bonds,} \\ 0 & \text{for substrate-substrate bonds,} \end{cases} \tag{2.9}$$

and

$$d_2 = \begin{cases} a_f - a_l & \text{for film-film and film-substrate bonds,} \\ 0 & \text{for substrate-substrate bonds.} \end{cases} \tag{2.10}$$

The variables d_1 and d_2 vanish if the film and substrate atoms are of the same kind. Note that the elastic energies in x and y directions can be treated independently if the term E_{xy} in Eq. (2.4) is not present.

2.2.2 Equilibrium constraints

Equilibrium configurations can be found if net forces acting on every atom are zero,

$$\frac{\partial E}{\partial u_x(i)} = F_x(i) = 0, \frac{\partial E}{\partial u_y(i)} = F_y(i) = 0. \tag{2.11}$$

These constraints lead to a system of linear equations:

$$\sum_n K(m,n)u(n) = f(m); \quad m, n = 1, 2, 3, ..., N \tag{2.12}$$

or

$$\mathbf{K} \cdot \vec{u} = \vec{f}. \tag{2.13}$$

The dimensions $(N \times N)$ of the matrix $\mathbf{K}$ account for the two components (u_x, u_y) of the displacements of L atoms, where $N = 2L$. For homoepitaxial systems, $\epsilon = 0$, the RHS of Eq. (2.13) is zero, giving a trivial solution: $\vec{u} = 0$. If $\vec{f} \neq 0$, Eq. (2.13) can be solved by using the inverse of the matrix, $\mathbf{K}^{-1}$. The displacement vector $(\vec{u})$ is simply $\vec{u} = \mathbf{K}^{-1} \cdot \vec{f}$. Finding $\mathbf{K}^{-1}$ is, however, not practical, especially when N is huge. Using a numerical method is more suitable, and a routine to solve the Eq. (2.13) will be discussed in the next chapter. The components $K(m,n)$, $f(n)$, and useful implementation are discussed in more detail in appendix C.

CHAPTER III

Computer Simulations

Computer algorithms are a set of instructions which describe how atoms in the models interact with the environment and evolve in time. The simplest instructions are of the RD model; atoms just randomly fall on the substrate, stick to the first lattice site they arrive, and do not move afterward. For more complicated models [2, 84], adatoms also interact with other atoms and hop to other sites. The crucial thing is that the instructions or rules must reflect the system being studied. In this chapter, we discuss instructions for simulating the heteroepitaxial system. The strain relaxation is also included.

3.1   Microscopic processes

Apart from the deposition process, microscopic processes during the real MBE growth are plenty and complex. The surface diffusion—terrace diffusion, edge diffusion, corner diffusion, dimer diffusion etc.—is thermally activated [88, 89]. To change a system state, atomic process i must overcome an energy barrier called the activation energy E_a, giving a transition rate [2, 36, 90, 91]

$$\nu_i = \nu_{0i}\exp(-E_a/k_B T).\tag{3.1}$$

The activation energy $E_a = E_{\mathrm{saddle}} - E_{\mathrm{min}}$, where E_{saddle} and E_{min} are the energies at the saddle and minimum points, and the prefactor ν_{0i} (attempt frequency) can be calculated from the transition state theory. For the sake of simplicity, we consider only a rate of an individual atom and ignore other rare processes, e.g. the dimer diffusion and exchange mechanism [90].

3.1.1 Deposition

The first process is the deposition process labeled by process (a) in Fig. 3.1. Particles from heated sources are evaporated and directed toward the substrate. The particles, carrying some kinetic energy, arrive on the film surface at random sites. In kMC simulations, a deposited atom arrives on the film surface at a given rate [58]

$$R_d = \left[(s_{\max} + 1)(2s_{\max} + 1)FL \right]/6, \tag{3.2}$$

where F is the deposition flux measured in the unit of monolayer per second (ML· s^{-1}). The maximum hopping distance ($s_{\max}$) corresponds to randomly distributed distance s in the horizontal direction [38], $s = 1, 2, 3, \cdots, s_{\max}$. The deposited atom sticks to the first site it arrives on.

3.1.2 Desorption

The desorption process labeled by process (b) in Fig. 3.1 is the opposite process competing with the deposition process. When the thermal energy, compared to the activation energy E_a, is high enough, surface atoms have some chances to detach from the surface, leaving the sites unoccupy. Generally, the energy required to detach an atom from the surface depends on growth materials and the local surface at which the atom is bound. For example, an atom with a smaller coordinating number of NN and NNN has more probability to desorb, and vice versa. The desorption time—the average time for a desorption event—is proportional to the average time (τ) spent by an atom from the deposition to desorption. It depends on the growth temperature and obeys the Arrhenius law [2, 36] as

$$\tau = \tau_0 \exp(E_d/k_B T). \tag{3.3}$$

The characteristic desorption time (τ_0) and desorption energy (E_d) can be determined from experimental results. For Ga on GaAs(111) substrate at substrate temperature $T = 860 - 960$K [2], the values are approximately $\tau_0 \approx 10^{-14}$ s and
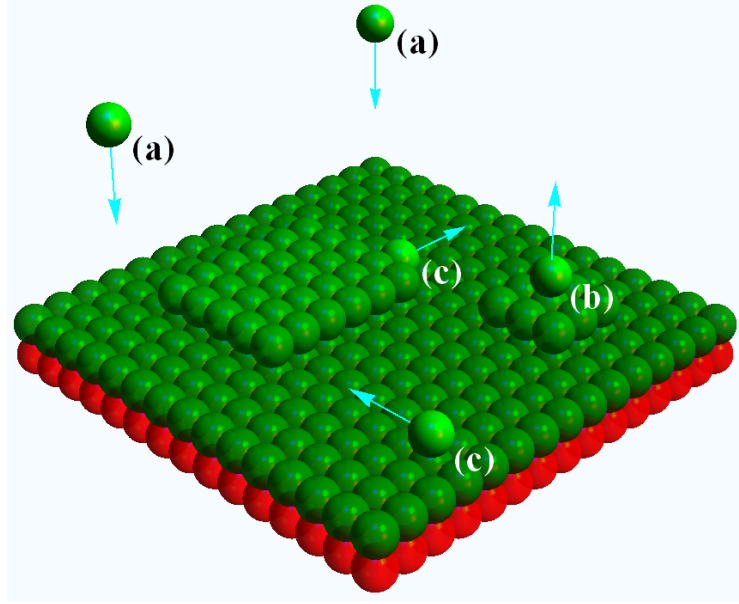
Figure 3.1: Microscopic processes: (a) deposition, (b) desorption, and (c) diffusion.

$E_d \approx 2.5$ eV. The desorption energy (E_d) is much higher than the activation energy (E_a); E_a is less than 1 eV for most materials [2, 36]. Thus, one can expect that the process is not activated under MBE growth conditions. In this work, the growth is under low temperature, and the desorption is neglected.

3.1.3 Diffusion

If deposited atoms arriving on the film surface have more excess kinetic energy, they may travel on the surface and stick to stable positions. Even the atoms already bound with neighboring sites, having the thermal energy from the heated substrate, can break the bonds and search for more stable sites. This process is called the surface diffusion and labeled by process (c) in Fig. 3.1. An atom searching for energetically more favorable sites must firstly overcome the activation energy E_a. The activation energy E_a depends on materials being used and the local surface. To determine the energy, the average number of jumps of surface atoms is counted in a unit time interval. The number also gives the diffusion length, an average distance an atom travels on the surface, and it decays exponentially with the growth temperature. It is conceivable that for an atom detaching from

an edge [see process (c) in Fig. 3.1], it must overcome the activation energy (E_a), plus extra energy E_n for breaking its lateral bond. For kink sites, the detachment is harder, making the probability very low. It is also easier for an atom to move along the edge rather than move away from the edge. The diffusion probability or diffusion rate of atom i obeys the Arrhenius form [2, 91] as

$$R_i = R_0 \exp\left[-(E_a + E_n)/k_B T\right],\tag{3.4}$$

where R_0 is in the order of the Debye frequency ($\approx 10^{13}$ s^{-1}). The rate R_i depends strongly on E_n and growth temperature T. For $T = 600$ K and $E_n = 1$ eV, the rate is 10^8 times smaller than the rate of an atom on the terrace. Once an atom sticks to the edge or kink site, it will stay there for a long time before hopping to other sites. Under most MBE growth conditions, atoms attaching to islands are nearly immobile, making the island growth an irreversible process.

The adatom diffusion is also affected by the anisotropy of the system—moving along one direction is energetically more favorable than moving along another direction [2, 36]. Moreover, an adatom on the edge of an island jumping down needs an additional energy to cross an barrier called the Schwoebel barrier [2]. It is more probable for the adatom to bounce back when it meets the edge, and the process is known as the diffusion bias.

In the heteroepitaxial system, the adatoms experience another bias: the strain from the film surface. The gradient of strain drives the adatoms with additional elastic energy difference ΔE. Taking the energy into account, the total energy required for an adatom to break its lateral bonds and hop to neighboring sites is $E_n + E_0 - \Delta E$. In this work, $E_n = nE_b$, and the diffusion rate of the adatom i follows the form [38, 58]

$$R_i = R_0 \exp\left[-(n_i E_b + E_0 - \Delta E_i)/k_B T\right],\tag{3.5}$$

where $R_0 = 12D_0/\left[a_s^2(s_{\max} + 1)(2s_{\max} + 1)\right]$ is a characteristic vibrational frequency, E_b is the binding energy with NN and NNN per bound, and E_0 is the surface binding energy. The values of the constants are chosen so that they are appropriate for Ge/Si system (see appendix B). The bindings with NN and NNN are the

same that is $n_i =$ the number of NN + NNN, and $\Delta E_i = E$(with the adatom i) $-$ E(without the adatom i) is the elastic energy difference when site i is occupied versus unoccupied. The probability that adatom i is likely to hop is associated with the diffusion rate R_i. In this work, the system is isotropic, and the Schwoebel barrier is not included to make sure that island formation is not caused by the diffusion bias.

3.2 Strain relaxation

The elastic energy in Eq. (2.4) and energy difference in Eq. (3.5) can be calculated if the displacements in Eq. (2.13) are known. The displacement vector $\vec{u}$ can be obtained in both exact and numerical solutions. In most cases including in this work, numerical methods seem to have more advantages, especially when the number of unknown variables is very large. But the numerical method has its own problem, for example the roundoff errors that may affect true solutions. Some methods that have been used to solve a system of linear equations are the Gauss-Jordan elimination, LU decomposition, and conjugate gradient (CG) methods [92]. A routine of the methods is quite general and can be found elsewhere[1]. We use a variant of the CG method, the biconjugate gradient stabilized (Bi-CGSTAB) method [93], to solve Eq. (2.13). The details, including an algorithm of the Bi-CGSTAB method, energy localization, and local relaxation, will be given in this section.

3.2.1 Solving a system of linear equations

The CG method is a routine for solving a system of linear equations. This method has successfully been applied to the iterative technique and capable of solving large sparse systems which are not suitable for the direct methods such

---

[1]BLAS (Basic Linear Algebra Subroutine) and other variants, LAPACK and LINPACK, are standard libraries for performing linear algebra operations.

as the Gauss-Jordan elimination. The original CG method requires symmetric $(\mathbf{A}^T = \mathbf{A})$, positive-definite ($\vec{x}^T \cdot \mathbf{A} \cdot \vec{x} > 0$ for all non-zero vector $\vec{x}$ in $\mathbb{R}^n$) n-by-n matrix $\mathbf{A}$, where $\vec{x}^T$ denotes the transpose of $\vec{x}$. The biconjugate gradient (Bi-CG) method is more generalized to non-symmetric matrices; but, the Bi-CG method is less stable than the Bi-CGSTAB method. The Bi-CGSTAB method is a simple, but powerful, algorithm that combines two important parts: the fast, converging Bi-CG and stabilizing effect. The Bi-CGSTAB method was developed by Henk A. van der Vorst [93].

From Eq. (2.13), $\mathbf{K} \cdot \vec{u} = \vec{f}$, an algorithm of the Bi-CGSTAB method can be illustrated as follows [93]:

1) Set initial values for $i = 0$

    1.1) Guess $\vec{u}_i$, e.g. $\vec{u}_i = \vec{u}_{\text{old}}$

    1.2) $\vec{r'} = \vec{r}_i = \vec{f} - \mathbf{K} \cdot \vec{u}_i$

    1.3) $\rho_i = \alpha_i = \beta_i = \omega_i = 1$

    1.4) $\vec{v}_i = \vec{p}_i = \vec{s}_i = \vec{t}_i = 0$

2) For $i = 1, 2, 3, ...$

    2.1) $\rho_i = \vec{r'} \cdot \vec{r}_{i-1}$

    2.2) $\beta_i = (\rho_i/\rho_{i-1})(\alpha_{i-1}/\omega_{i-1})$

    2.3) $\vec{p}_i = \vec{r}_{i-1} + \beta_i(\vec{p}_{i-1} - \omega_{i-1}\vec{v}_{i-1})$

    2.4) $\vec{v}_i = \mathbf{K} \cdot \vec{p}_i$

    2.5) $\alpha_i = \rho_i/(\vec{r'} \cdot \vec{v}_i)$

    2.6) $\vec{s}_i = \vec{r}_{i-1} - \alpha_i\vec{v}_i$

    2.7) $\vec{t}_i = \mathbf{K} \cdot \vec{s}_i$

    2.8) $\omega_i = (\vec{t}_i \cdot \vec{s}_i)/(\vec{t}_i \cdot \vec{t}_i)$

    2.9) $\vec{u}_i = \vec{u}_{i-1} + \alpha_i\vec{p}_i + \omega_i\vec{s}_i$

    2.10) If $\vec{u}_i$ is accurate enough then exit 2)

    2.11) Otherwise $\vec{r}_i = \vec{s}_i - \omega_i\vec{t}_i$

    2.12) Go to 2) after one step

A residual error relative to vector $\vec{f}$ is defined as

$$R = \frac{(\vec{r} \cdot \vec{r})}{(\vec{f} \cdot \vec{f})}. \tag{3.6}$$

In step 2.10), the recurrent loop i exits 2) if $R \leq R_{\text{tol}}$, where R_{tol} is a tolerance. The accuracy of $\vec{u}$ depends on the choice of the tolerance R_{tol}. Accounting for the accuracy and efficiency, $R_{\text{tol}} = 10^{-2}$ is enough [58].

3.2.2 An approximation of the elastic energy

We can see that in Eq. (3.5), the elastic energy difference (ΔE_i) is calculated twice for each adatom i. There must be at least L times for calculating ΔE_i for each time step. The calculation is the bottleneck of the simulations, consuming most of the computational time. This is the global effect in which all atoms are involved when adatom i is removed or added. The effect is strong near the site and small far away from the site. In other words, when atom i is removed (or added), neighboring atoms notice the change while other atoms, being far from the site, will be little affected. The elastic energy difference ΔE_i can be, therefore, approximated as a "local" effect. We note that the elastic energy in Eq. (2.4) can be written as

$$E = \frac{1}{2} \sum_i e_i, \tag{3.7}$$

where e_i is the energy stored in the springs connected to adatom i. We assume ΔE_i to be dependent on a local variable [57, 58] as

$$\Delta E_i = c(n_i, h_i)e_i + O(e^2) + \cdots$$
$$\approx c(n_i, h_i)e_i. \tag{3.8}$$

The local variable $c(n_i, h_i)$ depends on the number of NN + NNN, n_i, and height of adatom i (h_i). Moreover, when the adatom is far away from the substrate, the influence from the substrate is small. In this work, $c(n_i, h_i)$ is given by

$$c(n_i, h_i) = \begin{cases} 0 & \text{for } n_i \leq 2, \\ c(6, h_i) & \text{for } n_i > 6, \\ c(n_i, h_i) & \text{for } h_i \leq 3, \\ c(n_i, 3) & \text{for } h_i > 3. \end{cases} \tag{3.9}$$

The values (see Table 3.1) of $c(n_i, h_i)$ are calculated from the true ΔE_i with the full relaxation; $\Delta E_i^{\text{full}} = c(n_i, h_i)e_i$, and averaged over $\approx$ 4,000-100,000 samplings depending on its occurrence. In some cases, the probability of finding adatoms with n_i at the height h_i is too low to calculate $c(n_i, h_i)$. These situations are denoted by the sign (*) in Table 3.1 and the values of $c(n_i, h_i)$ are taken from calculation using smaller h_i (listed in the higher rows in the table) instead. The elastic energy difference profiles of surface atoms in Fig. 3.2 are calculated using the approximation versus full relaxation and are shown in Fig. 3.3.

The solid and dotted lines represent ΔE_i obtained from the full relaxation with the tolerances $R_{\text{tol}} = 10^{-6}$ and $R_{\text{tol}} = 10^{-2}$, respectively. For the full relaxation, the results are nearly the same for both tolerances. In the remainder of this work, $R_{\text{tol}} = 10^{-2}$ is used in the Bi-CGSTAB algorithm. The dashed line represents ΔE_i obtained from Eq. (3.8) with $R_{\text{tol}} = 10^{-2}$. The result indicates that ΔE_i can be approximated locally. The remaining variables which must be sufficiently accurate are the energies e_i. In an equilibrium, the energy e_i is stored in the springs connected to adatom i. When the adatom i is removed, one expects that the elastic energy difference ΔE_i would be proportional to e_i. Since before hopping or depositing an atom, the film configuration is in an equilibrium state, the energy e_i is therefore available for ΔE_i. The full relaxation required to update the energy e_i is only one time instead of L times for each time step. The relaxation for updating the energies e_i is done after hopping an adatom to a

h_i	$n_i = 3$	$n_i = 4$	$n_i = 5$	$n_i = 6$
0	1.51	1.63	2.16	1.72
1	*	1.58	1.81	1.75
2	*	1.57	1.85	*
3	*	1.47	1.80	*

Table 3.1: The values of local variable $c(n_i, h_i)$. The sign (*) denotes situations when $c(n_i, h_i)$ cannot be calculated and the values of c should be taken from calculations with smaller h_i (listed in the higher rows).
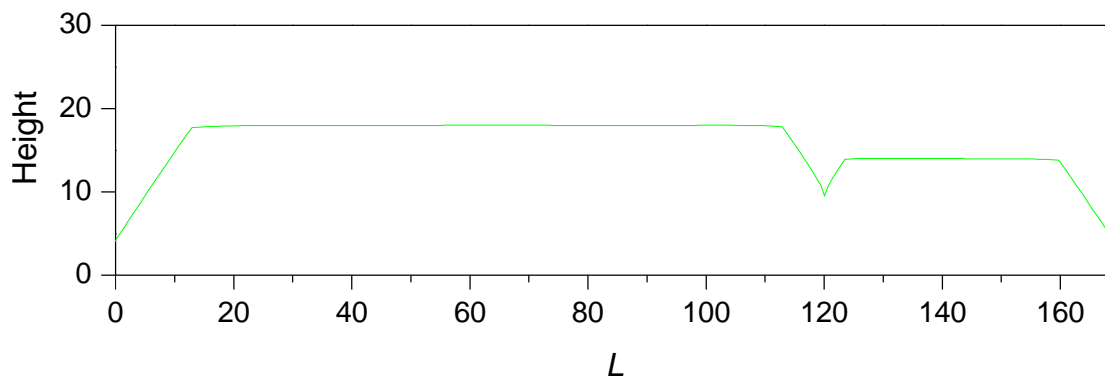
Figure 3.2: A typical configuration of surface atoms.
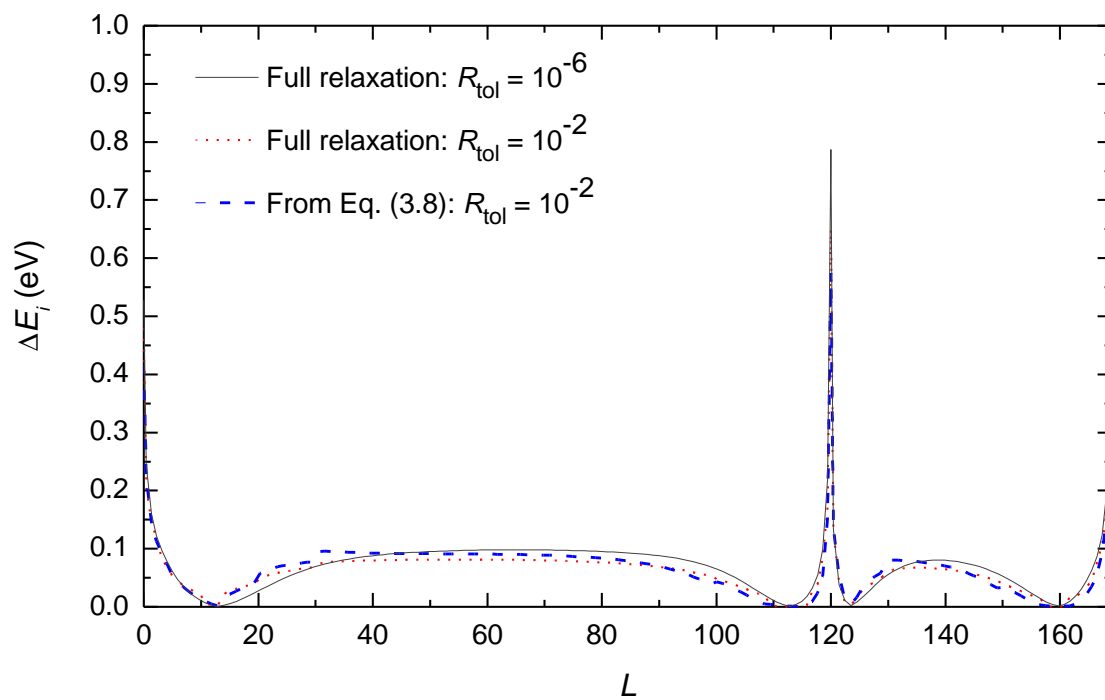
Figure 3.3: The elastic energy difference profiles of surface atoms in Fig. 3.2.

neighboring site, depositing an atom on the film surface, and/or changing the configuration of surface atoms. The approximation reduces the computational time considerably. A careful selection of whether the hopping atom is rejected or not can further increases the accuracy of the approximation. However, the rejection rate is very small, and does not really alter the final results [58].

3.2.3 Local relaxation

The approximation would be enough for a small system with submonolayer growth. For a larger system, the growth is still difficult to simulate. However, we can further reduce computational time by using local relaxation. Although the full relaxation is required to correct the configuration of surface atoms and update the energies e_i when an event (diffusion or deposition) is completed, for large L, the process occurs in a small area relative to the system size and can be considered as a local event. The local relaxation allows atoms in a certain area to relax and rearrange their positions, while atoms outside are not affected.

Fig. 3.4 shows a schematic representation of the local relaxation. Atoms in a box, whose width is denoted by W and whose height is denoted by H, centered at the blue atom are allowed to relax, while atoms outside are not affected. The effect of the local relaxation for different sizes of the box is shown in Fig. 3.5. The energy e_i is obtained from adding atom i to the film surface in Fig. 3.2 and relaxing surface atoms in the box centered at the atom i. The solid line represents the energy profile obtained from the full relaxation. For W = 75 and H = 7 (dotted line), the energy profile is identical with that of the full relaxation. The sharp changes relative to the energy profile of the full relaxation are found when W = 25 and H = 5 (dashed line). The local relaxation becomes unreliable when W = 15 and H = 5 (dotted dashed line). It is clear that the size of the box used in the local relaxation strongly effect the displacements and hence the energies e_i unless the local relaxation area is large. In this work, the box with W = 25 and H = 5 is used for the local relaxation. After every 100 time steps, atoms in the five rows measured from the topmost atom are relaxed to minimize local residues.
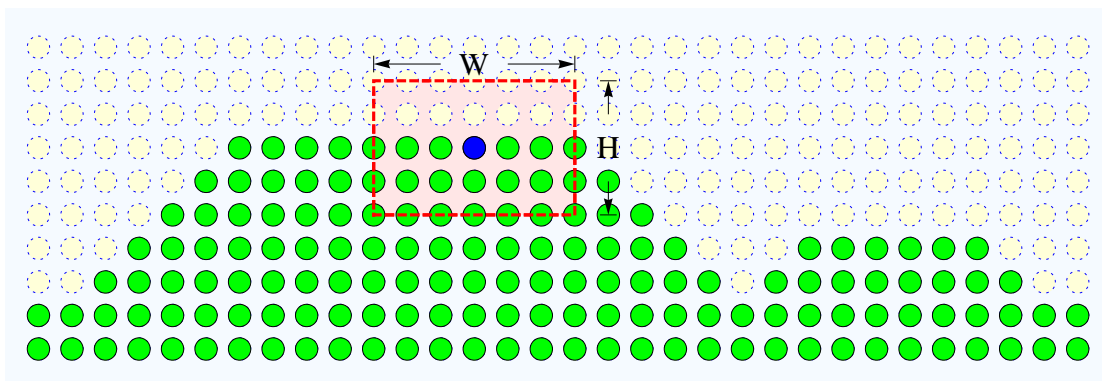
Figure 3.4: A schematic representation of the local relaxation. Atoms in a box, whose width is denoted by W and whose height is denoted by H, centered at the blue atom are allowed to relax.
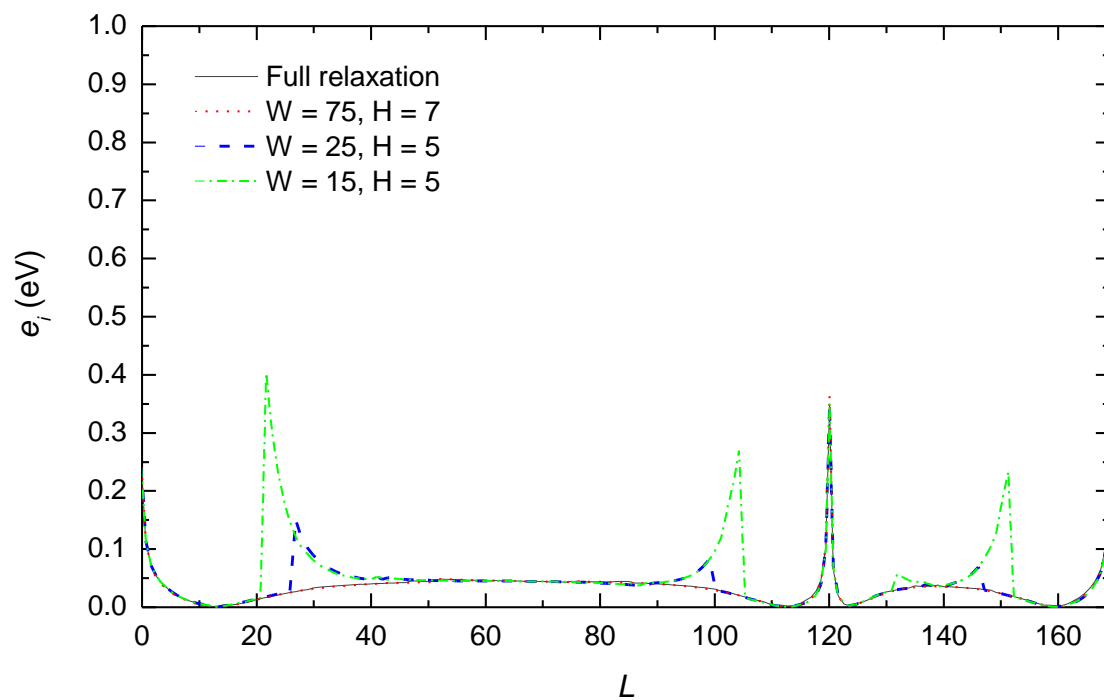
Figure 3.5: The energy profiles obtained from relaxing surface atoms in Fig. 3.2 for various local relaxation areas.

We also investigate the effects of the local relaxation on film surfaces and found that the final results are independent of the local relaxation areas. The details will be discussed in the next chapter.

3.3 Kinetic Monte Carlo simulations

The Monte Carlo (MC) method is a well-known method used in various branches of science [83, 91]. The MC method is generally referred to computational algorithms that use random numbers (so-called quasi-random numbers) to solve problems. Historically the method is used to estimate integrals in high-dimensional spaces or other poorly-behaved integrals that cannot be solved by ordinary methods.

In statistical physics, we need to calculate the partition function of a system [83, 91, 94],

$$Z = \sum_{\mu} \exp(-E_{\mu}/k_B T), \tag{3.10}$$

where E_{μ} is the energy of the system in state μ. The summation runs over all possible states of the system. The probability that the system is in the state μ is

$$P_{\mu} = \frac{1}{Z}\exp(-E_{\mu}/k_B T). \tag{3.11}$$

The average of thermodynamic parameter A is the sum of all possible values A_{μ} and weighted according to its probabilities P_{μ} as

$$\langle A \rangle = \frac{1}{Z} \sum_{\mu} A_{\mu}\exp(-E_{\mu}/k_B T) = \sum_{\mu} P_{\mu}A_{\mu}. \tag{3.12}$$

Unfortunately, the calculation of $\langle A \rangle$ in Eq. (3.12) is possible only when the system is small. For the Ising model on N lattice sites, there are 2^N possible configurations, and the configurations increase quickly with N. To overcome this problem, the MC method is used to generate n independent states. The parameter A is then averaged over the states,

$$\langle A \rangle_n = \frac{1}{n} \sum_{i=1}^{n} A_i. \tag{3.13}$$

If these states are mostly distributed in the system, in the limit of $n \to \infty$, each state is weighted by its Boltzmann factor, $e^{-E/k_B T}$. The average converges to the thermodynamic average as

$$\langle A \rangle_n = \langle A \rangle + O(n^{-1/2}). \tag{3.14}$$

Mostly the MC algorithms focus on how to generate such states whose its distribution obeys the Boltzmann distribution. Any transition rate which satisfies the detailed balance of the master equation is acceptable [83]. The Markov chain of states is widely used to generate transition rates [83, 91]. The well-known algorithm that uses the Markov chain of states to generate independent states is the Metropolis algorithm [83, 91]. The problem of the MC method with time-driven algorithms is that the acceptance ratio of the transition rates is very small at low temperatures. Once the system is trapped in a ground state at low temperatures it will spend a long time in the state. Many transition rates end up with rejection, wasting computational time before a new state is made.

The kinetic Monte Carlo (kMC) also called the continuous time Monte Carlo method with event-driven algorithms [83, 91] accepts a state at each step and calculates back how much time to produce such the state to occur, and the system advances according to the time. The acceptance ratio of the transition rates is always one, which speeds up the simulations. In the MC method, we can define a simulation time as the Monte Carlo step per site (MCS/site) [83]. But when the system reaches an equilibrium, there is no connection between the simulation time and physical time. Since in the equilibrium, the system is independent of time. In order to state how fast the system evolve, the physical time must be interpreted.

3.3.1 A definition of physical time

From Eq. (3.2) and Eq. (3.5), the total rate per unit time is

$$R = \sum_{k=0}^{L} R_k, \tag{3.15}$$

where $R_0 = R_d$ is the deposition rate, and $R_{k \neq 0}$ are the diffusion rates. The probability that any event is not observed in the time interval $(t_0 = 0, t)$ [83, 91, 95] is

$$P(t) = \exp(-Rt). \tag{3.16}$$

This equation is also known as the survival probability. The exponential decay law is found in many systems in nature such as the radioactive decay. The probability that any event is observed in the interval $(t, t + dt)$ is $p(t)dt$. Thus

$$\int_{t_0=0}^{t} p(t)dt = 1 - P(t) \tag{3.17}$$

is the probability that any event is observed in the time interval $(t_0 = 0, t)$. One finds that $p(t) = -dP(t)/dt = R\exp(-Rt)$. The waiting time between any two events is given by

$$\tau = \int_0^\infty tp(t)dt = \frac{1}{R}. \tag{3.18}$$

An event occurs, on average, after the waiting time τ. The total rate R will not be a constant during the simulations. Instead, the waiting time τ is drawn from a Poisson distribution [83, 95] as

$$\tau = -\frac{\ln(\rho_1)}{R}, \tag{3.19}$$

where ρ_1 is a random number uniformly distributed in the interval $(0, 1)$. The physical time advanced in a single step is then $t \to t + \tau$.

3.3.2 The n-fold way algorithm

The n-fold way algorithm is an event-driven algorithm introduced by Bortz, Kalos, and Lebowitz in 1975 [96] for Ising spin systems. The idea of the algorithm is to avoid rejected events during the simulations. An accepted event is then found at each step. In general, the algorithm has a following routine to select an event. Firstly, the rates R_i and the total rate $R = \sum_{i=0}^{L} R_i$ are calculated. Then the cumulative rates $\sum_{i=0}^{k} R_i$ (see Fig.3.6) are drawn. Next, an event k is selected such that $\sum_{i=0}^{k} R_i \geq \rho_2 R > \sum_{i=0}^{k-1} R_i$, where ρ_2 is a random number uniformly distributed in the interval (0,1). Finally, the event k is executed and time t is updated, $t \rightarrow t+\tau$. KMC simulations with the n-fold way algorithm are illustrated as a flowchart in Fig. 3.7.

3.4 Quantities of interest

When we study the roughening of film surfaces, the first thing we might need to know is the surface morphology of the grown films. The surface morphology tells us qualitatively about the film roughness and film pattern. However, the roughness may be interpreted differently. In fact, the roughness depends on the scale of the system we observe. Moreover, to extract a characteristic feature of the films, statistical quantities must be measured.

The critical thickness h_c is one of the statistical quantities we are interested in. It is defined as a thickness at which the transition from a 2D flat layer to 3D islands firstly occurs. The strain is partially relieved after the formation of 3D
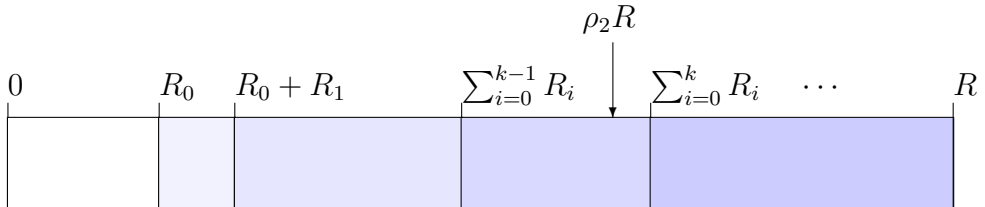
Figure 3.6: A schematic representation of an event selection.
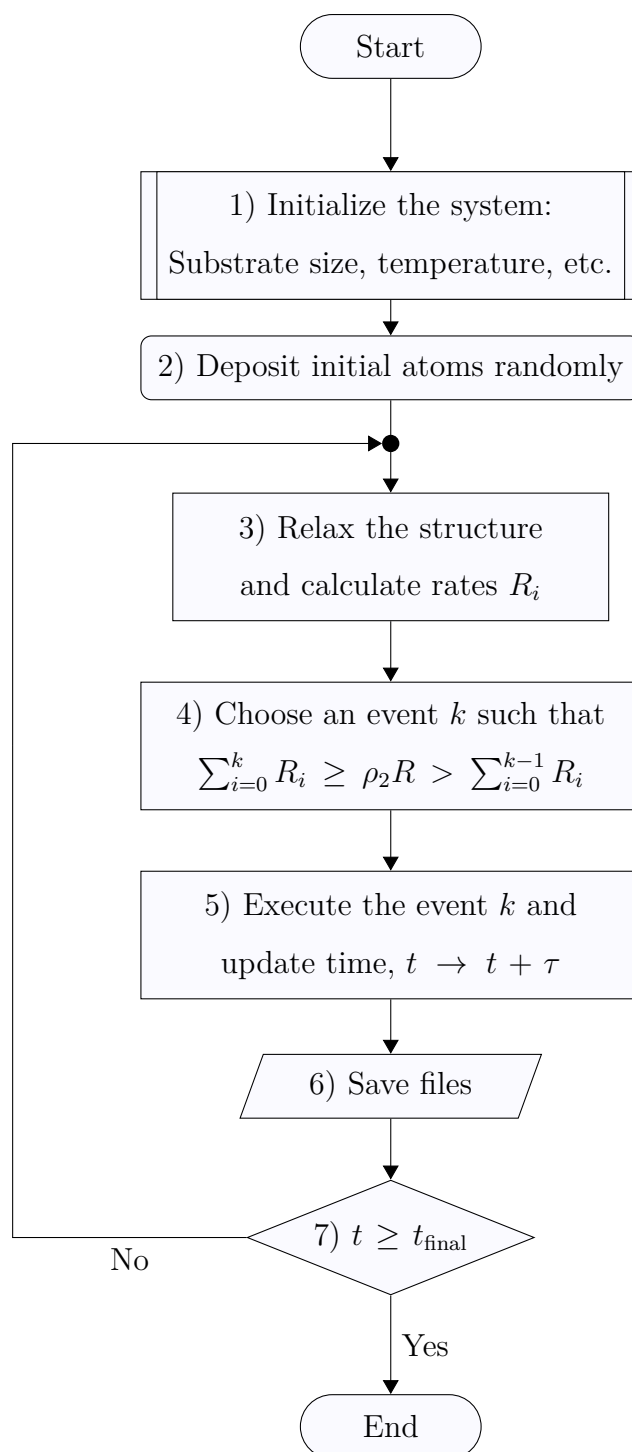
Figure 3.7: A flowchart of kMC simulations with the n-fold way algorithm.

islands. The elastic energy is then decreased after the critical thickness. In this work, the critical thickness is calculated from an average thickness (θ) at which the elastic energy per atom ($E/\theta L$) reaches its maximum value.

To study the film surfaces quantitatively, an island size (l) and a number of islands (n) are measured. Islands which have a thickness greater than 2 ML ($h > 2\text{ML}$) are counted, and the island base size is measured. The island size and number of islands characterize the film surfaces.

Finally, all statistical quantities presented here are averaged over 20 independent runs.

CHAPTER IV

Results and Discussions

In this chapter, we discuss our numerical results of films grown on flat substrates at different lattice mismatches, deposition fluxes, and growth temperatures. The main goal is to investigate effects of the growth conditions on the surface morphology, island size, number of islands, and critical thickness. we also compare our results with theoretical, experimental, and other computational results.

4.1 Introduction

Firstly, we begin this chapter with an introduction, which explains how the strain can bias the adatom diffusion. We then discuss some results normally observed in heteroepitaxial systems. This will help us understand results in the next sections. The effects of the local relaxation are also mentioned. Finally, we summarize the results of this section.

4.1.1 Strained films

To understand how the strain bias the adatom diffusion, we firstly look at an equilibrium configuration of strained films. Fig. 4.1 shows a strained film (green) and substrate (red) before the full relaxation. The film is under compressive strain; $a_f > a_s$. We only want to see where the stain is mostly contributed to. The strain distribution in the film and substrate is the same for all values of the lattice mismatch, but the strength of the strain depends on the lattice mismatch.

Figure 4.1: An equilibrium configuration of the strained film (green) and substrate (red) before the full relaxation.

Fig. 4.2 shows the same configuration as in Fig. 4.1 after the full relaxation. The displacements in the x- and y-direction can be seen more clearly in Fig. 4.3 and Fig. 4.4. In the x-direction, it is not surprising that the displacements are symmetric around the center of the structure because of the periodic boundary conditions. Film atoms in the vicinity of the film-substrate interface are bound with the substrate atoms and do not move much. The upper atoms, however, are free to expand outward and the displacements reach maximum values at the topmost layer. The values are particularly large compared to the lattice constant of the film. In the y-direction, the displacements are small. Atoms change their positions slightly in order to compensate the displacements in the x-direction so that the forces acting on the atoms in both directions are zero. Notice that the substrate atoms also move from the lattice points because two topmost layers of the substrate are allowed to relax. The calculated displacements can only describe relative displacements of atoms, but cannot tell us completely about the strain in the system. For Hookean springs, the relative displacements indicate the elastic energy associated with the springs.

Fig. 4.5 shows the density of the energies e_i— the energies stored in the springs connected to film and substrate atoms. Although the displacements are large at the upper layers, the energies contributed to the area are quite low. For adatoms, the upper area is energetically more preferable. In contrast, the energy density is high at the film-substrate interface, especially at the kink sites. The result comes from the fact that, at the interface, the film is forced to take the lattice constant of the substrate. The area is energetically undesirable for adatoms.

Figure 4.2: The same configuration as in Fig. 4.1 after the full relaxation.

Figure 4.3: The displacements of film and substrate atoms in x-direction. The colors indicate values of the displacements.

Figure 4.4: The displacements of film and substrate atoms in y-direction. The colors indicate values of the displacements.

Figure 4.5: The density of the energies e_i. The colors indicate values of the energies.

The energies, e.g. ~ 1.5 eV, compared with the binding energies, are quite significant and can effect the adatom diffusion. Adatoms at the kink sites are highly active and have more chance to hop to neighboring sites. The diffusion current of adatoms is driven toward the topmost layer. This current promotes the island formation [64].

4.1.2   Homoepitaxy vs. heteroepitaxy

We now consider the morphological evolution of homoepitaxial films versus heteroepitaxial films. The objective is to show that islands come purely from the influence of the strain in the system and not from statistically rough surfaces. The system size is set to $L = 1000$ sites unless specified otherwise. Film surfaces are observed every 1 ML until the coverage (θ) is equal to $\theta = 10$ ML. The temperature (T) and deposition flux (F) are set to be $T = 600$ K and $F = 1.0$ ML·s^{-1}, respectively.

Film surfaces at various θ for the homoepitaxial growth with $\epsilon = 0.0\%$ are shown in Fig. 4.6(bottom). There is no strain in the system. As we expected, the film surfaces are statistically flat from the beginning to the end of growth, indicating the layer-by-layer growth mode. The results show that the selected growth conditions are appropriate for homoepitaxial systems to grow flat surfaces. If the surface morphology of heteroepitaxial films, using the same growth conditions, is different from the result, it will be caused by the strain in the systems.

Fig. 4.6(top) shows film surfaces at various θ for the heteroepitaxial growth with $\epsilon = 4.0\%$. It is clear that the surface morphology is very different from the one observed in the homoepitaxial system. In early stages of the growth, the film surfaces are rather flat, then 2D islands form at $\theta \sim 4$ ML. The island size slightly increases with the coverage, while the number of islands remains the same.

It should be noted here that the island size and number of islands are measured directly from the film surfaces in Fig. 4.6(top). The critical thickness (h_c), however, cannot be measured directly from the film surfaces. Generally, film sur-

Figure 4.6: Homoepitaxial films (bottom) with $\epsilon = 0.0\%$ versus heteroepitaxial films (top) with $\epsilon = 4.0\%$ at $T = 600$ K and $F = 1.0$ ML·s^{-1}. The coverage (θ) is $\theta = 1 - 10$ ML and increases every 1 ML.

faces become rough when the transition from a 2D flat layer to 3D islands takes place at a critical thickness. One can, therefore, define the critical thickness as a thickness where the film surfaces become rough (or deviate from the flat surface). But the "rough" films may be interpreted differently and vary from one to another. As we mentioned earlier, the critical thickness in this work is defined from a thickness where the total elastic energy per atom ($E/\theta L$) reaches its maximum value.

Fig. 4.7 shows the total elastic energy per atom versus the coverage for the heteroepitaxial growth shown in Fig. 4.6(top). The energy increases rapidly in the early stages and reaches its maximum value at $\theta \sim 5.5$ ML (an average thickness), in which we define the critical thickness (h_c). After the critical thickness, 2D islands are more clearly seen. It is important to mention here that the total elastic energy per atom does not always reach its maximum value. With some growth conditions, the total elastic energy per atom never decreases (at least up to $\theta = 10$ ML). In these cases, critical thickness h_c cannot be identified.

The island formation can be described in a context of the total elastic energy per atom. In early stages of the growth, strain accumulates as the thickness increases. The strained surface is still flat against stress suppression. When the strain increases further, the flat surface becomes energetically undesirable at a
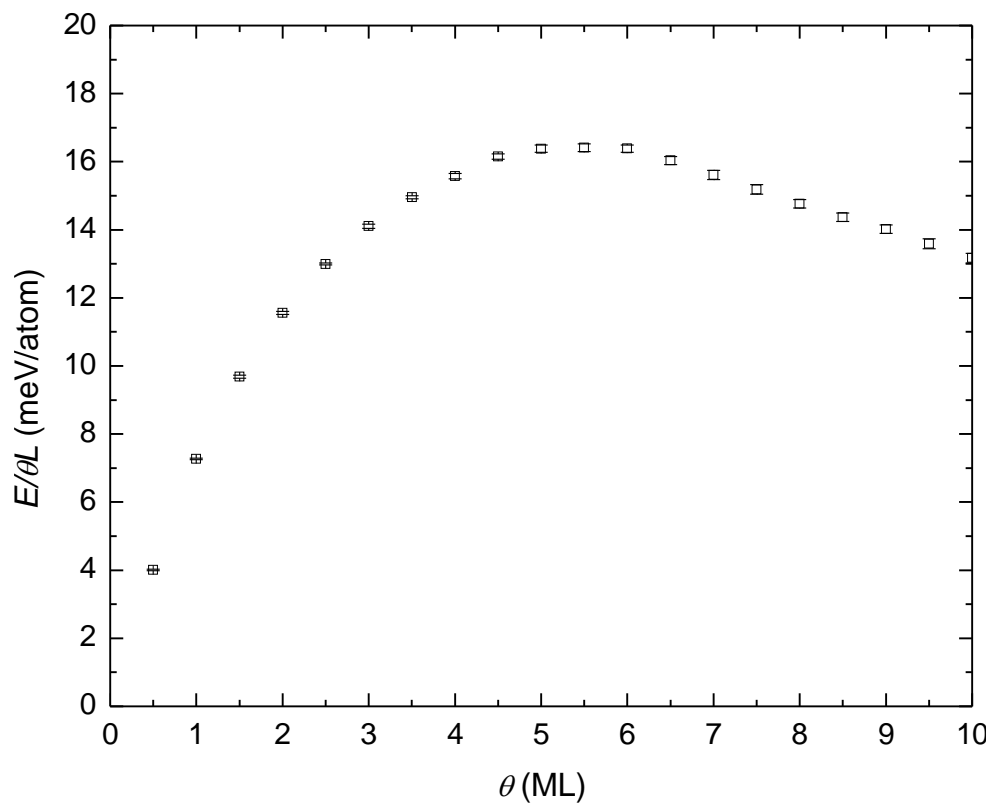
Figure 4.7: The total elastic energy per atom ($E/\theta L$) versus the coverage (θ) of films grown at the same conditions as the films in Fig. 4.6(top).

critical thickness. From previous results, adatoms at kink sits are highly active and can hop easily to upper layers. The adatom diffusion promotes the island formation in this stage [64]. Since the upper layers are more preferable for adatoms, the total elastic energy is decreased after the islands are formed [8, 40, 41]. The surface configuration is stable, and the growth process is almost irreversible. The island formation is more consistent with the island nucleation theory [8], which is observed at low temperatures and large lattice mismatches [11, 38], than the ATG instability [37] observed at high temperatures and small lattice mismatches [12, 13, 15, 38].

4.1.3 Local relaxation bias

We have shown some preliminary results of the homoepitaxial growth versus the heteroepitaxial growth. But for the heteroepitaxial growth, how do we know that the results are not affected by the local relaxation? In some cases, the local relaxation is not appropriate for a local width (W) and a local height (H) (see Fig. 3.5). In this subsection, we discuss effects of the size (W and H) used in local relaxation and show that our final results do not depend on the value of W and H. The growth conditions are still $T = 600$ K, $F = 1.0$ ML·s^{-1}, and $\epsilon = 4.0\%$. We believe that our conclusions also holds for other growth conditions as well. Fig. 4.8 shows film surfaces of the heteroepitaxial growth for various values of local width W and local height H. The surface morphologies are nearly identical. This is the first sign indicating that effects of the size of local relaxation is weak.

To better quantify our results, we consider the total elastic energy per atom ($E/\theta L$) as a function of the coverage (θ) shown in Fig. 4.9. The results (except for W = 125, H = 7) are independent of the values of W and H. For W = 125 and H = 7, the strain relaxation seems to be more efficient, i.e. the total elastic energy of the system is lower. However, the critical thicknesses (h_c) are approximately equal for all values of W and H. The thicknesses are estimated to be $h_c = 5.7 \pm 0.1$ ML (W = 15, H = 5), $h_c = 5.4 \pm 0.1$ ML (W = 25, H = 5), $h_c = 5.2 \pm 0.1$ ML (W = 75, H = 5), and $h_c = 5.4 \pm 0.1$ ML (W = 125, H = 7).

Figure 4.8: Film surfaces at $T = 600$ K, $\epsilon = 4.0\%$ and, $F = 1.0$ ML·s^{-1} for different local relaxation areas: (a) W = 15, H = 5, (b) W = 25, H = 5, (c) W = 75, H = 5, and (d) W = 125, H = 7.
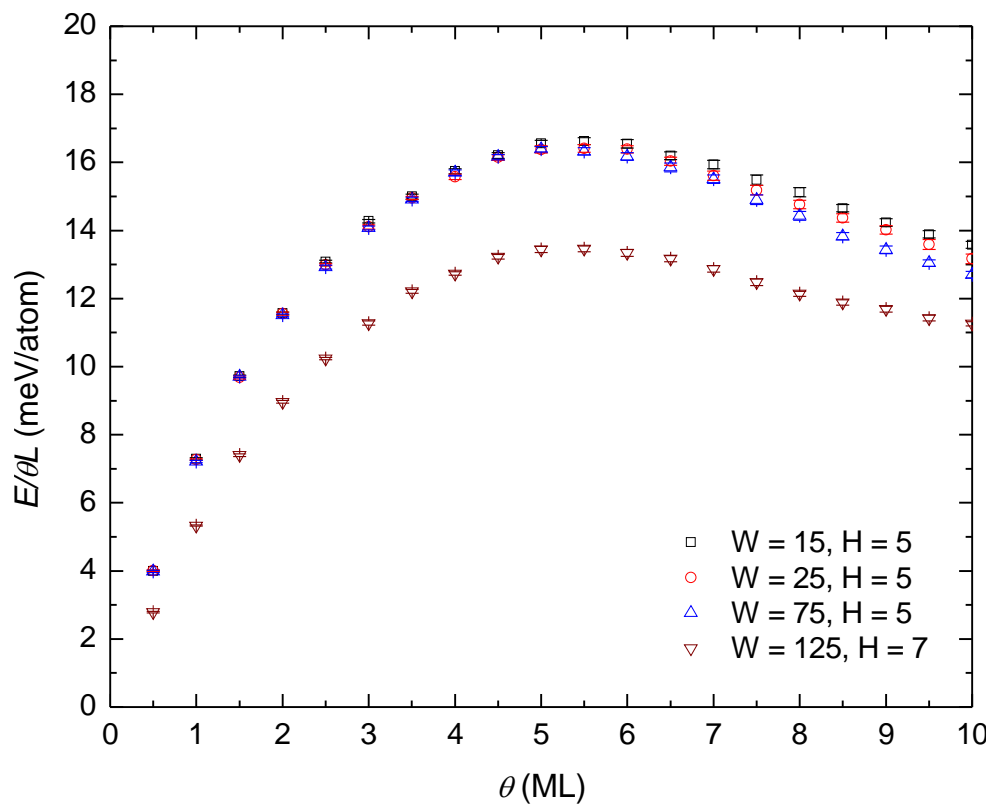
Figure 4.9: The elastic energy per atom $(E/\theta L)$ as a function of the coverage (θ) from heteroepitaxial growth with various local relaxation areas.

Fig. 4.10 and Fig. 4.11 show the island size (l) and number of island (n) as a function of the coverage (θ). The island size increases with the coverage and saturates after $\theta \sim 6$ ML. The saturation values are approximately the same, e.g. $l \sim 46$ sites at $\theta = 10$ ML. The number of islands increases rapidly with the coverage and then decreases abruptly after $\theta \sim 2$ ML. At $\theta \sim 2-5$ ML, the effect of the local relaxation size is visible. The number of islands saturates after $\theta \sim 6$ ML with $n \sim 18$ islands at $\theta = 10$ ML for all values of W and H.

Although here we emphasize on effects of the local relaxation, it is worth noting that the growth can be divided into three regimes. At $\theta \sim 0-2$ ML, adatoms just attach to neighboring sits to form "small" islands. The islands spread throughout the substrate as θ increases. The number of islands then increases quickly, while the island size slightly increases. At $\theta \sim 2-5$ ML, small islands begin to merge together. After that the number of islands decreases, and the island size increases accordingly. The islands are not fully formed in this regime because the elastic energy is still increasing. At $\theta \sim 5-10$ ML, the islands reach stable sizes and become fully formed. The island size and number of islands do not change further. In this regime, adatoms hop to upper layers where the strain is small. The total elastic energy per atom ($E/\theta L$) as a function of coverage θ is then decreased.

As we mentioned, islands are unstable at the intermediate regime ($\theta \sim 2-5$ ML). The fluctuation of the island size is then high, which can be seen from the standard deviation of mean ($\sigma_N = \sigma/\sqrt{20}$) in the inset of Fig. 4.10. When islands reach stable sizes, this quantity become smaller. We can also determine the critical thickness from the thickness at which the fluctuation reaches its maximum value.

In conclusion, the local relaxation seems to slightly affect the results in the early and intermediate regimes ($\theta \sim 0-5$ ML) where islands have not been fully formed and hence are not of our interest. In the saturation regime ($\theta \sim 5-10$ ML), however, we conclude that the size of the local relaxation does not have any effect on our final results. At $\theta = 10$ ML, the critical thickness, island size, and number
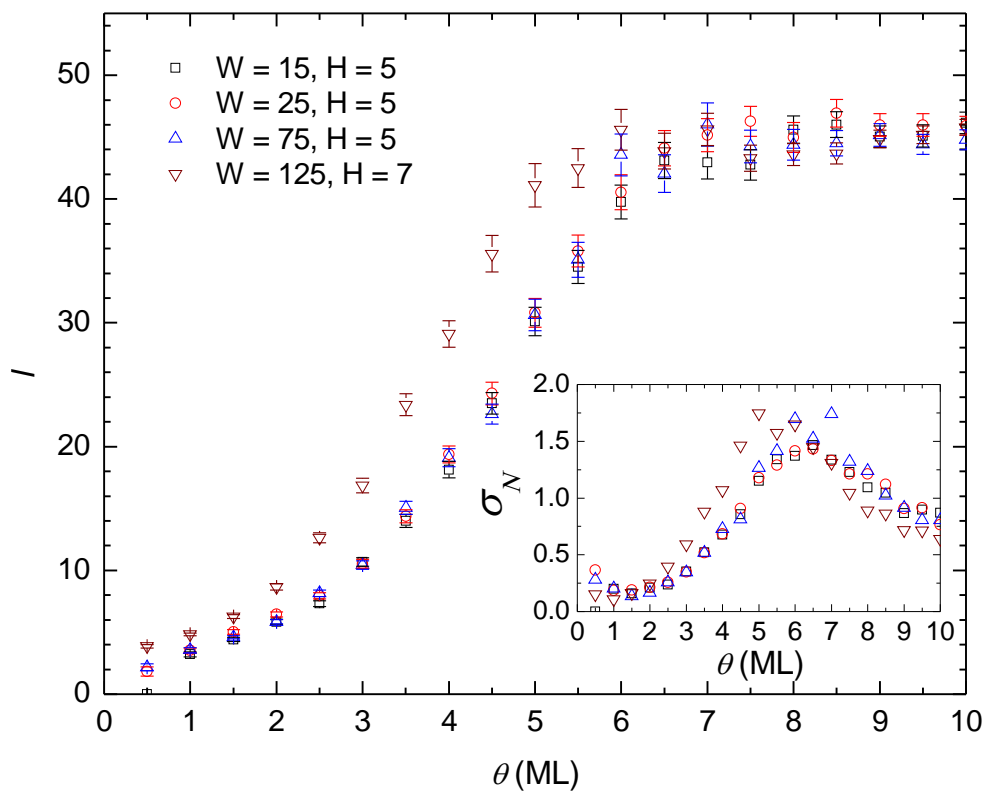
Figure 4.10: The island size (l) as a function of the coverage (θ) from heteroepitaxial growth with various local relaxation areas. Inset: the standard deviation of mean of island size l as a function of coverage θ.
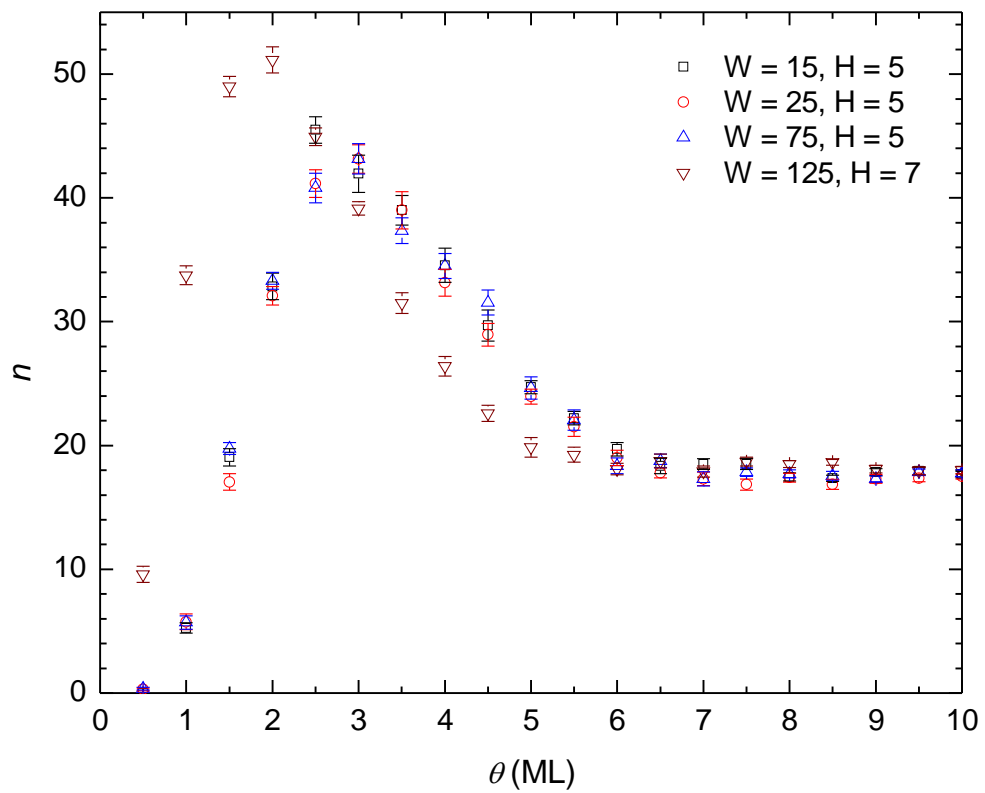
Figure 4.11: The number of islands (n) as a function of the coverage (θ) from heteroepitaxial growth with various local relaxation areas.

of islands are independent of the values of W and H.

4.1.4 Summary

Results in this section are summarized as follows. Firstly, the diffusion of adatoms in the vicinity of kink sites is strongly biased by the strain. Secondly, the island formation is a result of relieving strain in the heteroepitaxial system. Finally, effects of the size of local relaxation on our final results are weak and can be neglected.

4.2 Effects of growth conditions

We have so far shown our numerical results which reveal some aspects of the strain in the heteroepitaxial system. In this section, we will show further that controlling the critical thickness (h_c), island size (l), and number of islands (n) with the growth conditions is possible. The values of the growth conditions are chosen so that we will observe almost the features of films we have studied. Before going into detail, we note that all results of the critical thickness h_c, island size l, and number of islands n are reported at $\theta = 10$ ML. Since the system is in the saturation regime, and the quantities are independent of the local relaxation.

4.2.1 Deposition flux

We begin this part with the effects of the deposition flux F on the heteroepitaxial films. The deposition flux is one of the important factors in the real MBE growth and can be adjusted during the growth process. To produce high quality thin films, the deposition flux is needed to be particularly low (~ 1 ML·s^{-1}) [3] compared with other growth techniques. Growth conditions with the low deposition flux lead to the layer-by-layer growth mode in the homoepitaxial systems or heteroepitaxial systems with small lattice mismatches. In large lattice mismatch systems, the

picture is not true because a flat surface is energetically undesirable. In this work, we not only simulate the heteroepitaxial growth at low deposition fluxes but also at high deposition fluxes. The case in which the deposition rate is too fast compared to the diffusion rate is ignored due to the fact that islands cannot form on the film surface, so the film surface is statistically flat. In this subsection, we report that, at high deposition fluxes, islands (occurred from the pit formation) are essentially a result of limited mobility growth observed in experiments.

We begin with the morphological evolution of heteroepitaxial thin films grown at $T = 600$ K and $\epsilon = 4.0\%$ for various values of the deposition flux (F) shown in Figs. 4.12(a)-(c). For $F = 0.5$ ML·s^{-1} and $F = 1.0$ ML·s^{-1}, the surface morphologies are not much different from each other. Islands seem to grow from normal island formation, i.e. islands grown at the beginning of the growth process capture nearby atoms to increase their sizes. For $F = 2.0$ ML·s^{-1} [Fig. 4.12(a)], however, islands seem to occur from the introducing of pits (or groves). Film surfaces are rather flat in early stages of the growth, then pits develop at $\theta \sim 6$ ML. The pits are randomly formed and become deeper as the coverage increases. As a result, islands bound by the pits are more apparent. The island size (in fact the distance between the centers of the pits) is relatively large. The uniformity of the island size is also reduced since the pits are not uniformly distributed over the film surface. The results show clearly that the heteroepitaxial films possess different surface morphologies depending on whether the film surfaces have pits or islands.

The critical thickness h_c is shown at $T = 650$ K instead of $T = 600$ K because we can measure h_c in a broader range. As we mentioned earlier, with some growth conditions (e.g. $T = 600$ K and high deposition fluxes), the elastic energy per atom ($E/\theta L$) never decreases. Hence the critical thickness is greater than 10 ML, which is of course beyond our scope. Fig. 4.13 shows the critical thickness versus the deposition flux at $T = 650$ K for various values of the lattice mismatch. The results show that larger deposition flux leads to the shift of the critical thickness to higher values. The critical thickness, which increases about

Figure 4.12: The morphological evolution of heteroepitaxial thin films at $T = 600$ K and $\epsilon = 4.0\%$ for (a) $F = 2.0$ ML·s^{-1}, (b) $F = 1.0$ ML·s^{-1}, and (c) $F = 0.5$ ML·s^{-1}. The film thickness increases every $\theta = 1$ ML.

Figure 4.13: The critical thickness (h_c) at $T = 650$ K as a function of the deposition flux (F) for different values of the lattice mismatch (ϵ).

~ 1 ML, is less affected by the deposition flux at large lattice mismatches (e.g. at $\epsilon = 5.0\%$).

Fig. 4.14 and Fig. 4.15 show the relative island size and the number of islands versus the deposition flux at $T = 650$ K for various values of the lattice mismatch. At $\varepsilon = 4.5$ and 5.0%, the island size decreases with increasing F while the number of islands increases accordingly. At $\varepsilon = 4.0\%$ with high deposition rate $F = 5.0$ ML $\cdot$ s^{-1}, l/L increases and becomes less uniform as can be seen from the large deviation of l/L. We have found that if F is increased further to $F = 10.0$ ML $\cdot$ s^{-1}, pit formation occurs.

4.2.2 Lattice mismatch

We next investigate the effects of the lattice mismatch ϵ on the heteroepitaxial films. The growth temperature T and deposition flux F are fixed at $T = 600$ K and $F = 1.0$ ML·s^{-1}. The morphological evolution of film surfaces for various lattice mismatches is shown in Figs. 4.16(a)-(c). The island size is qualitatively smaller as the lattice mismatch increases. In Figs. 4.16(b)-(c), small islands are unstable in the early stages of the growth, and some dissolve due to high stress suppression.

Fig. 4.17 shows the critical thickness h_c as a function of the lattice mismatch ϵ for various values of the deposition flux F. We can see that the critical thickness becomes smaller with the increase in lattice mismatch for all values of F. From the surface morphology, we found that island formation is observed at small h_c. Deposition flux F has a minor effect on critical thickness h_c at lattice mismatch $\epsilon > 4.5\%$, while the effect becomes stronger when $\epsilon \leq 4.5\%$. The critical thickness can be adjusted from $h_c \sim 7$ ML to $h_c \sim 3$ ML depending on the values of ϵ and F.

The solid, dashed, and dotted lines in Fig. 4.17 show the relation $h_c \propto \epsilon^{-a}$, where a being a constant. The values of a are estimated to be $a = 1.84 \pm 0.25$ (solid), 2.26 ± 0.29 (dashed), and 2.80 ± 0.42 (dotted). Our results agree
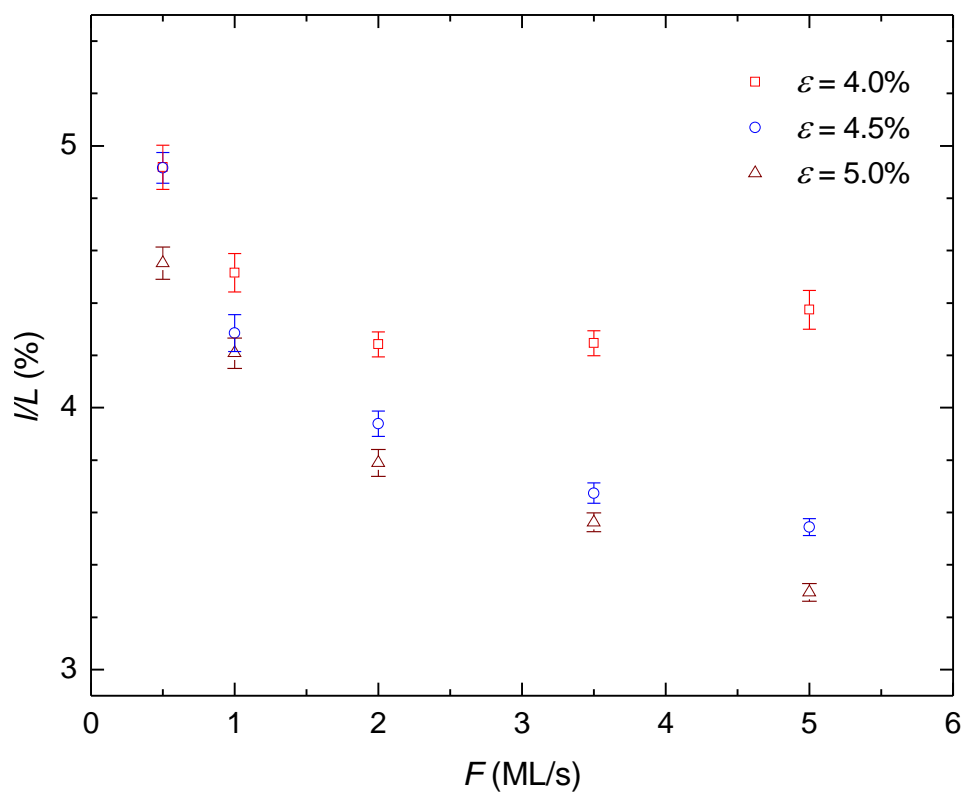
Figure 4.14: The relative island size (l/L) at $T = 650$ K as a function of the deposition flux (F) for different values of the lattice mismatch (ϵ).
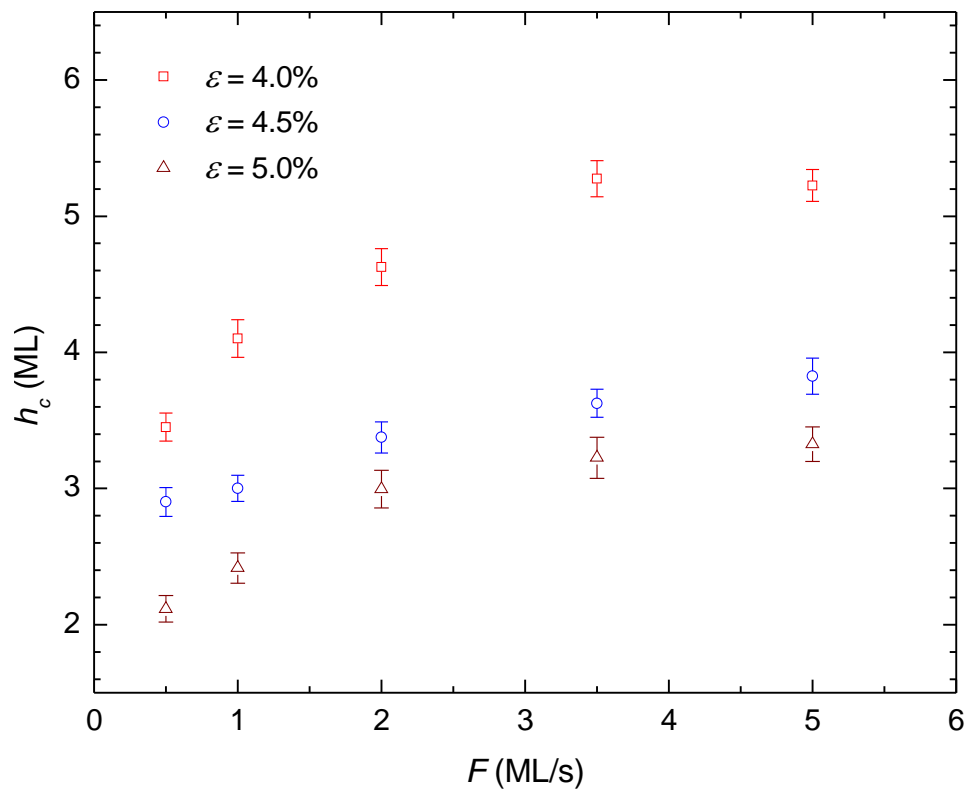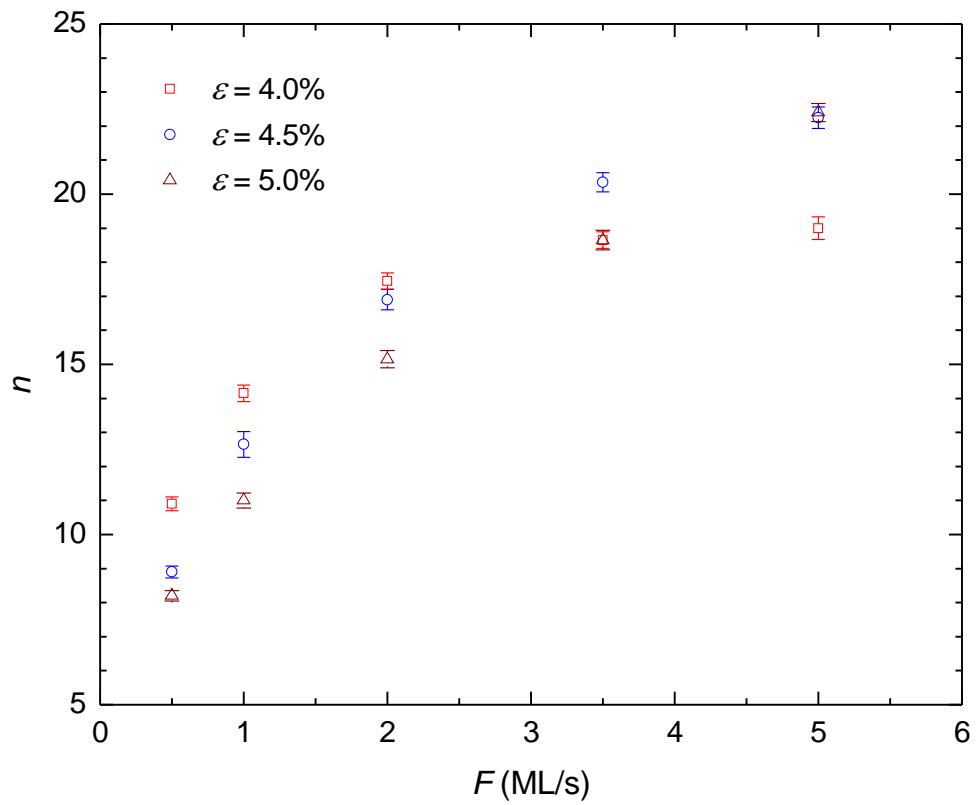
Figure 4.15: The number of islands (n) at $T = 650$ K as a function of the deposition flux (F) for different values of the lattice mismatch (ϵ).

Figure 4.16: The morphological evolution of heteroepitaxial thin films at $T = 600$ K and $F = 1.0$ ML·s^{-1} for (a) $\epsilon = 4.0\%$, (b) $\epsilon = 4.5\%$, and (c) $\epsilon = 5.0\%$. The film thickness increases every $\theta = 1$ ML.

Figure 4.17: The critical thickness (h_c) at $T = 600$ K as a function of the lattice mismatch (ϵ) for different values of the deposition flux (F). Solid, dashed, and dotted lines illustrate a power law relation, $h_c \propto \epsilon^{-a}$, where a being a constant.

well with this equation at deposition fluxes $F = 0.5$ and 1.0 ML $\cdot$ s^{-1}. At $F = 2.0$ ML$\cdot$s^{-1}, however, the relation does not fit well with our results, suggesting that the relation may not be valid for high deposition growth regime. In addition, our results are comparable with an experiment that obtained $a = 1$ [13], simulations with $a = 1.5$ [72, 74], and theoretical prediction of $a = 2$ [37].

The relative island size (l/L) and number of islands (n) are shown in Fig. 4.18 and Fig. 4.19, respectively. It is clear that island size l also decreases with increasing lattice mismatch ϵ, regardless of the deposition flux F. At $F = 2.0$ ML$\cdot$s^{-1}, we found both pit formation (at $\epsilon < 4.125\%$) and island formation (at $\epsilon > 4.125\%$). At $\epsilon < 4.125\%$, in which the pit formation is observed, island size is considerably large and less uniform, as can be seen from the deviation of l/L. As island size l decreases, number of islands n increases and reaches a saturation value of $n \sim 26$ islands at $\epsilon = 5.5\%$. At lower $F = 0.5$ and 1.0 ML $\cdot$ s^{-1}, we observe only island formation in the range of $\epsilon = 4.0 - 5.5\%$. Number of islands n increases slightly with increasing lattice mismatch ϵ from $\epsilon = 4.0\%$ to a particular value of ϵ where n reaches its saturation value. If lattice mismatch ϵ is increased further, both number of islands and island size decrease. At large $\epsilon = 5.5\%$, island density observed here is lower than the island density observed at $F = 2.0$ ML $\cdot$ s^{-1}.

The solid, dashed, and dotted lines in Fig. 4.18 show the relation $l \propto \epsilon^{-b}$, where b being a constant. The values of b are estimated to be $b = 0.45 \pm 0.05$ (solid), 0.94 ± 0.19 (dashed), and 1.26 ± 0.23 ($4.25\% \leq \epsilon \leq 5.5\%$) (dotted). For $F = 2.0$ ML$\cdot$s^{-1} and $\epsilon < 4.25\%$, we observe pits rather than the islands, and the relation may not hold in the pit formation regime. It is clear that the exponent b is affected by the deposition flux. Our values of b are closer to the values of grown films in experiments with $b = 0.9 - 1.1$ [13, 12, 73] than those of annealed films in simulations with $b = 1.8$ [38] and theoretical prediction with $b = 2$ [37].

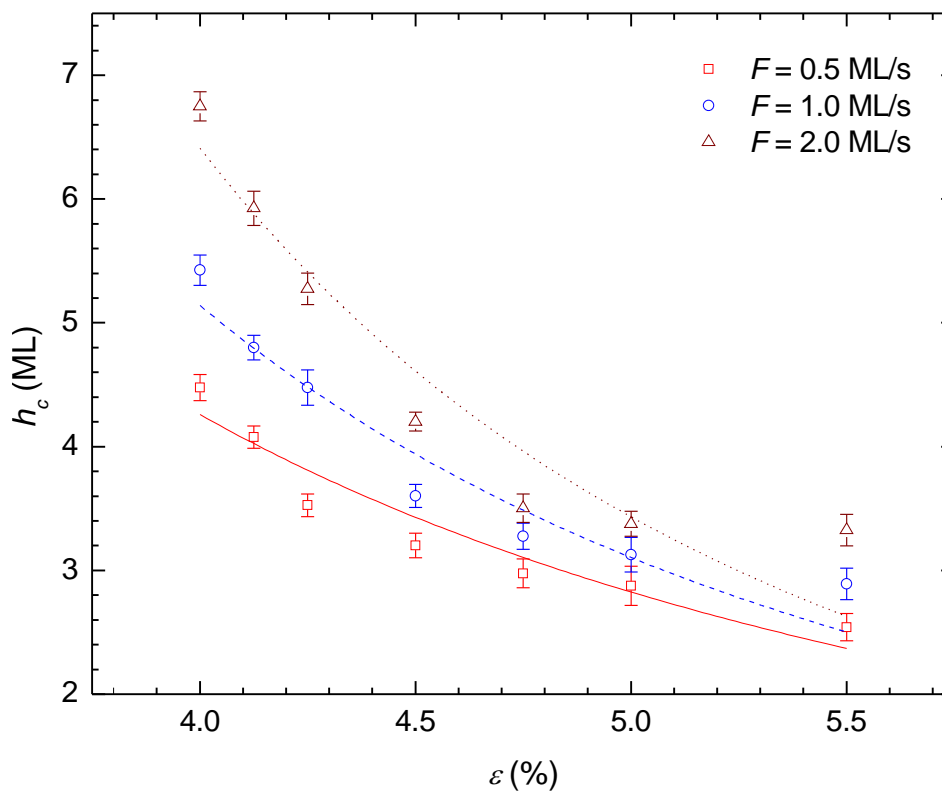Figure 4.18: The relative island size (l/L) at $T = 600$ K as a function of the lattice mismatch (ϵ) for different values of the deposition flux (F). Solid, dashed, and dotted lines illustrate a power law relation, $l \propto \epsilon^{-b}$, where b being a constant.
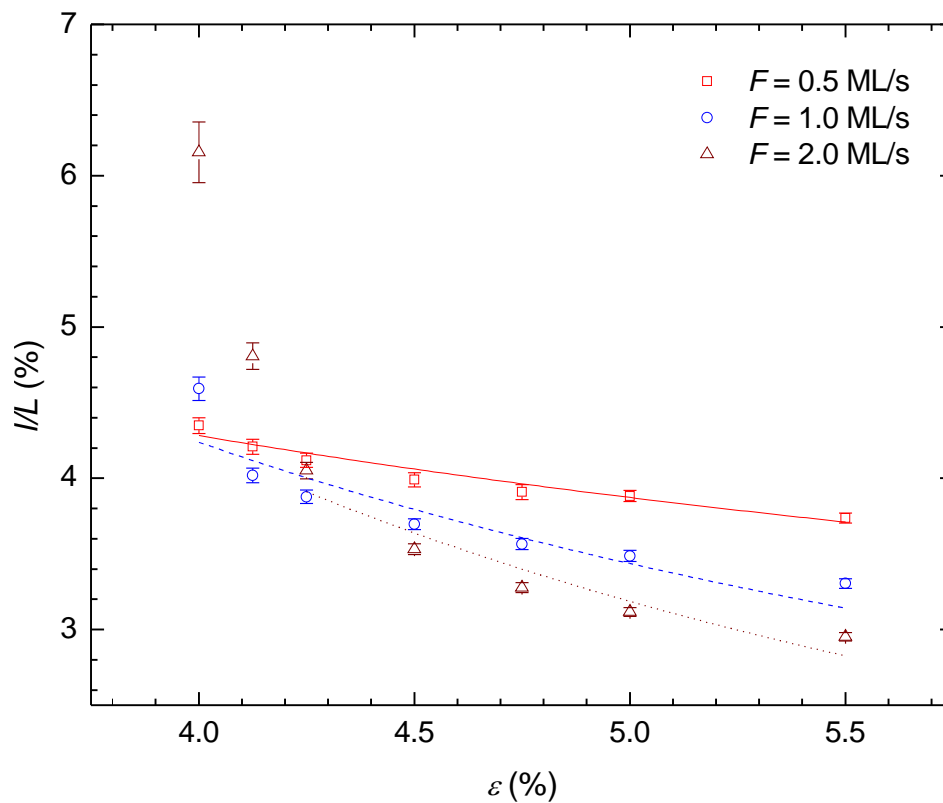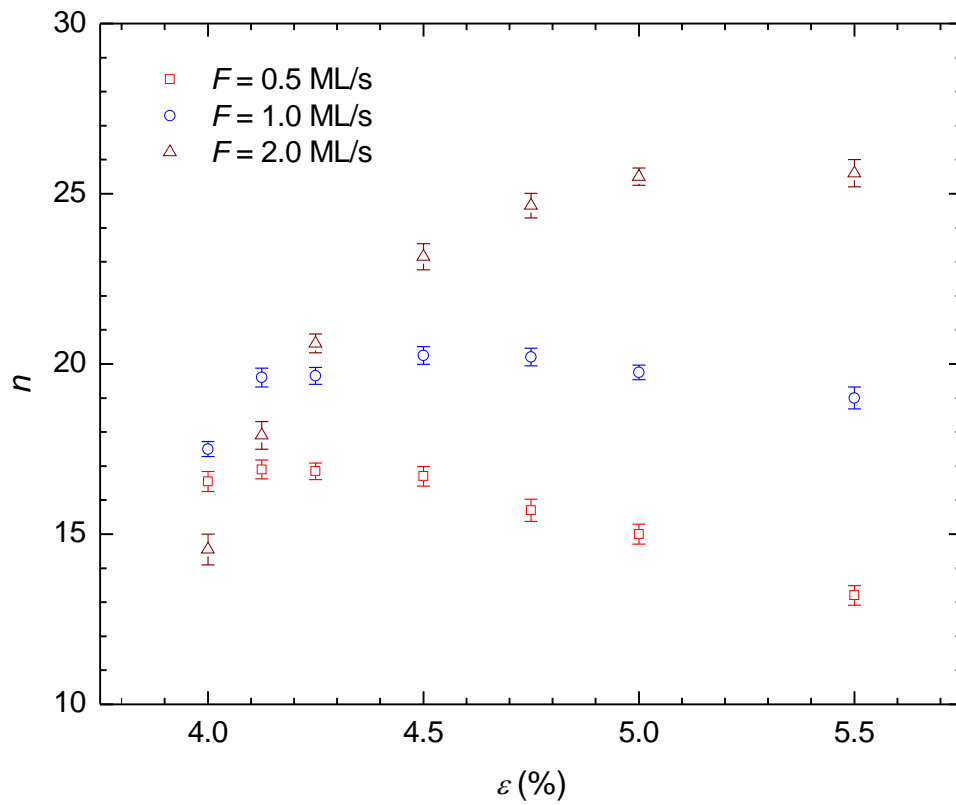
Figure 4.19: The number of islands (n) at $T = 600$ K as a function of the lattice mismatch (ϵ) for different values of the deposition flux (F).

4.2.3 Growth temperature

The growth temperature obviously controls the diffusion rate of adatoms as can be seen from Eq. (3.5). Generally, the diffusion length (an average distance used by adatoms to travel on the film surface) increases exponentially with the temperature [90]. Thus a small variation in the growth temperature can lead to significantly different surface morphologies.

In this subsection, we present the results of the heteroepitaxial films grown at various values of the growth temperature (T). The results show strong dependence of the surface morphology, island size, and number of islands on the temperature. The morphological evolution of heteroepitaxial films grown at $\epsilon = 4.0\%$ and $F = 1.0$ ML·s^{-1} for various values of the temperatures T is shown in Figs. 4.20(a)-(c). The surface morphologies are obviously different from each other. At $T = 550$ K [Fig. 4.20(a)], the layer-by-layer growth is observed in the early stages of growth, small pits then develop nearly the end of the growth. At a higher temperature ($T = 650$ K) in Fig. 4.20(c), islands occur from the island formation. In addition, some small islands disappear at the end of growth (Ostwald ripening) [39].

Fig. 4.21 shows the critical thickness as a function of the growth temperature for various values of the deposition flux. Again we show the critical thickness of the heteroepitaxial thin films at $\epsilon = 5.0\%$ because, at low temperatures, the critical thickness cannot be observed. We can see that growth temperature T also influences critical thickness h_c as well as deposition flux F—increasing T and decreasing F lead to similar kinetically effects. Both cause h_c to become smaller as can be seen in Fig. 4.13 and Fig. 4.21. The critical thickness can be adjusted from $h_c \sim 5$ ML to $h_c \sim 2$ ML by varying the deposition flux and temperature.

The relative island size and number of islands versus the temperature at $\epsilon = 5.0\%$ for various values of the deposition flux are shown in Fig. 4.22 and Fig. 4.23, respectively. At $F = 0.5$ and 1.0 ML $\cdot$ s^{-1}, island size l increases with growth temperature T and decreases with increasing deposition flux F. Number of islands n drops according to the increasing of island size l. At higher $F =$

Figure 4.20: The morphological evolution of heteroepitaxial thin films at $F = 1.0$ ML·s^{-1} and $\epsilon = 4.0\%$ for (a) $T = 550$ K, (b) $T = 600$ K, and (c) $T = 650$ K. The film thickness increases every $\theta = 1$ ML.

Figure 4.21: The critical thickness (h_c) at $\epsilon = 5.0\%$ as a function of the growth temperature (T) for different values of the deposition flux (F).
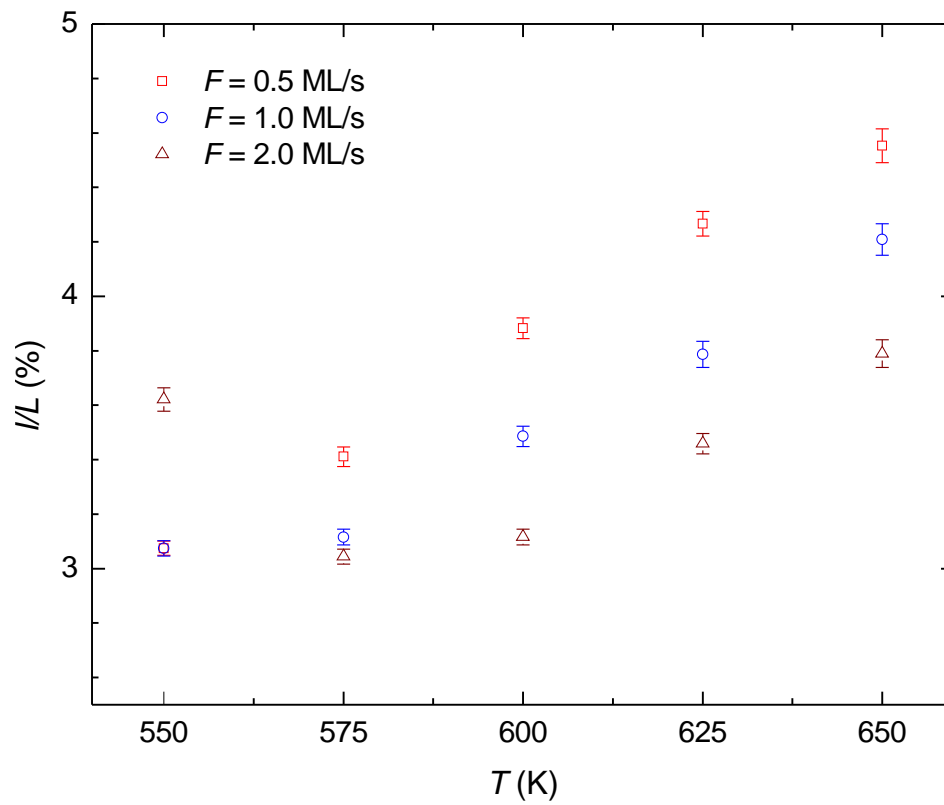
Figure 4.22: The relative island size (l/L) at $\epsilon = 5.0\%$ as a function of the growth temperature (T) for different values of the deposition flux (F).
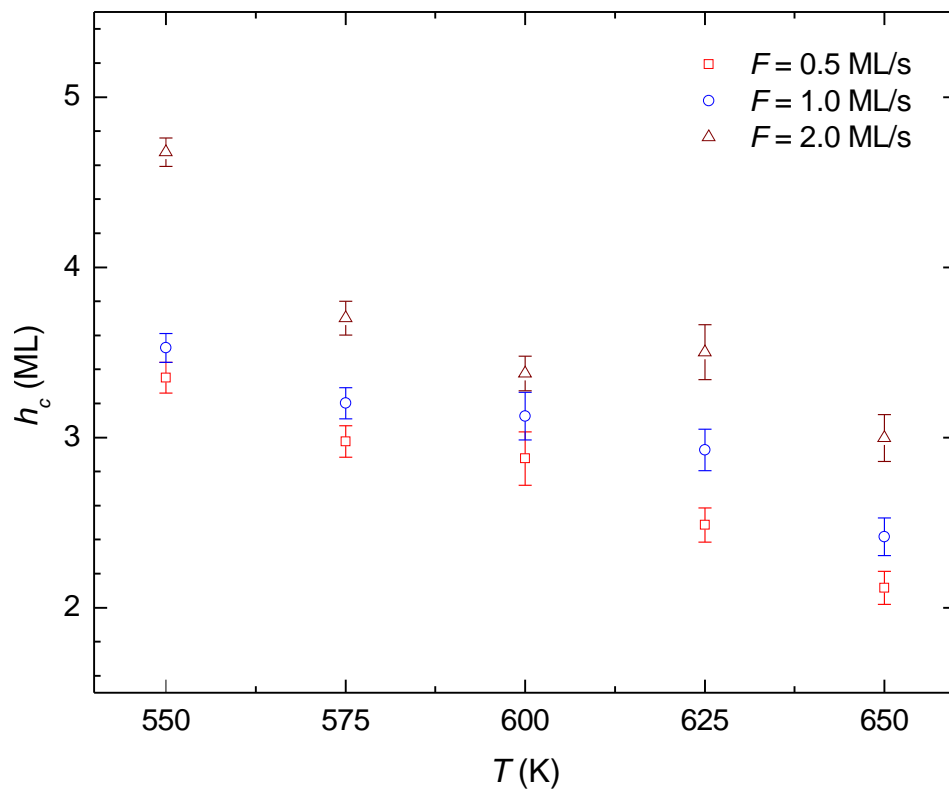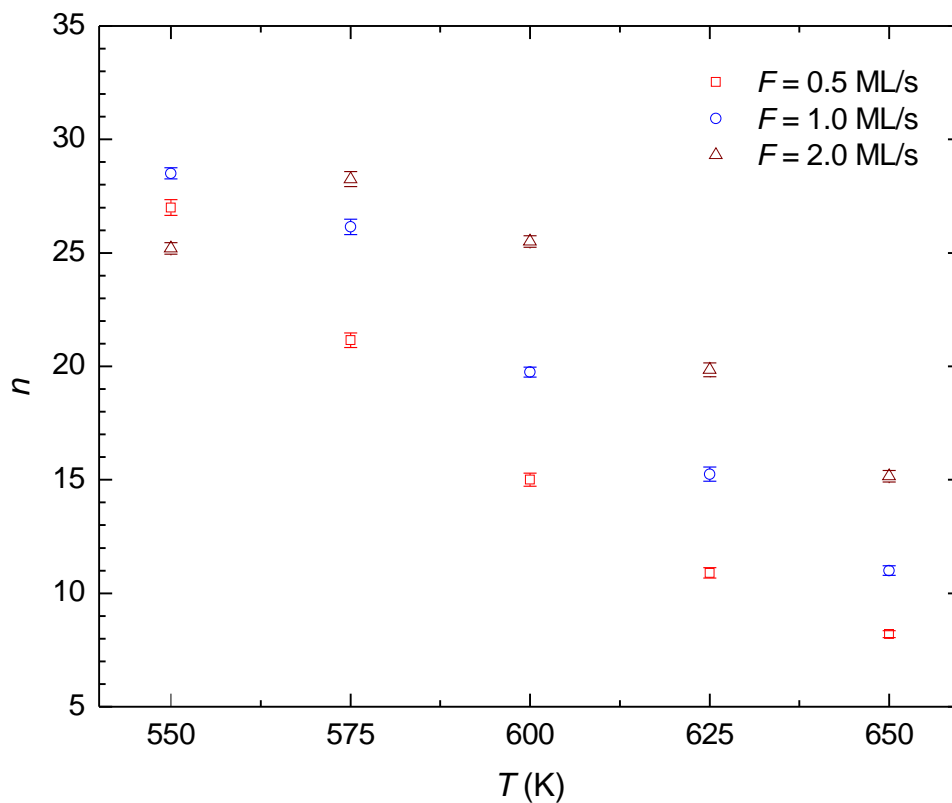
Figure 4.23: The number of islands (l/L) at $\epsilon = 5.0\%$ as a function of the growth temperature (T) for different values of the deposition flux (F).

$2.0 \, \mathrm{ML \cdot s^{-1}}$, however, we observe pits at $T = 550$ K and islands at higher T. Our result suggests that, as well as by varying F, pits and islands can be found by varying T. These results agree with previous work [19, 18]. In addition, island size l is less uniform when growth temperature T increases to $T = 650$ K which can be seen from the deviation of l/L.

Here, we discuss our numerical results of this section. According to the pit and island formation mechanisms and available data points for various growth conditions, we plot qualitatively a diagram in Fig. 4.24. All points (●) below the surface denote pits and all points (●) above the surface denote islands. The surface cutting is draw by the points (●) which denotes the transition regime. We note that although the formation of pits and islands is not obvious at the interface and in the area nearby, all data points that are far from this area i.e. deeply below the surface and highly above the surface show clearly the pit and island formation respectively. For example, at $T = 600$ K and $F = 0.5 \, \mathrm{ML \cdot s^{-1}}$ we observe only islands at $\epsilon > 4.0\%$.

We have found that the trend of critical thickness h_c is related to pit and island formation regions. For example in Fig. 4.13 when F increases, h_c increases accordingly and the system moves deeply in the pit regime according to the diagram in Fig. 4.24. This result is also consistent with the experimental result shown in Fig. 4.25 at $T = 550$ °C. The morphological evolution changes from the formation of islands at deposition rate $R_{\mathrm{dep}} = 0.015 \, \mathrm{nm \cdot s^{-1}}$ to the formation of pits at $R_{\mathrm{dep}} = 0.09 \, \mathrm{nm \cdot s^{-1}}$. In this region deposited atoms interrupt adatoms from hopping to energetically more preferable sites (at upper layers or on top of existing islands). Adatoms are buried before they reach existing islands. As a result, it takes longer time for islands to form, and the critical thickness is then larger.

Similarly in Fig. 4.21 when T increases, h_c decreases accordingly and the system moves deeply in the island region according to the diagram in Fig. 4.24. This result agrees with the experimental result shown in Fig. 4.25 at $R_{\mathrm{dep}} = 0.09 \, \mathrm{nm \cdot s^{-1}}$. The morphological evolution changes from the formation of pits at

Figure 4.24: F-ϵ-T diagram. Points (●) below the surface denote pits and points (●) above the surface denote islands. The surface cutting the points (●) and area nearby the surface denote the transition regime.
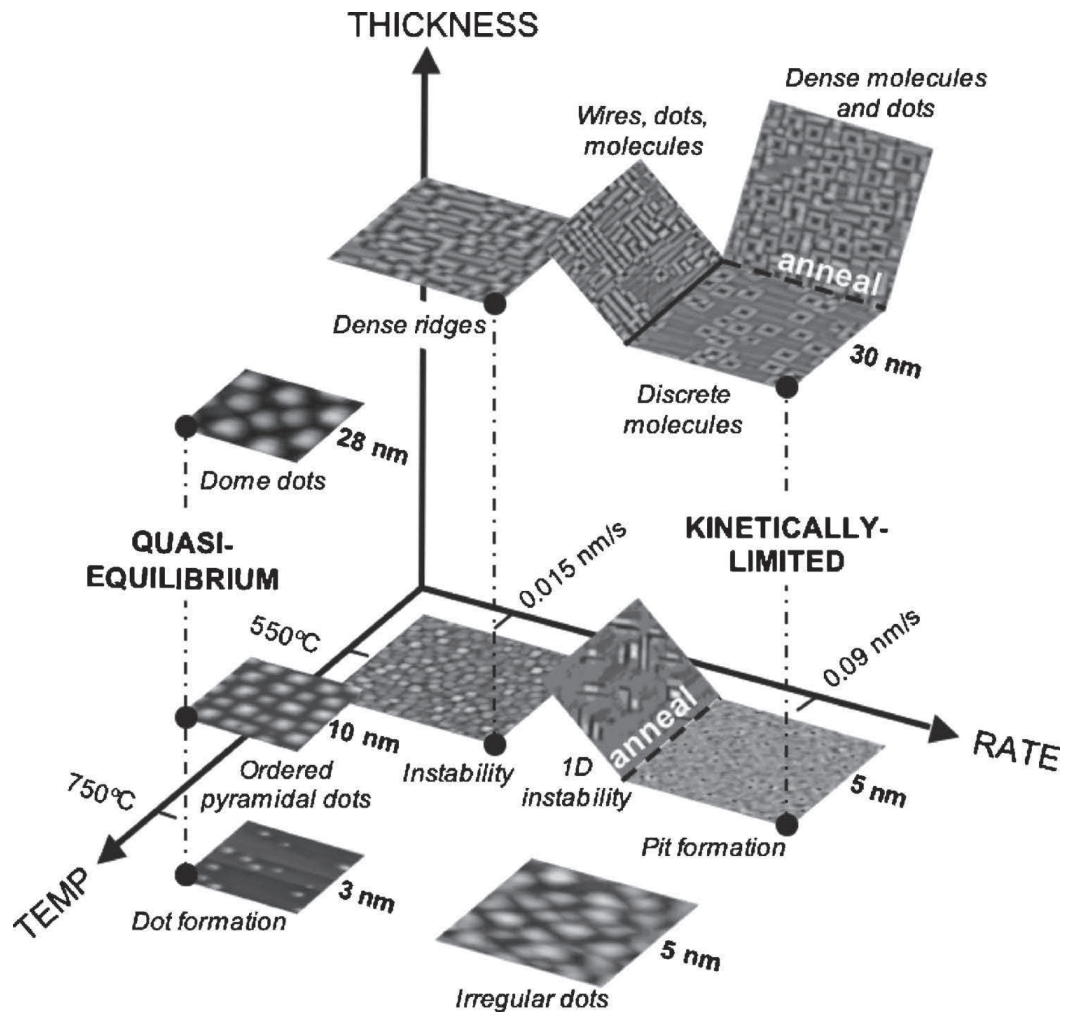
Figure 4.25: Morphological evolution of GeSi/Si (001) thin films during MBE growth with $\epsilon \approx 1.2\%$ [19].

$T = 550$ °C to the formation of islands at $T = 750$ °C. In this region the growth temperature enhances the adatom diffusion, so islands form early. Hence h_c is low.

In general, the formation of pits observed in our simulations is consistent with that in limited mobility growth regime at high deposition flux and low growth temperature [19, 38]. This regime is at the far back corner of the diagram (point $T = 550$ K, $F = 10$ ML $\cdot$ s^{-1} and $\epsilon = 3.5\%$) which is deeply below the cutting surface. In limited mobility growth, the formation of pits is more preferable for strain relief [19, 38, 39]. When surface diffusion process becomes significant, at high growth temperature and low deposition flux, island formation is preferable [8, 38]. This regime is at the near front corner of the diagram (point $T = 650$ K, $F = 1.0$ ML $\cdot$ s^{-1} and $\epsilon = 5.5\%$) which is high above the cutting surface. The transition from island to pit formation indicates the onset of a limited mobility growth regime.

Moreover, the trend of our results quite agrees with experimental results [18] and the picture of morphological evolution shown in Fig. 4.25.

4.2.4 Summary

Results in this section, Effects of growth conditions, are listed in Table 4.1 and summarized as follows. The pit formation, resulting from the limited mobility growth, is observed at low lattice mismatches, high deposition fluxes, and/or

Properties	$\epsilon \uparrow$ (at $T = 600$ K)	$F \uparrow$ (at $T = 650$ K)	$T \uparrow$ (at $\epsilon = 5.0\%$)
h_c	$\downarrow$ ($h_c \propto \epsilon^{-a}$)	$\uparrow$	$\downarrow$
l	$\downarrow$ ($l \propto \epsilon^{-b}$)	$\downarrow$	$\uparrow$
n	$\uparrow$ (at high F) $\downarrow$ (at low F)	$\uparrow$	$\downarrow$

Table 4.1: Relevant properties of heteroepitaxial thin films in the island formation regime. For example, h_c decreases when ϵ increases at $T = 600$ K.

low temperatures. And the heteroepitaxial films possess different morphologies depending on whether the film surfaces have pits (groves) or islands.

CHAPTER V

An Application of Roughness Exponent Method in a Frustrated Spin System

In this chapter, we discuss the possibility of using the global roughness (W), also known as the interface width, and its exponents of a modified SOS growth model to determine a critical temperature and critical exponent ν of a frustrated spin model. The exponents of the SOS growth model: growth exponent β, roughness exponent α, and dynamical exponent z, are calculated by means of the scaling concept and data collapse. The global roughness W and roughness exponent α are sensitive enough to detect a critical temperature of the spin model. Moreover, the exponents of both models are also connected with some relation, which can be used to verify the universality class of the spin model.

We arrange this chapter as follows: firstly, we provide a brief introduction to the previous studies using the SOS growth method to determine behavior of various spin models. We then introduce a frustrated spin model, to which the SOS growth method is adopted. In the next section, we present the frustrated spin model and method to determine the critical temperature and exponents. We discuss our numerical results in section 5.3. In this section, we compare our results with those results obtained from conventional spin methods. Finally, we summarize the results of this chapter in section 5.4.

5.1 Introduction

In the past decades, kinetic roughening of film surfaces generated by growth models has been one of the most attractive subjects studied in computational, theoretical, and also experimental statistical physics [2, 97, 98, 99, 100, 101, 102]. Its behavior seems to occur in a wide range of physical systems, which reflects its universality. In order to study physical properties of the systems, some parameters must be introduced. The standard tools used in growth models are the roughness (W) and its exponents: growth exponent (β), roughness exponent (α) and dynamical exponent (z) [2, 84]. Once the exponents are determined, the universality of the systems is classified.

It had been shown [103, 104, 105] that W, β_w[1] and α obtained from mapping spin configurations to rough surfaces of a solid-on-solid (SOS) growth model can be used to detect transition points of spin models. In addition, the exponents can also be used to verify the validity of its universality classes by considering scaling relations between growth and spin models. This approach was introduced by de Sales *et al* [106, 107]. They considered cellular automata (CA) and then mapped the CA configurations to surfaces of a SOS model. By using the roughness exponent method, the CA universality classes can be classified more precisely. Later, Atman *et al.* [108, 109] showed that β_w can be used not only to detect the Domany–Kinzel cellular automaton (DKCA) phases, but also to test scaling relations of critical exponents between growth and DKCA models. In spin models, Redinz and Martins [103] studied the q-state (with $q =2$, 3, and 7) Potts and $p =10$ clock models. The results showed that α and ϵ^* (characteristic length) sharply change near critical points. For the clock model, the intermediate phase or spin-wave phase was also found [104, 105]. Furthermore, Brito *et al.* [110] studied the Ising chain with long-range interactions and found the value of α to peak near critical points, resulting in super-roughening. The detailed study was extended to q-state Potts, spin-1 Blume-Capel (BC) models, and two-dimensional XY models [104, 105].

---

[1]The subscript w denotes a quantity that is of the SOS growth model.

In studies of spin systems, frustrated spin models have received much attention. It describes an array of Josephson junctions under an external field [111]. Some of the interesting models investigated via the simulation methods are the fully frustrated XY model [112, 113, 114, 115], the frustrated antiferromagnetic XY (FAXY) model [116, 117, 118] and the frustrated antiferromagnetic six-state clock model [119, 120]. These models have a rotational $U(1)$ symmetry and an additional reflection Z_2 symmetry or chiral symmetry that can be broken at critical temperatures through the Kosterlitz–Thouless and an Ising-like transition temperatures, T_{KT} and T_I, respectively. Since systems with the $U(1)$ symmetry are expected to belong to the KT universality class [83, 94], therefore the Z_2 symmetry has been the subject of interest in these models. It has been found that the Z_2 symmetry (with the critical exponent, $\nu < 1$) may not belong to the Ising universality class [113, 114, 116, 117, 118, 120]. Other [115, 119] argue that it is the finite size effect and $\nu = 1$ in the limit of $L \to \infty$, so the results are still controversial.

We, therefore, investigate the FAXY model on a two-dimensional triangular lattice. The chiral configurations are mapped (like a walk process) to rough surfaces of a SOS growth model, for which the roughness exponent method will be used. As discussed earlier, the aims of this study are to study the chiral symmetry breaking of FAXY model and to provide simulation details of this model, since frustrated models have not been much studied using this method.

5.2   Models and Methods

The Hamiltonian of the lattice spin model is given by

$$H = -J \sum_{\langle ij \rangle} \mathbf{S_i} \cdot \mathbf{S_j} = -J \sum_{\langle ij \rangle} \cos(\theta_i - \theta_j), \tag{5.1}$$

where $\langle ij \rangle$ denotes a sum over all neighbor spin pairs, J is a coupling constant, $\mathbf{S_i}$ is a spin variable with $|\mathbf{S_i}| = 1$, and θ_i is an angle of $\mathbf{S_i}$ with respected to an arbitrary direction. In the FAXY model, the chirality at each elementary triangle

is defined as

$$\kappa_{\triangle_i, \triangledown_i} = \frac{2}{3\sqrt{3}}[\sin(\theta_m - \theta_l) + \sin(\theta_n - \theta_m) + \sin(\theta_l - \theta_n)], \tag{5.2}$$

where $\triangle_i$ and $\triangledown_i$ denote up- and down-triangle i, respectively (see Fig. 5.1). The staggered chirality which plays a role of spin-like variable of the Z_2 symmetry is given by

$$\kappa_i = \frac{1}{2}(\kappa_{\triangle_i} - \kappa_{\triangledown_i}). \tag{5.3}$$

According to the method [106, 107], a positive-state of κ_i at site i and at time t' is equivalent to deposition of an atom on the film surface while a negative-state leads to an evaporation of an atom. Local hight at site i and at time t, then, is the accumulation of atoms on the surface from t' to t as

$$h_i(t) = \sum_{t'=0}^{t} \kappa_i(t'). \tag{5.4}$$

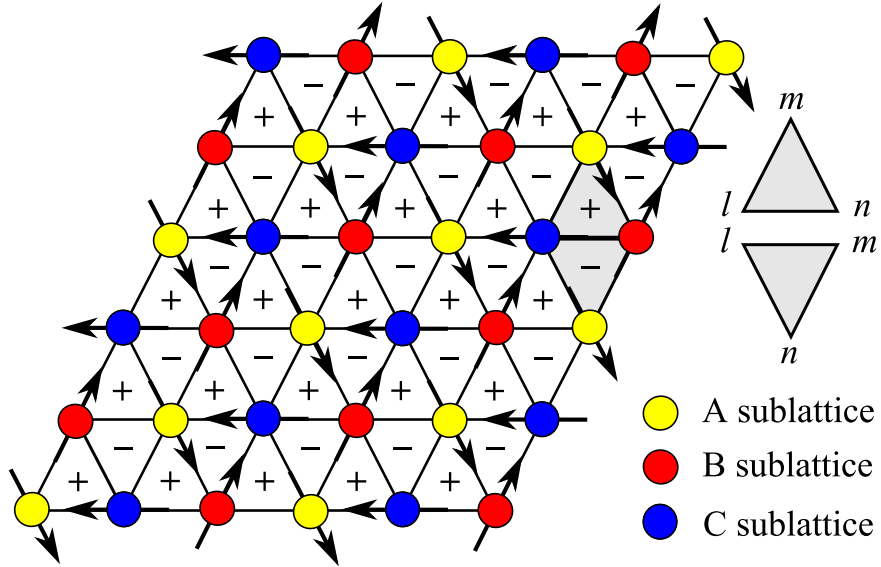The global roughness, also known as the interface width, defined from fluctuation

Figure 5.1: The FAXY model with $N = 6 \times 6$ sites. The circles refer to spins in A, B and C sublattices, the $\pm$ signs denote the chirality at each elementary triangle, and the shaded triangles refer to up- and down-triangle i, respectively.

relation of h_i is given by [2]

$$W(L,t) = \sqrt{\langle (h_i(t) - \langle h(t) \rangle_L)^2 \rangle_L}, \tag{5.5}$$

where $\langle \ldots \rangle_L$ denotes an average overall substrate of size L. At early time, W increases with increasing t as $W(t) \sim t^{\beta_w}$ when β_w is the growth exponent, and saturates after a crossover time $t_\times$. When $t > t_\times$, W is independent of t, but W depends on the substrate size L as $W(L) \sim L^\alpha$, where α is the roughness exponent. The scaling form of W can be written as [121]

$$W(L,t) \sim L^\alpha f\left(\frac{t}{L^{z_w}}\right), \tag{5.6}$$

where $f(u)$ is a scaling function, $f(u) \sim u^{\beta_w}$ for $t \ll t_\times$ and $f(u) = $ const. for $t \gg t_\times$. The crossover time grows as a function of L, $t_\times \sim L^{z_w}$, so $z_w = \alpha/\beta_w$. For a random deposition (RD) process, W increases indefinitely with time as $W \sim t^{\beta_w}$ with $\beta_w = 1/2$ because the correlation length is zero at all time. For correlated systems, the correlation length increases with time and saturates at $t_\times$, so β_w should deviate from $1/2$ at $t < t_\times$. In the case of a persistent correlation process, $\beta_w > 1/2$ while in the case of the anticorrelation function process, $\beta_w < 1/2$. It has been shown that the Monte Carlo simulations add an intrinsic noise to the SOS model [104, 105]. At high temperatures, spins are uncorrelated, then W increases definitely with t as a RD process. This noise still exists even when the system is in a critical state. The Family-Vicsek scaling in Eq. (5.6), therefore, does not hold in this model because $\alpha \to \infty$. In order to remove the effect, the factor $t^{-1/2}$ is introduced to W [104, 105]. The noise-reduced roughness is then given by

$$W^*(L,t) = t^{-1/2}W(L,t). \tag{5.7}$$

The new relations become $\beta_w^* = \beta_w - 0.5$, $z_w^* = z_w$, and $\alpha^* = z_w(\beta_w - 0.5)$.

In simulations, we use linear size $N = L \times L$ with $L = 24$ to 120 sites, and we average all results over 25 to 200 independent runs depending on L. The maximum simulation time is up to 5×10^5 Monte Carlo steps (MCS). The Monte Carlo algorithm, together with Metropolis method, are used to update spin states [83, 91, 94]. The system is initially set in high temperature states. The temperature is then

decreased and the systems are allowed to relax to equilibrium states. Likewise, h_i is set to be zero at initial states (flat substrates), although W only depends on the fluctuation of the surfaces.

5.3   Results and discussions

In our work, temperature is measured via the dimensionless quantity $T \equiv k_B \tau / |J|$, where k_B is the Boltzmann constant, τ is the temperature and J is the coupling constant in Eq. (5.1). Fig. 5.2 shows the film surfaces taken at $t \gg t_\times$ and different temperatures. For $T > T_I$ [Fig. 5.2(a)] and $T < T_I$ [Fig. 5.2(c)], the film surfaces are rough in a short scale while the film surface is rough in a large scale at $T \simeq T_I$ [Fig. 5.2(b)]. This is due to the fact that fluctuations are maximum at the transition point.

In order to quantify the film roughness, the noise-reduced roughness, W^*, is studied. In Fig. 5.3, W^* is plotted versus t at different T for $L = 120$ sites. In the early time, W^* increases with increasing t as $W^*(t) \sim t^{\beta_w^*}$ with $\beta_w^* = 0.513, 0.423$ and 0.256 for $T = 0.540, 0.515$ and 0.500, respectively. We can see that W^*_{sat} is maximum at $T = 0.515$ which is near T_I.

In Fig. 5.4, we consider W^* as a function of t at $T = 0.520$ for $L = 24, 48, 72, 96$ and 120 sites. It can be seen that W^* increases with t, and saturates after $t_\times$. The inset shows that W^*_{sat} grows as $W^*_{sat}(L) \sim L^{\alpha^*}$. The solid line shows the power law of W^*_{sat} with $\alpha^* = 1.03$ when $T = 0.520$.

The process is then repeated for different values of T. In Fig. 5.5, W^* at the saturated time (W^*_{sat}) is plotted versus temperature T. Starting from the high temperature phase $T > T_I(L)$, W^*_{sat} increases as the temperature is decreased. The temperature at which W^*_{sat} reaches the maximum value is called $T_I(L)$ where $T_I(L)$ represents the critical temperature of a system with finite size L. When the temperature is decreased further to the $T < T_I(L)$ range, W^*_{sat} decreases with T. In addition, Fig. 5.5 shows that the substrate size dependence of W^*_{sat} is particularly strong near the transition point, in which all atoms are correlated. It
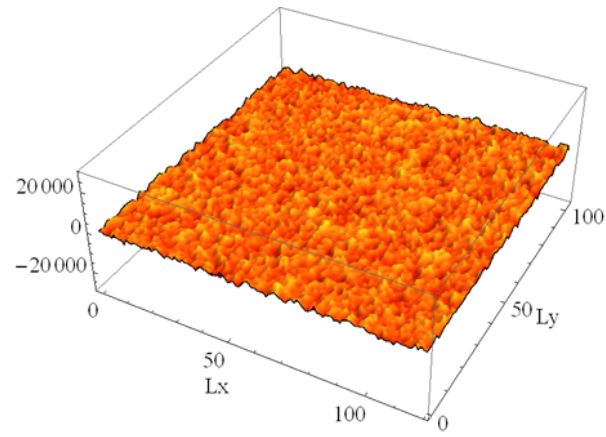
(a) $T > T_I$
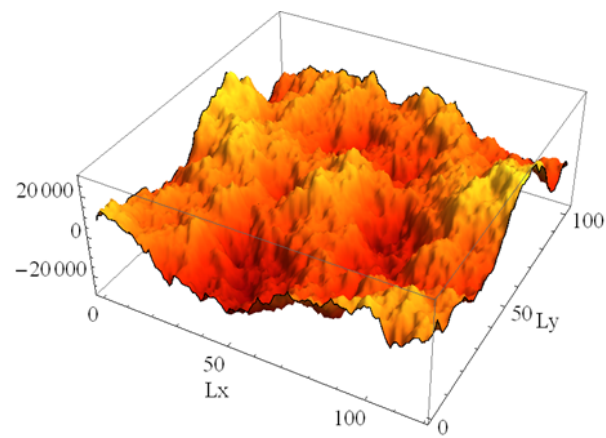
(b) $T \simeq T_I$
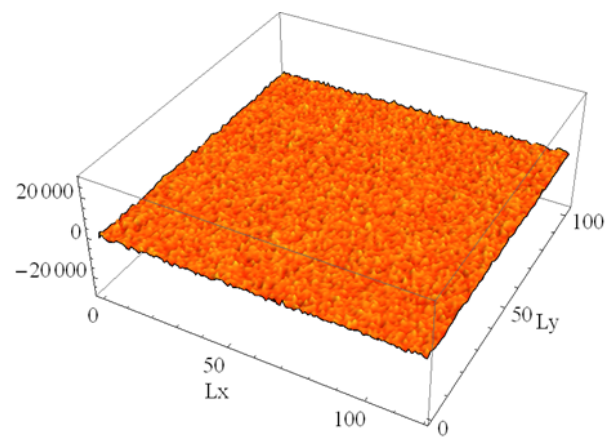
(c) $T < T_I$

Figure 5.2: The film surfaces of a system with $L = 120$ sites at a saturated time; (a) $T > T_I$, (b) $T \simeq T_I$, and (c) $T < T_I$.
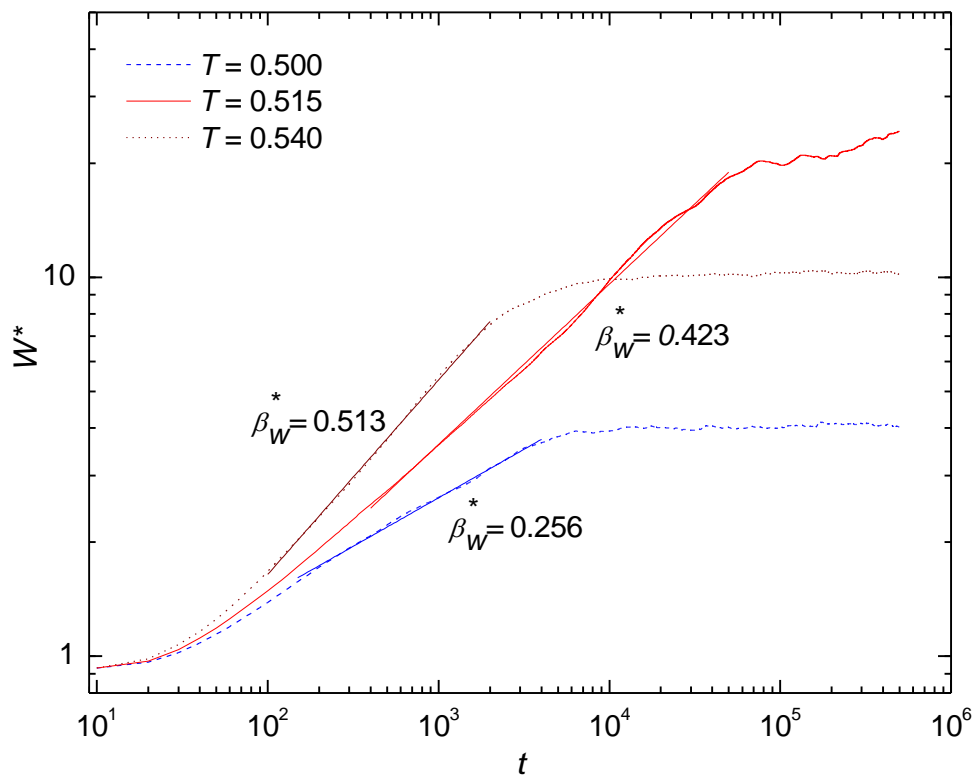
Figure 5.3: W^* as a function of t for $L = 120$ sites at different T. The power law of W^* in the early t is indicated by β_w^*.
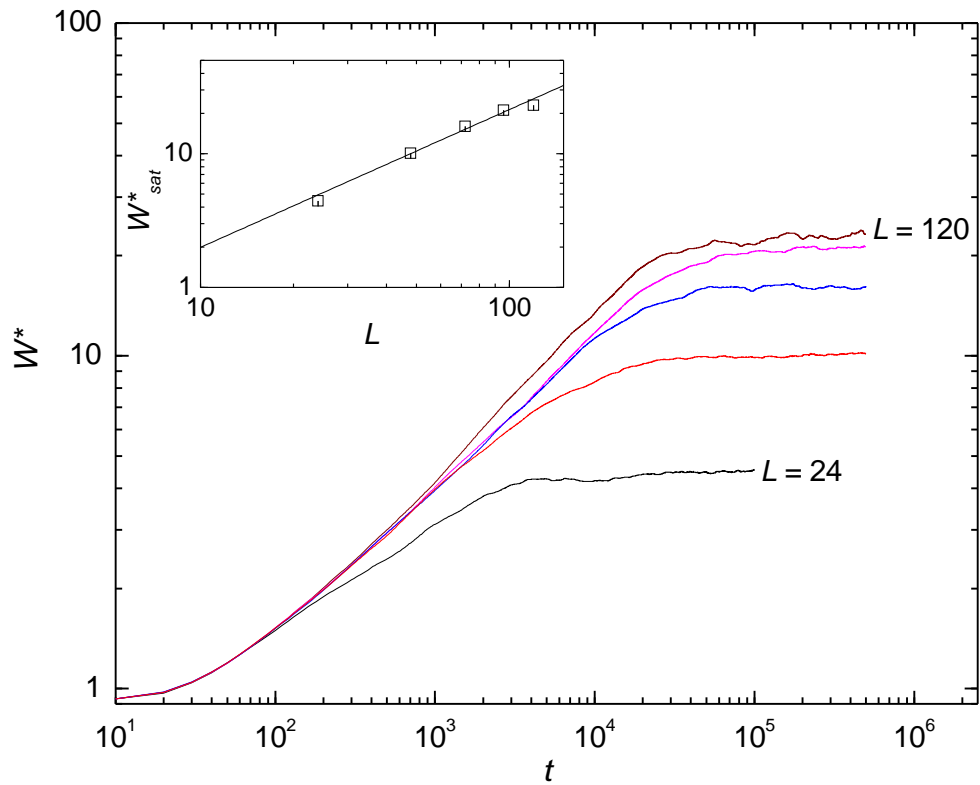
Figure 5.4: The evolution of W^* as a function of t at $T = 0.520$ for $L = 24$, 48, 72, 96 and 120 sites (from the bottom to the top). The solid line in the inset shows the power law of W^*_{sat} with $\alpha^* = 1.03$.
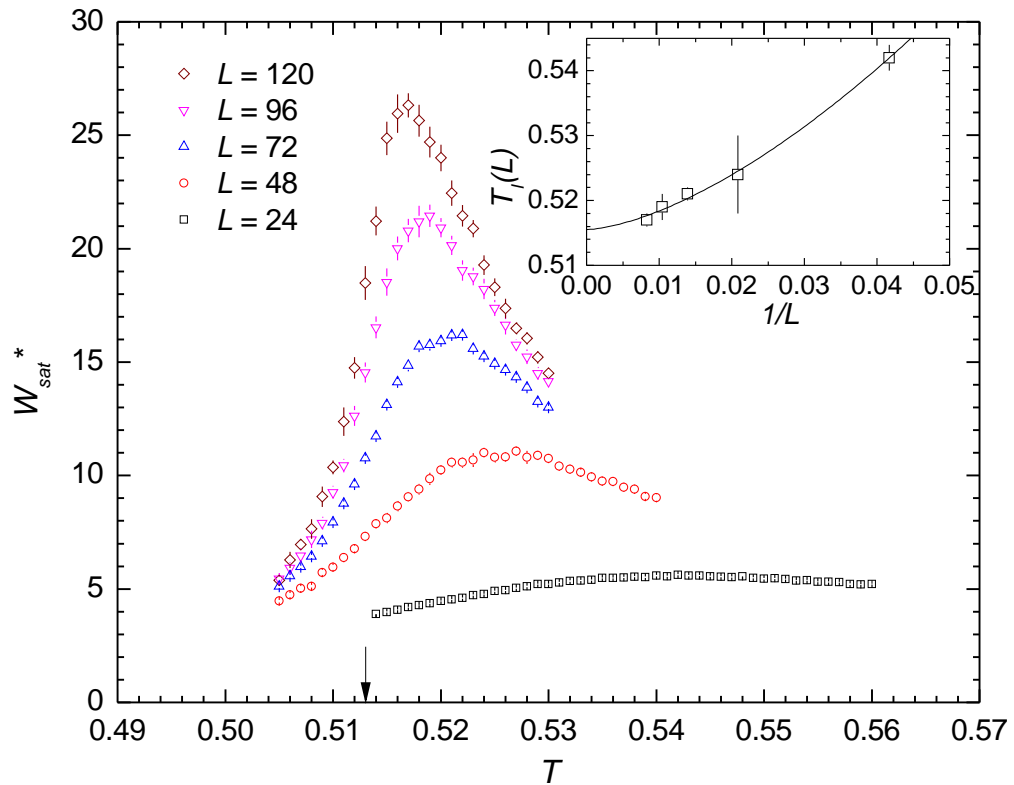
Figure 5.5: The temperature dependent of W_{sat}^* at $t \gg t_\times$ with different L. The arrow marks $T_I \simeq 0.513$ and the inset shows the best fit of $T_I(L)$ as a function of $1/L$.

is seen that when L is increased, the peak becomes narrow and shifts toward the low temperature region. The value of $T_I(L)$ also shows strong dependence on L. To obtain the "real" critical temperature, we need to find T_I in the thermodynamic limit [105], $T_I = T_I(L \to \infty)$. To this end, $T_I(L)$ is plotted versus $1/L$ as shown in the inset. The graph is then fitted with an equation $T_I(L) = T_I + C(1/L)^\lambda$ where C and λ are nonuniversal constants. The result yields $T_I = 0.515 \pm 0.002$, $C = 3.694$ and $\lambda = 1.554$, which is the same as those results (marked by the arrow) obtained from conventional statistical methods. The results are $T_I = 0.513(1)$ using $L = 12$ to 102 from Ref. [117] and $T_I = 0.512(1)$ using $L = 500$ to 2000 from Ref. [118].

The value of α^*, obtained via the W_{sat}^* vs L plot as shown in the inset of Fig. 5.4, can also be used to identify T_I. Fig. 5.6 shows a plot of α^* as a function of T. One can see that α^* increases with decreasing temperature to the maximum value at $T \simeq T_I$ marked by the arrow, and decreases to zero after $T < T_I$. This result shows that W_{sat}^* is independent of L ($\alpha^* = 0$) for $T < T_I$.

It is known that [83, 91, 94, 122] in spin systems, the correlation length (ξ) is finite when the temperature is far from the critical temperature. Spins are correlated in a small regime only and the spin fluctuations are low. However, when the temperature reaches the critical temperature, ξ diverges to infinity[2] [83]. The spins are entirely correlated and the spin fluctuations are at the maximum value. When spin configurations are mapped to film surfaces of SOS growth model, the roughness of the surfaces represents the spin fluctuations. Fig. 5.2(a) and Fig. 5.2(c) show the film surfaces when ξ is small, while Fig. 5.2(b) shows the film surface when $\xi \sim L$. The maximum value of ξ at $T = T_I(L)$ is clearly seen in Fig. 5.5.

In order to determine the exponent ν of the correlation length ($\xi \sim t_I^{-\nu}$) in the spin model, W_{sat}^* is written in a scaling form [83, 122], $W_{sat}^* = L^{\alpha^*} f(t_I L^{1/\nu})$, where $t_I = |(T - T_I)/T_I|$ is a reduced temperature. Fig. 5.7 shows the data collapse of W_{sat}^*/L^{α^*} as a function of $t_I L^{1/\nu}$. The result yields $\alpha^* = 0.963$, $\nu = 0.81$,

---

[2]Note that $\xi \sim L$ for a finite system size.
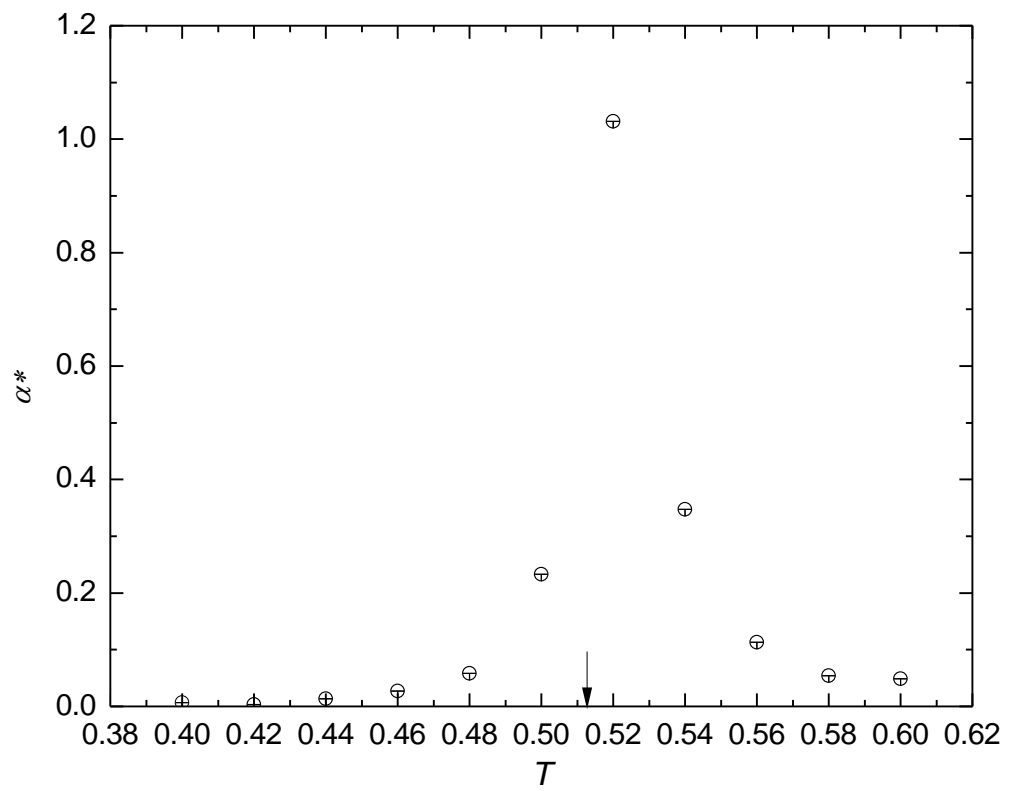
Figure 5.6: The temperature dependent of α^*, the arrow marks $T_I \simeq 0.513$.
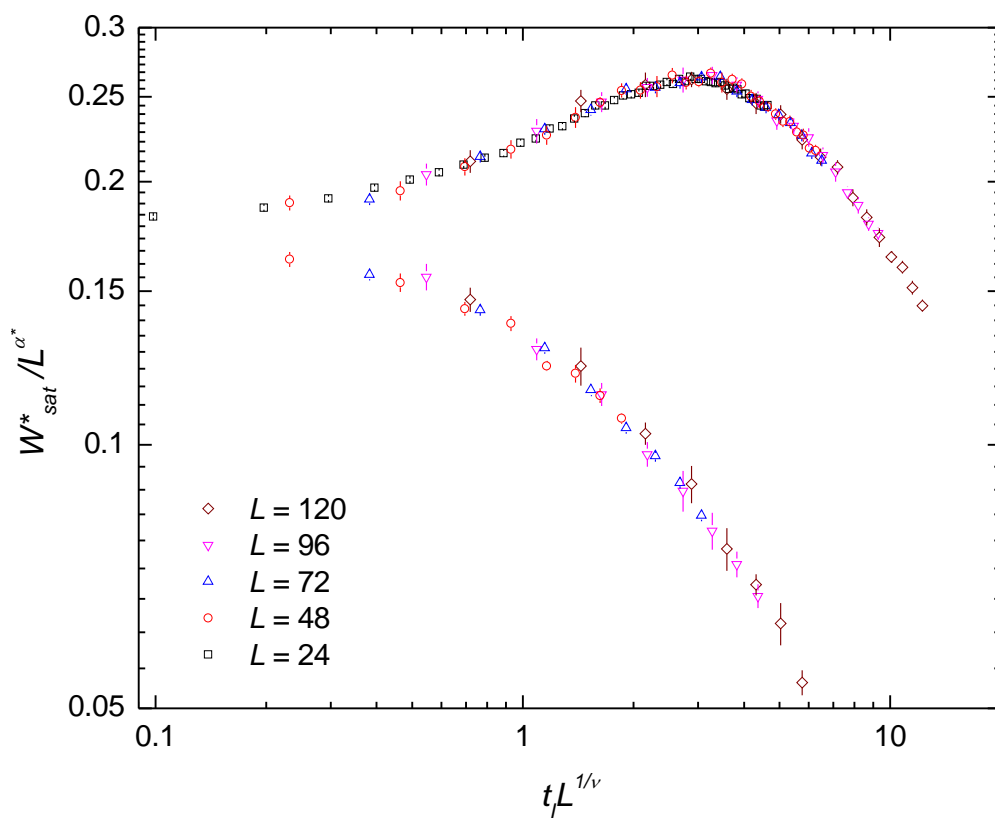
Figure 5.7: Log-log plot of the data collapse of W^*_{sat}/L^{α^*} as a function of $t_I L^{1/\nu}$.

and $T_I = 0.513$. The critical exponent ν agrees with $\nu = 0.83$ (Ref. [117]) and $\nu = 0.84$ (Ref. [118]) obtained from conventional methods. At $T = T_I$, the growth exponent β_w relates to the exponents of the spin model through [109]

$$\beta_w = 1 - \frac{\beta}{\nu z} \quad (L \to \infty), \tag{5.8}$$

where β and z are the order parameter and dynamical exponents of the spin model. Taking $\beta = 0.106$, $\nu = 0.84$, and $z = 2.52$ from Ref. [118], β_w is estimated to be $\beta_w = 0.95$. From Fig. 5.3, $\beta_w = \beta_w^* + 0.5 = 0.923$. It can be seen that β_w obtained from the two methods are comparable. However, the smaller value may be caused by the finite size effect [104, 105]. For $\alpha^* = 0.963$ and $\beta_w^* = 0.423$, the dynamical exponent z_w is calculated from $z_w = \alpha^*/\beta_w^* = 2.28$ compared with those value obtained from conventional spin method which is $z = 2.52$ [118].

5.4   Summary

Results in this chapter, An Application of Roughness Exponent Method in a Frustrated Spin System, are summarized as follows. Firstly, the film roughness reaches its maximum value at a critical temperature. Secondly, the critical exponent ν of the correlation length in spin systems can be obtained from the roughness exponent method. Next, the exponents of the SOS growth model and FAXY model are connected through the scaling relation. Finally, our results are comparable with those results obtained from conventional spin methods.

CHAPTER VI

Conclusions

Heteroepitaxial growth is truly a large subject studied in thin film physics. Microscopic processes which occur during the real MBE growth are far more complex than those of any existing models we investigated. Even with the same heteroepitaxial systems, one cloud not expect to have the same experimental results, since growth conditions, growth preparations etc. seem to involve in the growth process. Nevertheless, it is found that some phenomena have been observed in a large class among the heteroepitaxial systems, sharing the same underlying principle. The formation of self-assembled, strained islands also called the quantum dots is one of the phenomena found in many heteroepitaxial systems. Therefore, the main objective of this work is to investigate the formation of the islands and pits by using computer modelling. A two-dimensional discrete ball and spring model is chosen to simulate an heteroepitaxial system. The dynamics of the system are controlled by the kinetic Monte Carlo simulations. Within the scope of this work, our numerical results show that the ball and spring model is indeed a suitable model to study heteroepitaxial systems.

We conclude that the island (pit) formation is purely a result of relieving strain in the system. The island formation is supported by the diffusion bias at the film-substrate interface, especially at the kink sites, where the strain is mostly registered to. The lattice mismatch, deposition flux, and growth temperature are equally important factors which specify the film surface morphologies. According to our extensive results, the relevant properties of heteroepitaxial thin films, i.e. the critical thickness, island size, and number of islands, in the island formation

regime are summarized in Table 4.1. Here, we note that the formation of pits in the limited mobility growth regime is another strain-relieved mechanism found in the system.

We also investigate surface roughening of a modified SOS growth model to determine critical properties of a seemingly different model, the frustrated antiferromagnetic XY spin model. The film roughness achieved by mapping spin configurations to film surfaces of the SOS growth model is proved to be able to identify the critical temperature in the spin model with accurate figures. The scaling hypothesis and relation between exponents in both models are useful tools for verifying the universality class of the spin model. According to our work and previous work in the literature reviews, we believe that the roughness exponent method can be applied to other physical systems as well.

Finally, we recommend that for further investigation, the heteroepitaxial growth should be extended to three-dimensional simulations. Due to many aspects of the heteroepitaxial growth, we draw here some possible studies in this area. Influence of crystalline substrates on the island shape is a promising topic to be investigated. Off-lattice models are other candidates which can be used to study dislocations, wetting layers etc. and are suitable for highly strained heteroepitaxial systems. We believe that the growth process which allows the film annealing and/ or alloying would provide another strain-relieved mechanism.

References

[1] Barnham, K., and Vvedensky, D. *Low-dimensional semiconductor structures: Fundamentals and device applications.* Cambridge: Cambridge University Press, 2001.

[2] Barabási, A. -L., and Stanley, H. E. *Fractal concepts in surface growth.* Cambridge: Cambridge University Press, 1995.

[3] Arthur, J. R. Molecular beam epitaxy. *Surf. Sci.* **500** (2002): 189–217.

[4] Bimberg, D., and Pohl, U. W. Quantum dots: Promises and accomplishments. *materialstoday* **14** (2011): 388–397.

[5] Petroff, P. M., Lorke, A., and Imamoglu, A. Epitaxially self-assembled quantum dots. *Phys. Today* **54** (2001): 46–52.

[6] Aqua, J. -N., Berbezier, I., Favre, L., Frisch, T., and Ronda, A. Growth and self-organization of SiGe nanostructures. *Phys. Rep.* **522** (2013): 59–189.

[7] Mo, Y. -W., Savage, D. E., Swartzentruber, B. S., and Lagally, M. G. Kinetic pathway in Stranski-Krastanov growth of Ge on Si(001). *Phys. Rev. Lett.* **65** (1990): 1020–1023.

[8] Tersoff, J., and LeGoues, F. K. Competing relaxation mechanisms in strained layers. *Phys. Rev. Lett.* **72** (1994): 3570–3573.

[9] Tersoff, J., Teichert, C., and Lagally, M. G. Self-organization in growth of quantum dot superlattices. *Phys. Rev. Lett.* **76** (1996): 1675–1678.

[10] Shklyaev, A. A., Shibata, M., and Ichikawa, M. Instability of two-dimensional layers in the Stranski-Krastanov growth mode of Ge on Si(111). *Phys. Rev. B* **58** (1998): 15647–15651.

[11] Kästner, M., and Voigtländer, B. Kinetically self-limiting growth of Ge islands on Si(001). *Phys. Rev. Lett.* **82** (1999): 2745–2748.

[12] Sutter, P., and Lagally, M. G. Nucleationless three-dimensional island formation in low-misfit heteroepitaxy. *Phys. Rev. Lett.* **84** (2000): 4637–4640.

[13] Tromp, R. M., Ross, F. M., and Reuter, M. C. Instability-driven SiGe island growth. *Phys. Rev. Lett.* **84** (2000): 4641–4644.

[14] Springholz, G., et al. Vertical and lateral ordering in self-organized quantum dot superlattices. *Physica E* **9** (2001): 149–163.

[15] Tersoff, J., Spencer, B. J., Rastelli, A., and von Känel, H. Barrierless formation and faceting of SiGe islands on Si(001). *Phys. Rev. Lett.* **89** (2002): 196104–196107.

[16] Rastelli, A., and von Känel, H. Island formation and faceting in the SiGe/Si(001) system. *Surf. Sci.* **532–535** (2003): 769–773.

[17] Yang, Z., et al. Optical properties of Ge/Si quantum dot superlattices. *Mater. Lett.* **58** (2004): 3765–3768.

[18] Dubrovskii, V. G., et al. Effect of growth kinetics on the structural and optical properties of quantum dot ensembles. *J. Cryst. Growth* **267** (2004): 47–59.

[19] Gray, J. L., et al. Beyond the heteroepitaxial quantum dot: Self-assembling complex nanostructures controlled by strain and growth kinetics. *Phys. Rev. B* **72** (2005): 155323–155333.

[20] Leonard, D., Pond, K., and Petroff, P. M. Critical layer thickness for self-assembled InAs islands on GaAs. *Phys. Rev. B* **50** (1994): 11687–11692.

[21] Grundmann, M., et al. Ultranarrow luminescence lines from single quantum dots. *Phys. Rev. Lett.* **74** (1995): 4043–4046.

[22] Xie, Q., Madhukar, A., Chen, P., and Kobayashi, N. P. Vertically self-organized InAs quantum box islands on GaAs(100). *Phys. Rev. Lett.* **75** (1995): 2542–2545.

[23] Ruvimov, S., Werner, P., Scheerschmidt, K., Gösele, U., and Heydenreich, J. Structural characterization of (In,Ga)As quantum dots in a GaAs matrix. *Phys. Rev. B* **51** (1995): 14766–14769.

[24] Heitz, R., et al. Observation of reentrant 2D to 3D morphology transition in highly strained epitaxy: InAs on GaAs. *Phys. Rev. Lett.* **78** (1997): 4071–4074.

[25] Joyce, B. A., et al. Nucleation mechanisms during MBE growth of lattice-matched and strained III-V compound films. *Appl. Surf. Sci.* **130**−**132** (1998): 357–366.

[26] Bromann, K., Giovannini, M., Brune, H., and Kern, K. Self-organized growth of cluster arrays. *Eur. Phys. J. D* **9** (1999): 25–28.

[27] Koroknay, E., Rengstl, U., Bommer, M., Jetter, M., and Michler, P. Site-controlled growth of InP/GaInP islands on periodic hole patterns in GaAs substrates produced by microsphere photolithography. *J. Cryst. Growth* **370** (2013): 146–149.

[28] Zhang, J., Rastelli, A., Schmidt, O. G., and Bauer, G. Site-controlled SiGe islands on patterned Si(001): Morphology, composition profiles, and devices. *Phys. Status Solidi B* **249** (2012): 752–763.

[29] Szkutnik, P. D., et al. Influence of patterning on the nucleation of Ge islands on Si and SiO_2 surfaces. *Surf. Sci.* **601** (2007): 2778–2782.

[30] QD Laser, Inc. Available from: http://www.qdlaser.com [2012, November 07]

[31] Ledentsov, N. N., Ustinov, V. M., Shchukin, V. A., Kop'ev, P. S., and Alferov, Zh. I. Quantum dot heterostructures: Fabrication, properties, lasers (Review). *Semiconductors* **32** (1998): 343–365.

[32] Bimberg, D., et al. Quantum dot lasers: Breakthrough in optoelectronics. *Thin Solid Films* **367** (2000): 235–249.

[33] Ledentsov, N. N., et al. Quantum-dot heterostructure lasers. *IEEE J. Sel. Top. Quantum Electron.* **6** (2000): 439–451.

[34] Ledentsov, N. N., et al. Submonolayer quantum dots for high speed surface emitting lasers. *Nanoscale Res. Lett.* **2** (2007): 417–429.

[35] Ledentsov, N. N., Bimberg, D., and Alferov, Zh. I. Progress in epitaxial growth and performance of quantum dot and quantum wire lasers. *J. Lightwave Technol.* **26** (2008): 1540–1555.

[36] Pimpinelli, A., and Villain, J. *Physics of crystal growth.* Cambridge: Cambridge University Press, 1998.

[37] Grinfeld, M. A. The stress driven instability in elastic crystals: Mathematical models and physical manifestations. *J. Nonlinear Sci.* **3** (1993): 35–83.

[38] Lam, C. -H., Lee, C. -K., and Sander, L. M. Competing roughening mechanisms in strained heteroepitaxy: A fast kinetic Monte Carlo study. *Phys. Rev. Lett.* **89** (2002): 216102–216105.

[39] Lung, M. T., Lam, C. -H., and Sander, L. M. Island, pit, and groove formation in strained heteroepitaxy. *Phys. Rev. Lett.* **95** (2005): 086102–086105.

[40] Xiang, R., Lung, M. T., and Lam, C. -H. Layer-by-layer nucleation mechanism for quantum dot formation in strained heteroepitaxy. *Phys. Rev. E* **82** (2010): 021601–021608.

[41] Moll, N., Scheffler, M., and Pehlke, E. Influence of surface stress on the equilibrium shape of strained quantum dots. *Phys. Rev. B* **58** (1998): 4566–4571.

[42] Wang, L. G., Kratzer, P., Scheffler, M., and Moll, N. Formation and stability of self-assembled coherent islands in highly mismatched heteroepitaxy. *Phys. Rev. Lett.* **82** (1999): 4042–4045.

[43] van de Walle, A., Asta, M., and Voorhees, P. W. First-principles calculation of the effect of strain on the diffusion of Ge adatoms on Si and Ge(001) surfaces. *Phys. Rev. B* **67** (2003): 041308–041311.

[44] Miyazaki, T., Bowler, D. R., Gillan, M. J., and Ohno, T. The energetics of hut-cluster self-assembly in Ge/Si(001) from linear-scaling DFT calculations. *J. Phys. Soc. Jpn.* **77** (2008): 123706–123709.

[45] Liu, P., Zhang, Y. W., and Lu, C. Computer simulations of the Stranski-Krastanov growth of heteroepitaxial films with elastic anisotropy. *Surf. Sci.* **526** (2003): 375–382.

[46] Zhang, Y. W., Bower, A. F., and Liu, P. Morphological evolution driven by strain induced surface diffusion. *Thin Solid Films* **424** (2003): 9–14.

[47] Queka, S. S., and Liu, G. R. Simulation of surface evolution of quantum dot using meshfree approximation. *Thin Solid Films* **479** (2005): 297–309.

[48] Ni, Y., He, L. H., and Soh, A. K. Three-dimensional phase field simulation for surface roughening of heteroepitaxial films with elastic anisotropy. *J. Cryst. Growth* **284** (2005): 281–292.

[49] Liu, P., Lu, C., Zhang, Y. -W., and Lam, K. -Y. Heteroepitaxial growth of quantum wire arrays through prepatterning substrate surfaces. *Appl. Phys. Lett.* **91** (2007): 093129–093131.

[50] Pang, Y., and Huang, R. Effect of elastic anisotropy on surface pattern evolution of epitaxial thin films. *Int. J. Solids Struct.* **46** (2009): 2822–2833.

[51] Korzec, M. D., and Evans, P. L. From bell shapes to pyramids: A reduced continuum model for self-assembled quantum dot growth. *Physica D* **239** (2010): 465–474.

[52] Jesson, D. E., Munt, T. P., Shchukin, V. A., and Bimberg, D. Suppression of coalescence during the coarsening of quantum dot arrays. *Phys. Rev. B* **69** (2004): 041302–041305.

[53] Aqua, J. -N., Frisch, T., and Verga, A. Ordering of strained islands during surface growth. *Phys. Rev. E* **81** (2010): 021605–021610.

[54] Schindler, A. C., et al. Theory of strain relaxation in heteroepitaxial systems. *Phys. Rev. B* **67** (2003): 075316–075329.

[55] Russo, G., and Smereka, P. Computation of strained epitaxial growth in three dimensions by kinetic Monte Carlo. *J. Comput. Phys.* **214** (2006): 809–828.

[56] Caflisch, R. E., Lee, Y. -J., Shu, S., Xiao, Y. -X., and Xu, J. An application of multigrid methods for a discrete elastic model for epitaxial systems. *J. Comput. Phys.* **219** (2006): 697–714.

[57] Lam, C. -H., Lung, M. T., and Sander, L. M. Fast kinetic Monte Carlo simulation of strained heteroepitaxy in three dimensions. *J. Sci. Comput.* **37** (2008): 73–88.

[58] Schulze, T. P., and Smereka, P. An energy localization principle and its application to fast kinetic Monte Carlo simulation of heteroepitaxial growth. *J. Mech. Phys. Solids* **57** (2009): 521–538.

[59] Baskaran, A., Devita, J., and Smereka, P. Kinetic Monte Carlo simulation of strained heteroepitaxial growth with intermixing. *Continuum Mech. Thermodyn.* **22** (2010): 1–26.

[60] Orr, B. G., Kessler, D., Snyder, C. W., and Sander, L. A model for strain-induced roughening and coherent island growth. *Europhys. Lett.* **19** (1992): 33–38.

[61] Barabási, A. -L. Self-assembled island formation in heteroepitaxial growth. *Appl. Phys. Lett.* **70** (1997): 2565–2567.

[62] Barabási, A. -L. Thermodynamic and kinetic mechanisms in self-assembled quantum dot formation. *Mater. Sci. Eng. B* **67** (1999): 23–30.

[63] Khor, K. E., and Das Sarma, S. Surface morphology and quantum dot self-assembly in growth of strained-layer semiconducting films. *J. Vac. Sci. Technol. B* **15** (1997): 1051–1055.

[64] Khor, K. E., and Das Sarma, S. Quantum dot self-assembly in growth of strained-layer thin films: A kinetic Monte Carlo study. *Phys. Rev. B* **62** (2000): 16657–16664.

[65] Lam, C. -H. Kinetic Monte Carlo simulation of faceted islands in heteroepitaxy using a multistate lattice model. *Phys. Rev. E* **81** (2010): 021607–021614.

[66] Guo, J. Y., Zhang, Y. W., and Lu, C. Effects of wetting and misfit strain on the pattern formation of heteroepitaxially grown thin films. *Comput. Mater. Sci.* **44** (2008): 174–179.

[67] Rouhani, M. D., Kassem, H., Torre, J. D., Landa, G., and Estève, D. Kinetic Monte Carlo simulation of intermixing during semiconductor heteroepitaxy. *Appl. Surf. Sci.* **188** (2002): 24–28.

[68] Volkmann, T., Much, F., Biehl, M., and Kotrla, M. Interplay of strain relaxation and chemically induced diffusion barriers: Nanostructure formation in 2D alloys. *Surf. Sci.* **586** (2005): 157–173.

[69] Niu, X., Stringfellow, G. B., and Liu, F. Phase separation in strained epitaxial InGaN islands. *Appl. Phys. Lett.* **99** (2011): 213102–213104.

[70] Faux, D. A., Gaynor, G., Carson, C. L., Hall, C. K., and Bernholc, J. Computer simulation studies of the growth of strained layers by molecular-beam epitaxy. *Phys. Rev. B* **42** (1990): 2914–2922.

[71] Jalkanen, J., Trushin, O., Granato, E., Ying, S. C., and Ala-Nissila, T. Equilibrium shape and size of supported heteroepitaxial nanoislands. *Eur. Phys. J. B* **66** (2008): 175–183.

[72] Much, F., Ahr, M., Biehl, M., and Kinzel, W. A kinetic Monte Carlo method for the simulation of heteroepitaxial growth. *Comput. Phys. Commun.* **147** (2002): 226–229.

[73] Much, F., and Biehl, M. Simulation of wetting-layer and island formation in heteroepitaxial growth. *Europhys. Lett.* **63** (2003): 14–20.

[74] Biehl, M., Ahr, M., Kinzel, W., and Much, F. Kinetic Monte Carlo simulations of heteroepitaxial growth. *Thin Solid Films* **428** (2003): 52–55.

[75] Schöll, E., and Bose, S. Kinetic Monte Carlo simulation of the nucleation stage of the self-organized growth of quantum dots. *Solid-State Electron.* **42** (1998): 1587–1591.

[76] Nurminen, L., Kuronen, A., and Kaski, K. Kinetic Monte Carlo simulation of nucleation on patterned substrates. *Phys. Rev. B* **63** (2000): 035407–035413.

[77] Elsholz, F., Meixner, M., and Schöll, E. Kinetic Monte Carlo simulation of self-organized pattern formation in thin film deposition. *Nucl. Instr. and Meth. in Phys. Res. B* **202** (2003): 249–254.

[78] Meixner, M., Kunert, R., and Schöll, E. Control of strain-mediated growth kinetics of self-assembled semiconductor quantum dots. *Phys. Rev. B* **67** (2003): 195301–195312.

[79] Larsson, M. I., Cho, K., and Clemens, B. M. Surface diffusion mechanisms for strain-induced self-assembly. *Phys. Rev. B* **69** (2004): 155426–155432.

[80] Petrov, P. P., and Miller, W. Kinetic Monte Carlo simulation of the wetting layer in Stranski-Krastanov heteroepitaxial growth. *Comput. Mater. Sci.* **60** (2012): 176–180.

[81] Nath, P., and Ranganathan, M. Kinetic Monte Carlo simulations of heteroepitaxial growth with an atomistic model of elasticity. *Surf. Sci.* **606** (2012): 1450–1457.

[82] Russo, G., and Smereka, P. A multigrid-fourier method for the computation of elastic fields with application to heteroepitaxy. *Multiscale Model. Simul.* **5** (2006): 130–148.

[83] Landau, D. P., and Binder, K. *A guide to Monte Carlo simulations in statistical physics.* Cambridge: Cambridge University Press, 2000.

[84] Patcha Punyindu. *Understanding kinetic surface roughening using local, discrete, nonequilibrium growth models.* Doctoral dissertation, Department of Physics, Graduate School of the University of Maryland, College Park, 2000.

[85] Das Sarma, S., and Tamborenea, P. A new universality class for kinetic growth: One-dimensional molecular-beam epitaxy. *Phys. Rev. Lett.* **66** (1991): 325–328.

[86] Wolf, D. E., and Villain, J. Growth with surface diffusion. *Europhys. Lett.* **13** (1990): 389–394.

[87] Family, F. Scaling of rough surfaces: Effects of surface diffusion. *J. Phys. A* **19** (1986): L441–L446.

[88] Bogicevic, A., Strömquist, J., and Lundqvist, B. I. Low-symmetry diffusion barriers in homoepitaxial growth of Al(111). *Phys. Rev. Lett.* **81** (1998): 637–640.

[89] Müller, M., Albe, K., Busse, C., Thoma, A., and Michely, T. Island shapes, island densities, and stacking-fault formation on Ir(111): Kinetic Monte Carlo simulations and experiments. *Phys. Rev. B* **71** (2005): 075407–075414.

[90] Kittel, C. *Introduction to solid state physics.* 8th ed. New Jersey: John Wiley & Sons, Inc., 2005.

[91] Newman, M. E. J., and Barkema, G. T. *Monte Carlo methods in statistical physics.* Oxford: Oxford University Press, 1999.

[92] Press, W. H., Teukolsky, S. A., Vetterling, W. T., and Flannery, B. P. *Numerical recipes in C: The art of scientific computing.* 2nd ed. Cambridge: Cambridge University Press, 1992.

[93] van der Vorst, H. A. Bi-CGSTAB: A fast and smoothly converging variant of Bi-CG for the solution of nonsymmetric linear systems. *SIAM J. Sci. and Stat. Comput.* **13** (1992): 631–644.

[94] Yeomans, J. M. *Statistical mechanics of phase transitions.* Oxford: Clarendon Press, 1992.

[95] Bulnes, F. M., Pereyra, V. D., and Riccardo, J. L. Collective surface diffusion: N-fold way kinetic Monte Carlo simulation. *Phys. Rev. E* **58** (1998): 86–92.

[96] Bortz, A. B., Kalos, M. H., and Lebowitz, J. L. New algorithm for Monte Carlo simulations of Ising spin systems. *J. Comp. Phys.* **17** (1975): 10–18.

[97] Huo, S., and Schwarzacher, W. Anomalous scaling of the surface width during Cu electrodeposition. *Phys. Rev. Lett.* **86** (2001): 256–259.

[98] Hasan, N. M., Mallett, J. J., dos Santos Filho, S. G., Pasa, A. A., and Schwarzacher, W. Dynamic scaling of the surface roughness of Cu deposited using a chemical bath. *Phys. Rev. B* **67** (2003): 081401–081404.

[99] Cavalcanti, W. L., Figueiredo, W., and Santos, M. Growth model on (1+1) dimensions with local relaxation and discrete number of orientation. *Phys. Status Solidi A* **201** (2004): 894–897.

[100] López, J. M., Castro, M., and Gallego, R. Scaling of local slopes, conservation laws, and anomalous roughening in surface growth. *Phys. Rev. Lett.* **94** (2005): 166103–166106.

[101] Kosturek, R., and Malarz, K. New cellular automaton designed to simulate epitaxial films growth. *Physica A* **345** (2005): 538–546.

[102] Forgerini, F. L., and Figueiredo, W. Thin-film growth by random deposition of rod-like particles on a square lattice. *Phys. Status Solidi C* **8** (2011): 3119–3122.

[103] Redinz, J. A., and Martins, M. L. Roughness exponent in two-dimensional percolation, Potts model, and clock model. *Phys. Rev. E* **63** (2001): 066133–066138.

[104] Brito, A. F., Redinz, J. A., and Plascak, J. A. Dynamics of rough surfaces generated by two-dimensional lattice spin models. *Phys. Rev. E* **75** (2007): 046106–046113.

[105] Brito, A. F., Redinz, J. A., and Plascak, J. A. Two-dimensional XY and clock models studied via the dynamics generated by rough surfaces. *Phys. Rev. E* **81** (2010): 031130–031140.

[106] de Sales, J. A., Matins, M. L., and Moreira, J. G. One-dimensional cellular automata characterization by the roughness exponent. *Physica A* **245** (1997): 461–471.

[107] de Sales, J. A., Matins, M. L., and Moreira, J. G. Roughness exponent in the Domany-Kinzel cellular automaton. *J. Phys. A* **32** (1999): 885–890.

[108] Atman, A. P. F., and Moreira, J. G. Growth exponent in the Domany-Kinzel cellular automaton. *Eur. Phys. J. B* **16** (2000): 501–505.

[109] Atman, A. P. F., Dickman, R., and Moreira, J. G. Scaling exponents of rough surfaces generated by the Domany-Kinzel cellular automaton. *Phys. Rev. E* **66** (2002): 016113–016120.

[110] Brito, A. F., and Redinz, J. A. Superrougheningin the Isingchain with long-range interactions. *Physica A* **333** (2004): 269–277.

[111] Resnick, D. J., Garland, J. C., Boyd, J. T., Shoemaker, S., and Newrock, R. S. Kosterlitz-Thouless transition in proximity-coupled superconducting arrays. *Phys. Rev. Lett.* **47** (1981): 1542–1545.

[112] Villain, J. Two-level systems in a spin-glass model. I. General formalism and two-dimensional model. *J. Phys. C* **10** (1977): 4793–4803.

[113] Luo, H. J., Schülke, L., and Zheng, B. Dynamic approach to the fully frustrated XY Model. *Phys. Rev. Lett.* **81** (1998): 180–183.

[114] Boubcheur, E. H., and Diep, H. T. Critical behavior of the two-dimensional fully frustrated XY model. *Phys. Rev. B* **58** (1998): 5163–5165.

[115] Olsson, P. Monte Carlo study of the Villain version of the fully frustrated XY model. *Phys. Rev. B* **55** (1997): 3585–3602.

[116] Lee, J., Kosterlitz, J. M., and Granato, E. Monte Carlo study of frustrated XY models on a triangular and square lattice. *Phys. Rev. B* **43** (1991): 11531–11534.

[117] Lee, S., and Lee, K. -C. Phase transitions in the fully frustrated triangular XY model. *Phys. Rev. B* **57** (1998): 8472–8477.

[118] Ozeki, Y., and Ito, N. Nonequilibrium relaxation analysis of fully frustrated XY models in two dimensions. *Phys. Rev. B* **68** (2003): 054414–054421.

[119] Noh, J. D., Rieger, H., Enderle, M., and Knorr, K. Critical behavior of the frustrated antiferromagnetic six-state clock model on a triangular lattice. *Phys. Rev. E* **66** (2002): 026111–026117.

[120] Surungan, T., Okabe, Y., and Tomita, Y. Study of the fully frustrated clock model using the Wang-Landau algorithm. *J. Phys. A* **37** (2004): 4219–4230.

[121] Family, F., and Vicsek, T. Scaling of the active zone in the Eden process on percolation networks and the ballistic deposition model. *J. Phys. A* **18** (1985): L75–L81.

[122] Huang, K. *Statistical mechanics.* New York: John Wiley & Sons, 1987.

APPENDICES

APPENDIX A

List of Notations

Symbol	Definition	Page
a_f, a_s	lattice constant	2
ATG	Asaro-Tiller-Grinfeld	6
Bi-CGSTAB	biconjugate gradient stabilized	22
D	dimensional	3
DFT	density functional theory	7
DOS	density of state	3
e_i	energy stored in springs connected to atom i	24
E	total elastic energy	15
E_0	surface binding energy	21
E_a	activation energy	18
E_b	binding energy	21
F	deposition flux	19
FAXY	frustrated antiferromagnetic XY	10
FM	Frank-van der Merwe	4
h	film thickness	4
h_c	critical thickness	5
H	local height	27
k_B	Boltzmann constant	7
kMC	kinetic Monte Carlo	7
k_{NN}, k_{NNN}	spring strength	13
l	island size	6
L	substrate size	15

Symbol	*Definition*	*Page*
MBE	molecular-beam epitaxy	1
ML	monolayer	9
NN	nearest neighbors	13
NNN	next-nearest neighbors	13
QDs	quantum dots	3
R_0	characteristic vibrational frequency	21
R_d	deposition rate	19
R_i	diffusion rate	21
RD	random deposition	12
$s_{\max}$	maximum hopping distance	19
SK	Stranski-Krastanov	4
SOS	solid-on-solid	8
t	time	72
$t_\times$	crossover time	73
T	temperature	7
T_I	critical temperature	71
VW	Volmer-Weber	4
W	local width	27
W	interface width or roughness	69
ΔE_i	elastic energy difference	22
$\alpha,\ \beta,\ z,\ \nu$	exponent	69, 82
ϵ	lattice mismatch or misfit	2
θ	coverage or average thickness	34
ξ	correlation length	79

APPENDIX B

List of Constants

Symbol	Value	Page
a_s	2.715 Å	13
$c(n_i, h_i)$	see Table 3.1	25
D_0	3.83×10^{13} Å$^2 \cdot$ s^{-1}	21
E_0	-0.25 eV	21
E_b	0.30 eV	21
H	5 sites	27
k_{NN}	20.73 eV/a_s^2 = 2.81 eV·Å^{-2}	13
k_{NNN}	k_{NN}	13
R_tol	10^{-2}	24
s_max	8 sites	19
W	25 sites	27

APPENDIX C

System of Linear Equations

Recall Eq. (2.13),

$$\mathbf{K} \cdot \vec{u} = \vec{f}. \tag{C.1}$$

The components $K(i,j)$, $u(i)$, and $f(i)$ are given by

$$
\begin{pmatrix}
K^x(1,1) & K^x(1,2) & K^x(1,3) & \dots & K^x(1,N) \\
K^y(1,1) & K^y(1,2) & K^y(1,3) & \dots & K^y(1,N) \\
K^x(2,1) & K^x(2,2) & K^x(2,3) & \dots & K^x(2,N) \\
K^y(2,1) & K^y(2,2) & K^y(2,3) & \dots & K^y(2,N) \\
\vdots & \vdots & \vdots & \ddots & \vdots \\
K^x(\frac{N}{2},1) & K^x(\frac{N}{2},2) & K^x(\frac{N}{2},3) & \dots & K^x(\frac{N}{2},N) \\
K^y(\frac{N}{2},1) & K^y(\frac{N}{2},2) & K^y(\frac{N}{2},3) & \dots & K^y(\frac{N}{2},N)
\end{pmatrix}
\begin{pmatrix}
u_x(1) \\
u_y(1) \\
u_x(2) \\
u_y(2) \\
\vdots \\
u_x(\frac{N}{2}) \\
u_y(\frac{N}{2})
\end{pmatrix}
=
\begin{pmatrix}
f_x(1) \\
f_y(1) \\
f_x(2) \\
f_y(2) \\
\vdots \\
f_x(\frac{N}{2}) \\
f_y(\frac{N}{2})
\end{pmatrix},
\tag{C.2}
$$

where $N = 2L$. The components $K^x(i,j)$ and $K^y(i,j)$ relate to the forces acting on atom i in x and y directions as,

$$F_x(i) = \sum_j K^x(i,j)u(j) - f_x(i) = 0, \tag{C.3}$$

and

$$F_y(i) = \sum_j K^y(i,j)u(j) - f_y(i) = 0. \tag{C.4}$$

For more convenience, we map the data of the $(N \times N)$ matrix $\mathbf{K}$ to a 1D array whose size is N^2. The components $f_x(i)$ and $f_y(i)$ are stored in variable f specified by index i as,

$$f_x(i) \Rightarrow f[2i-1], \quad f_y(i) \Rightarrow f[2i]. \tag{C.5}$$

The components $K^x(i,j)$ and $K^y(i,j)$ are given by

$$K^x(i,j) \Rightarrow \begin{cases} K[2(i-1)N + (2j-1)] & \text{if } j = \text{odd}, \\ K[2(i-1)N + 2j] & \text{if } j = \text{even}, \end{cases} \tag{C.6}$$

and

$$K^y(i,j) \Rightarrow \begin{cases} K[2(i-1)N + N + (2j-1)] & \text{if } j = \text{odd}, \\ K[2(i-1)N + N + 2j] & \text{if } j = \text{even}. \end{cases} \tag{C.7}$$

An atom interacting with the atom i is now represented by index j. For the atom i (see Fig. C.1), the interaction is in the range of NN and NNN. Thus, the index j runs only over NN $= i+1$, $i-L$, $i-1$, $i+L$ and NNN $= i+1-L$, $i-1-L$, $i-1+L$, $i+1+L$. The directions of NN and NNN respected to the atom i are labeled with (1), (2), (3), and (4). In x direction, the values of the arrays f and
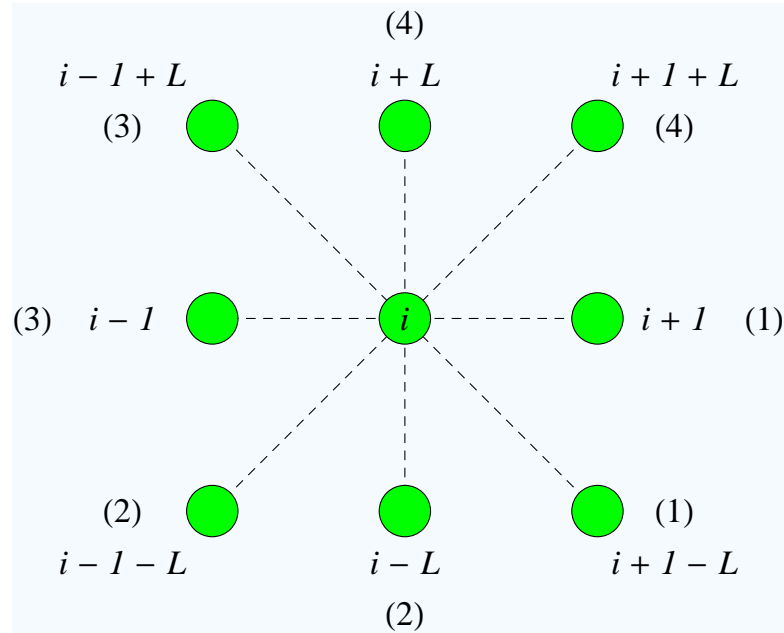

Figure C.1: The nearest neighbors (NN) and next-nearest neighbors (NNN) of atom i. The sign (...) labels the directions of NN and NNN respected to the atom i.

K are

$$f[2i-1] = k_{NNN}\delta_{i,i-1-L}(d_1 + d_2) - k_{NNN}\delta_{i,i+1-L}(d_1 + d_2)$$
$$+ 2k_{NN}\delta_{i,i-1}d_1 - 2k_{NN}\delta_{i,i+1}d_1 \tag{C.8}$$
$$+ k_{NNN}\delta_{i,i-1+L}(d_1 + d_2) - k_{NNN}\delta_{i,i+1+L}(d_1 + d_2).$$

For $j = i - 1 - L$,

$$K[2(i-1)N + (2j-1)] = -k_{NNN}\delta_{i,i-1-L},$$
$$K[2(i-1)N + 2j] = -k_{NNN}\delta_{i,i-1-L}. \tag{C.9}$$

For $j = i - L$,

$$K[2(i-1)N + (2j-1)] = 0,$$
$$K[2(i-1)N + 2j] = 0. \tag{C.10}$$

For $j = i + 1 - L$,

$$K[2(i-1)N + (2j-1)] = -k_{NNN}\delta_{i,i+1-L},$$
$$K[2(i-1)N + 2j] = k_{NNN}\delta_{i,i+1-L}. \tag{C.11}$$

For $j = i - 1$,

$$K[2(i-1)N + (2j-1)] = -2k_{NN}\delta_{i,i-1},$$
$$K[2(i-1)N + 2j] = 0. \tag{C.12}$$

For $j = i$,

$$K[2(i-1)N + (2j-1)] = 2k_{NN}\delta_{i,i-1} + 2k_{NN}\delta_{i,i+1}$$
$$+ k_{NNN}\delta_{i,i-1-L} + k_{NNN}\delta_{i,i+1+L}$$
$$+ k_{NNN}\delta_{i,i-1+L} + k_{NNN}\delta_{i,i+1-L}, \tag{C.13}$$
$$K[2(i-1)N + 2j] = k_{NNN}\delta_{i,i+1+L} + k_{NNN}\delta_{i,i-1-L}$$
$$- k_{NNN}\delta_{i,i-1+L} - k_{NNN}\delta_{i,i+1-L}.$$

For $j = i + 1$,

$$K[2(i-1)N + (2j-1)] = -2k_{NN}\delta_{i,i+1},$$
$$K[2(i-1)N + 2j] = 0. \tag{C.14}$$

For $j = i - 1 + L$,

$$K[2(i-1)N + (2j-1)] = -k_{NNN}\delta_{i,i-1+L},$$
$$K[2(i-1)N + 2j] = k_{NNN}\delta_{i,i-1+L}. \tag{C.15}$$

For $j = i + L$,

$$K[2(i-1)N + (2j-1)] = 0,$$
$$K[2(i-1)N + 2j] = 0. \tag{C.16}$$

For $j = i + 1 + L$,

$$K[2(i-1)N + (2j-1)] = -k_{NNN}\delta_{i,i+1+L},$$
$$K[2(i-1)N + 2j] = -k_{NNN}\delta_{i,i+1+L}. \tag{C.17}$$

In y direction, the values of the arrays f and K are

$$f[2i] = k_{NNN}\delta_{i,i-1-L}(d_1 + d_2) + k_{NNN}\delta_{i,i+1-L}(d_1 + d_2)$$
$$+ 2k_{NN}\delta_{i,i-L}d_2 - 2k_{NN}\delta_{i,i+L}d_2 \tag{C.18}$$
$$- k_{NNN}\delta_{i,i-1+L}(d_1 + d_2) - k_{NNN}\delta_{i,i+1+L}(d_1 + d_2).$$

For $j = i - 1 - L$,

$$K[2(i-1)N + N + (2j-1)] = -k_{NNN}\delta_{i,i-1-L},$$
$$K[2(i-1)N + N + 2j] = -k_{NNN}\delta_{i,i-1-L}. \tag{C.19}$$

For $j = i - L$,

$$K[2(i-1)N + N + (2j-1)] = 0,$$
$$K[2(i-1)N + N + 2j] = -2k_{NN}\delta_{i,i-L}. \tag{C.20}$$

For $j = i + 1 - L$,

$$K[2(i-1)N + N + (2j-1)] = k_{NNN}\delta_{i,i+1-L},$$
$$K[2(i-1)N + N + 2j] = -k_{NNN}\delta_{i,i+1-L}. \tag{C.21}$$

For $j = i - 1$,

$$K[2(i-1)N + N + (2j-1)] = 0,$$
$$K[2(i-1)N + N + 2j] = 0. \tag{C.22}$$

For $j = i$,

$$K[2(i-1)N + N + (2j-1)] = k_{NNN}\delta_{i,i-1-L} + k_{NNN}\delta_{i,i+1+L}$$
$$- k_{NNN}\delta_{i,i-1+L} - k_{NNN}\delta_{i,i+1-L},$$
$$K[2(i-1)N + N + 2j] = 2k_{NN}\delta_{i,i-L} + 2k_{NN}\delta_{i,i+L} \qquad \text{(C.23)}$$
$$+ k_{NNN}\delta_{i,i+1+L} + k_{NNN}\delta_{i,i-1-L}$$
$$+ k_{NNN}\delta_{i,i-1+L} + k_{NNN}\delta_{i,i+1-L}.$$

For $j = i + 1$,

$$K[2(i-1)N + N + (2j-1)] = 0,$$
$$K[2(i-1)N + N + 2j] = 0. \qquad \text{(C.24)}$$

For $j = i - 1 + L$,

$$K[2(i-1)N + N + (2j-1)] = k_{NNN}\delta_{i,i-1+L},$$
$$K[2(i-1)N + N + 2j] = -k_{NNN}\delta_{i,i-1+L}. \qquad \text{(C.25)}$$

For $j = i + L$,

$$K[2(i-1)N + N + (2j-1)] = 0,$$
$$K[2(i-1)N + N + 2j] = -2k_{NN}\delta_{i,i+L}. \qquad \text{(C.26)}$$

For $j = i + 1 + L$,

$$K[2(i-1)N + N + (2j-1)] = -k_{NNN}\delta_{i,i+1+L},$$
$$K[2(i-1)N + N + 2j] = -k_{NNN}\delta_{i,i+1+L}. \qquad \text{(C.27)}$$

It is important to note that the NN and NNN of the atom i must be subjected to the periodic boundary conditions in x direction.

APPENDIX D

Publications and Presentations

PUBLICATIONS:

2013　Klawtanong, M., Srinitiwarawong, C., and Chatraphorn, P. Chiral symmetry breaking in FAXY model with roughness exponent method. *Physica A* **392** (2013): 6307–6313.

CONFERENCE PRESENTATIONS:

2009　Klawtanong, M., and Srinitiwarawong, C. Two-separate critical temperatures of the frustrated antiferromagnetic (FAXY) XY model on the triangular lattice. The 12nd National Graduate Research Conference, Khon Kaen, Thailand (12-13 February 2009).

2009　Klawtanong, M., and Srinitiwarawong, C. Phase transitions in the frustrated antiferromagnetic XY Model on the triangular lattice. Siam Physics Congress 2009, Phetchburi, Thailand (19-21 March 2009).

2010　Klawtanong, M., Srinitiwarawong, C., and Chatraphorn, P. Rough surfaces generated by the 2D spin models. Siam Physics Congress 2010, Kanchanaburi, Thailand (25-27 March 2010).

2010　Klawtanong, M., Srinitiwarawong, C., and Chatraphorn, P. Chiral symmetry breaking in FAXY model using roughness exponent. The 6th Mathematics and Physical Science Graduate Congress 2010, Kuala Lumpur, Malaysia (13-15 December 2010).

2011   Klawtanong, M., Srinitiwarawong, C., and Chatraphorn, P. Phase transition in the FAXY model using roughness exponent method. Siam Physics Congress 2011, Pattaya, Thailand (23-26 March 2011).

2012   Klawtanong, M., Srinitiwarawong, C., and Chatraphorn, P. Fast kinetic Monte Carlo simulation of heteroepitaxial thin film growth with a local approximation technique. Siam Physics Congress 2012, Phra Nakhon Si Ayutthaya, Thailand (9-12 May 2012).

2012   Klawtanong, M., Srinitiwarawong, C., and Chatraphorn, P. Surface morphology of heteroepitaxy thin films: Fast kinetic Monte Carlo simulations. The 8th Mathematics and Physical Science Graduate Congress 2012, Bangkok, Thailand (8-10 December 2012).

2013   Klawtanong, M., Srinitiwarawong, C., and Chatraphorn, P. Strained quantum dot formation in epitaxy thin films: Fast kinetic Monte Carlo simulations. Siam Physics Congress 2013, Chiang Mai, Thailand (21-23 March 2013).

Vitae

Manit Klawtanong was born on June 16, 1983 in Songkhla, Thailand. He received Bachelor's Degree of Science (Second Class Honors) in Physics from Prince of Songkla University in 2006. He continued studying and received Master's Degree of Science in Physics from Chulalongkorn University in 2009.